



universität  
wien

# DISSERTATION

Titel der Dissertation

## Self-Assembled Monolayers Studied by Density-Functional Theory

Verfasser

Dipl.-Ing. David Karhánek

angestrebter akademischer Grad

Doktor der Naturwissenschaften (Dr. rer. nat.)

Wien, 2010

Studienkennzahl lt. Studienblatt: A 091 419

Dissertationsgebiet lt. Studienblatt: Chemie

Betreuer: o.Univ.Prof. Dipl.-Ing. Dr.techn. Jürgen Hafner



# Eidesstattliche Erklärung

Ich erkläre hiermit an Eides Statt, dass ich die vorliegende Arbeit selbständig und ohne Benutzung anderer als der angegebenen Hilfsmittel angefertigt habe.

Die aus fremden Quellen direkt oder indirekt übernommenen Gedanken sind als solche kenntlich gemacht.

Die Arbeit wurde bisher in gleicher oder ähnlicher Form keiner anderen Prüfungsbehörde vorgelegt und auch noch nicht veröffentlicht.

David Karhánek  
Wien, am 5. Mai 2010



# Acknowledgements

I would like to thank to my parents, *Anna Karhánková* and *Zdeněk Karhánek*, for their support they were giving me all the long years of my education up to the doctor degree. They always support me in good times, they find the right words not to give up in the bad times - and they have been always the rational break when I wanted to achieve for what I did not have sufficient power.

There is a big word "thank you" that belongs to my girlfriend *Denisa*, who always found pleasant psychologic support for me and my work, which took that much time, so that others would have maybe already given up.

Among my colleagues, I would like to thank to *Dr. Joachim Paier* and *Dr. Konstantinos Termentzidis* for a big help in my very early months working with VASP.

I have to express my gratitude to *Dr. Florian Mittendorfer*, *Dr. Doris Vogtenhuber* and especially to my supervisor *Prof. Dr. Jürgen Hafner* for their cooperation all over the time and their ability to always give a clue when discussing materials science calculations. Furthermore, *Dr. Tomáš Bučko* has shown me in long discussions, how easily could materials science be understandable for a chemist.

I say thanks to my long-term office colleagues *Dr. Michal Jahnátek*, *Dr. Miroslav Čák*, *Assoc. Prof. Allan East*, *Dr. Martin Zelený*, *Dr. Cesare Franchini* and *MSc. Sowmya Murthy* for keeping scientifically-fruitful atmosphere in our office.

I thank to *Mrs. Edith Wolfsgruber* and *Mr. Michael Pöttl* for their kind support in bureaucracy-duties and computer administration, respectively.

Last but not least, note that this work has been financially supported by the Austrian Science Funds (FWF) through the Doctoral College "Computational Materials Science", project no. W004. This support is gratefully acknowledged.

David Karhánek



# Contents

<b>Acknowledgements</b>	<b>v</b>
<b>1 Introduction</b>	<b>1</b>
<b>2 Density Functional Theory</b>	<b>3</b>
2.1 The Schrödinger Equation . . . . .	3
2.2 The Born-Oppenheimer Approximation . . . . .	5
2.3 The Hohenberg-Kohn Theorem . . . . .	5
2.4 Kohn-Sham Theory . . . . .	6
2.5 Exchange-Correlation Functionals . . . . .	8
2.5.1 Hartree-Fock Theory of the Homogeneous Electron Gas . . . . .	8
2.5.2 Local-Density Approximation (LDA) . . . . .	9
2.5.3 Local-Spin-Density Approximation (LSDA) . . . . .	10
2.5.4 Generalized Gradient Approximation (GGA) . . . . .	10
2.6 The Bloch Theorem . . . . .	12
2.7 Planewaves and Pseudopotentials . . . . .	13
2.8 Analysis of the Electronic Properties . . . . .	15
2.8.1 Density of States (DOS) . . . . .	16

---

2.8.2	Charge Density Analysis . . . . .	17
2.9	The Hellmann-Feynman Theorem . . . . .	17
2.10	Optimization and Vibrational Analysis . . . . .	18
2.10.1	Static Optimization . . . . .	18
2.10.2	Vibrational Analysis . . . . .	20
2.10.3	Vibrational Properties Using DFPT . . . . .	21
2.11	Calculation of Reaction Barriers . . . . .	22
2.11.1	Improved Dimer Method . . . . .	23
<b>3</b>	<b>Adsorption on Solid Surfaces</b>	<b>25</b>
3.1	Adsorption by Experiment . . . . .	25
3.2	Adsorption by <i>Ab-Initio</i> Modeling . . . . .	28
3.2.1	The Slab Model . . . . .	29
3.2.2	The Adsorption Energy . . . . .	30
<b>4</b>	<b>Self-Assembled Monolayers</b>	<b>31</b>
4.1	The Phenomenon of Self-Assembly . . . . .	31
4.2	Kinetics and Mechanism of SAM growth . . . . .	33
4.3	Alkanethiol SAMs on Nickel . . . . .	34
4.4	Alkanethiol SAMs on Palladium . . . . .	36
4.5	Alkanethiol SAMs on Platinum . . . . .	36
<b>5</b>	<b>Computational Results</b>	<b>39</b>
5.1	Bulk Metals . . . . .	40
5.1.1	Preliminary Calculations . . . . .	40



---

5.1.2	Lattice Constants, Bulk Moduli and Cohesive Energies . . .	42
5.2	Clean (111)-Metal Surfaces . . . . .	46
5.2.1	Surface Relaxation . . . . .	47
5.2.2	Surface Energy . . . . .	48
5.2.3	Surface Workfunction . . . . .	49
5.3	Molecules and Molecule-Radicals . . . . .	52
5.3.1	Molecular Geometry . . . . .	52
5.3.2	Electronic Properties . . . . .	54
5.3.3	Vibrational Analysis . . . . .	60
5.4	Gas-Phase Dissociation of Methane Thiol . . . . .	69
5.5	Methane Thiol on (111)-Surfaces of Ni, Pd, Pt . . . . .	73
5.5.1	Adsorption Geometry . . . . .	73
5.5.2	Electronic Properties . . . . .	81
5.5.3	Vibrational Analysis . . . . .	84
5.6	Methane Thiolate on (111)-Surfaces of Ni, Pd, Pt . . . . .	94
5.6.1	Adsorption Geometry . . . . .	94
5.6.2	Electronic Properties . . . . .	105
5.6.3	Vibrational Analysis . . . . .	112
5.7	Comparison of Thiol and Thiolate Adsorption . . . . .	121
5.8	Dissociation of Methane Thiol on Metals . . . . .	122
<b>6</b>	<b>Conclusions</b>	<b>129</b>
	<b>Bibliography</b>	<b>133</b>

List of Publications	143
Conference Presentations and Seminars, Poster Sessions	145
Abstract	147
Zusammenfassung	149
Curriculum Vitae	151

# Chapter 1

## Introduction

The daily reality, based on consumption life-style, lets us easily forget about the concepts of the matter surrounding us. We just use what someone has produced for us. Nevertheless, it is always good to know what is the microscopic structure of the matter like, how the objects of daily used may be produced, and how they may be improved and protected in order to be useful for a long time. This is where science – in particular physics and chemistry – invest its time and money. There are experiments, facing the non-ideal properties of real world, and there is also the computational science, which may (and *does*) save a lot of experimental effort.

A foundation stone for this project has been discovered some 30 years ago. It was found out, than alkane thiols – in fact gases stinking after rotten eggs – undergo a surface reaction on gold, which was that time still reviewed as one of the least reactive (therefore “noble”) metals.

The thiols (also “mercaptoalcohols”) cover the metal surface perfectly and form a new organic interface over the metal surface. Although some applications are already used in technical practice (corrosion protection layers for easily-oxidizing metals, electrode-overlayers, molecular recognition surface for capturing sulfur containing aminoacids), there are still lack of knowledge how the organic molecules are bound to the metal surface.

Methane thiol is the prototype for the organic molecules, and it has been intensively studied on the “noble” gold surface. Comparative studies for several metals are however rather lacking. But right this is the way how to validate the results and make predictions. Concerning our study, the experimental results for adsorption on palladium were rather scarce.

Thus a big motivation for us to predict, how a small molecule behaves on that metal surface, whereas we verify its behavior on the elements neighboring in the periodic system (Ni and Pt), for which the experimental information is available.

This study is therefore also a proof of periodicity trends among the elements, as pronounced already early in 1869 by D.I. Mendeleev. Although relativistic effects (described much later, in 20<sup>th</sup> century) play here some role, we are able to distinguish a clear increase (or decrease) of adsorption energies and dissociation barriers for surface reactions on Ni-triad metals (group 8.B) in the periodic system of the elements.

$^{28}\text{Ni}$ $[\text{Ar}]3d^84s^2$
$^{46}\text{Pd}$ $[\text{Kr}]4d^{10}5s^0$
$^{78}\text{Pt}$ $[\text{Xe}]4f^{14}5d^96s^1$

The thesis comprises of 6 numbered chapters jeweled with a load of graphic material, followed by pre-requisites abstract in English and German, as well as author's personal info in appendix.

The introductory Chapter 1 sheds light on the field of research, that we decided to concern with. The Chapters 2-4 summarize the state of the art of the corresponding theory (background of *ab-initio* solid state calculations, Chapter 2) and experiments (adsorption in Chapter 3, self-assembly in Chapter 4). In contrast, the largest Chapter 5 contains the actual results of the computational project itself. These results are then briefly concluded in Chapter 6.

The readers are encouraged to enjoy their time when going through the text and to contact the author in case of any doubts or questions for discussion.

# Chapter 2

## Density Functional Theory

The density-functional theory (DFT) is nowadays the main tool of quantum mechanics, which allows to describe larger and larger systems as accurate as far the theory can go. The less approximations, the better description of real matter, no matter if it is solid, liquid or gaseous.

In the following, the Schrödinger equation as a basis for any quantum mechanical problem (i.e. also for Hartree-Fock methodology, which is anyway not used in this work), as well as the basis of the DFT itself as proposed already in the 1960's by Hohenberg, Kohn and Sham [1, 2] will be briefly stated, together with the relations and approximations for calculating periodic solids.

### 2.1 The Schrödinger Equation

Prediction of the electronic and geometric structure of a solid requires calculation of total energy of the system and subsequent minimization of that energy with respect to the electronic and nuclear coordinates.

If one looks at small atoms, the non-relativistic theory is a very good approximation, but when heavy atoms are involved, relativistic effects must be considered as well.

The Hamilton operator (**Hamiltonian**) describing a system of  $M$  nuclei and  $N$  electrons (Fig. 2.1) described by position vectors  $\vec{R}_A$  and  $\vec{r}_i$ , respectively, with a

pair (Coulomb) interaction between the components is given by:

$$\hat{H} = \hat{T}_A + \hat{T}_i + V_{A-i} + V_{i-i} + V_{A-A} \quad (2.1)$$

or (in atomic units, i.e.  $m_e = \hbar = e^2/(4\pi\epsilon_0) = 1$ , energy in Hartrees):

$$\hat{H} = - \sum_{A=1}^M \frac{1}{2M_A} \nabla_A^2 - \sum_{i=1}^N \frac{1}{2} \nabla_i^2 - \sum_{i=1}^N \sum_{A=1}^M \frac{Z_A}{|\vec{r}_{iA}|} + \sum_{i=1}^N \sum_{j>i}^N \frac{1}{|\vec{r}_{ij}|} + \sum_{A=1}^M \sum_{B>A}^M \frac{Z_A Z_B}{|\vec{R}_{AB}|} \quad (2.2)$$

The first two terms are the kinetic energy operators of the nuclei ( $\hat{T}_A$ ) and electrons ( $\hat{T}_i$ ); the third term ( $V_{A-i}$ ) represents the Coulomb interaction between electrons and nuclei; the fourth and fifth terms represent the electron-electron repulsion ( $V_{i-i}$ ) and ion-ion repulsion (repulsion between nuclei,  $V_{A-A}$ ), respectively.

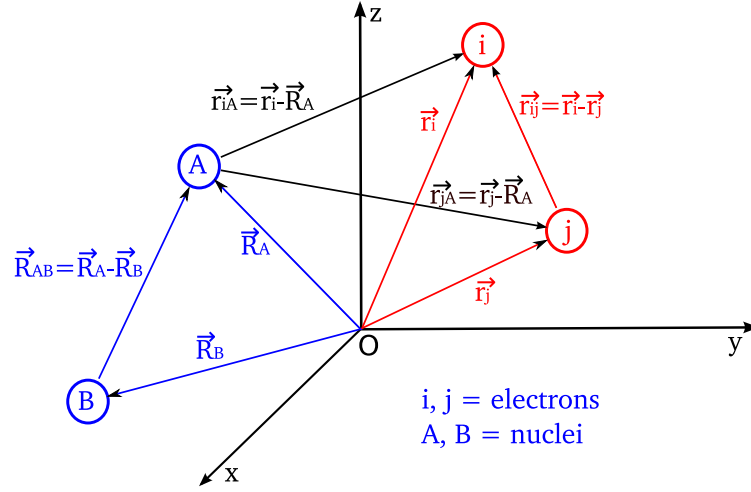


Figure 2.1: Representation of the coordinate system.

To find the total ground state energy, the **Schrödinger equation**, which is an eigenvalue problem:

$$\hat{H}\Psi = E\Psi \quad (2.3)$$

is solved under the constraint

$$\langle \Psi | \Psi \rangle = 1. \quad (2.4)$$

The eigenvalue  $E$  is the total energy of the system and is the total quantum state of this system. The symbol  $\Psi = \Psi(\vec{r}_1, \dots, \vec{r}_N; \vec{R}_1, \dots, \vec{R}_M)$  stands for a many-ion many-electron wavefunction. It is impossible to solve the equation 2.3 exactly (except for small systems up to  $\text{H}_2^+$ ) and several approximations have to be made, as will be described in the following chapters.

## 2.2 The Born-Oppenheimer Approximation

The *Born-Oppenheimer approximation* (or *adiabatic approximation*) focuses on the expression for the Hamiltonian (Eq. (2.1)) of a coupled many-ion many-electron system such as a molecule or a solid.

A starting point is the statement, that according to the huge difference in masses of nuclei and electrons ( $M_A/m_e \geq 10^4$ ), ionic and electronic processes proceed on a very different timescales. Namely the frequencies of ionic eigenvibrations in molecules and solids are of the order of magnitude of  $10^{12}$  Hz. Transitions between electronic eigenstates in atoms lead to emission of electromagnetic radiation in a frequency region of  $10^{17} - 10^{18}$  Hz.

One may therefore assume, that the electrons are irrespective of the ionic configuration always in their ground-state respective to the current position of ions in the ground state.

The subsystem of the electrons is described by the Schrödinger equation:

$$(T_i + V_{A-i}(\{\vec{R}_A\}) + V_{i-i})\psi(\vec{r}_1, \dots, \vec{r}_N) = E(\{\vec{R}_A\})\psi(\vec{r}_1, \dots, \vec{r}_N). \quad (2.5)$$

Here the ionic coordinates  $\vec{R}_A$  are here just external parameters and not dynamic variables. In the adiabatic approximation, the subsystem of ions is described by the Schrödinger equation:

$$(T_A + E(\{\vec{R}_A\}) + V_{A-A})\Phi(\vec{R}_1, \dots, \vec{R}_M) = E\Phi(\vec{R}_1, \dots, \vec{R}_M). \quad (2.6)$$

The ions are moving here in a field of a potential, which consists of the Coulomb-repulsion of ions  $V_{A-A}$  and the energy of the electrons in the field of ions  $E(\{\vec{R}_A\})$ . Thanks to the enormous mass of the ions, quantum effects may be *neglected* (exception: liquid and solid helium and hydrogen) and the Schrödinger equation may be replaced by the classical Newton equation of motion.

## 2.3 The Hohenberg-Kohn Theorem

The Hohenberg-Kohn theorem applies to any system consisting of electrons moving under the influence of an external potential.

Stated simply they are as follows:

**Theorem 1** (existence theorem)

The total energy of a many electron system in an external potential  $V_{ext}(\vec{r})$  is a unique functional of the electron density  $\rho(\vec{r})$ .

$$E[\rho(\vec{r})] = \int d^3\vec{r} \rho(\vec{r}) V_{ext}(\vec{r}) + F[\rho(\vec{r})] \quad (2.7)$$

where the first term describes the interaction with the external potential, and  $F[\rho(\vec{r})]$  is an unknown, but otherwise universal functional of the electron density only describing the kinetic and electron-electron interaction energies.

**Theorem 2** (variational principle)

In the ground state, the functional  $E[\rho(\vec{r})]$  has its minimum relative to all variations of the density.

$$E_0[\rho(\vec{r})] = \min E[\rho(\vec{r})] \quad \Longleftrightarrow \quad \left. \frac{\partial E[\rho(\vec{r})]}{\partial \rho(\vec{r})} \right|_{\rho(\vec{r})=\rho_0(\vec{r})} = 0 \quad (2.8)$$

Although the Hohenberg-Kohn theorems are in principle extremely powerful, they do not offer a way of computing the ground-state density of a system in practice, because the exact form of the functional  $F[\rho(\vec{r})]$  is unknown. About one year after the key DFT paper by Hohenberg and Kohn [1], Kohn and Sham derived a simple method for carrying out DFT calculations, that retains the exact nature of DFT (see Chapter 2.4).

## 2.4 Kohn-Sham Theory

The approach of Kohn and Sham [2], published in 1965, turns DFT into a practical tool to obtain the ground state.

The Kohn-Sham method is based on parameterization of the density  $\rho(\vec{r})$  in terms of one-electron orbitals  $\phi_i(\vec{r})$  (the summation is over all occupied states):

$$\rho(\vec{r}) = \sum_i \phi_i^*(\vec{r}) \phi_i(\vec{r}) \quad (2.9)$$

and a decomposition of the total energy functional according to:

$$E[\rho] = T[\rho] + E_H[\rho] + E_{xc}[\rho] + E_{ext}[\rho] \quad (2.10)$$

where

$$E_H = \iint \frac{\rho(\vec{r})\rho(\vec{r}')}{|\vec{r} - \vec{r}'|} d\vec{r} d\vec{r}' \quad (2.11)$$



is the electrostatic electron-electron interaction in the Hartree approximation, while

$$E_{ext} = \int V_{ext}(\vec{r})\rho(\vec{r})d\vec{r} \quad (2.12)$$

describes the interaction with the external field.

The contribution of the kinetic energy is approximated by that of non-interacting electron in states  $\phi_i(\vec{r})$ ,

$$T[\rho] = \sum_i \int \phi_i^*(\vec{r})\left(-\frac{1}{2}\vec{\nabla}^2\right)\phi_i(\vec{r})d^3r. \quad (2.13)$$

All other contributions to the total energy are described by the so-called exchange-correlation energy  $E_{xc}[\rho]$ . The one-electron orbitals are the variational quantities. Variation of the total energy functional  $E[\rho]$  with respect to  $\phi_i^*(\vec{r})$  leads to an effective one-electron equation for the determination of the  $\phi_i(\vec{r})$ , the **Kohn-Sham equations**:

$$\left(-\frac{1}{2}\vec{\nabla}^2 + \int \frac{\rho(\vec{r}')}{|\vec{r}-\vec{r}'|}d^3r' + V_{ext}(\vec{r}) + \frac{\delta E_{xc}[\rho(\vec{r})]}{\delta\rho(\vec{r})}\right)\phi_i(\vec{r}) = \epsilon_i\phi_i(\vec{r}). \quad (2.14)$$

The Kohn-Sham equations describe electrons moving in an one-electron potential given by

$$V_{eff}(\vec{r}) = V_{ext}(\vec{r}) + \int \frac{\rho(\vec{r}')}{|\vec{r}-\vec{r}'|}d^3r' + V_{xc}[\rho(\vec{r})], \quad (2.15)$$

where the exchange correlation potential is given by the variational derivation of the exchange-correlation energy,

$$V_{xc}[\rho(\vec{r})] = \frac{\delta E_{xc}[\rho(\vec{r})]}{\delta\rho(\vec{r})}. \quad (2.16)$$

The  $\epsilon_i$  in (2.14) are introduced as Lagrange parameters to preserve the orthogonality of the one-electron Kohn-Sham orbitals

$$\int \phi_i^*(\vec{r})\phi_j(\vec{r})d^3r = \delta_{ij}, \quad (2.17)$$

they are not true excitation energies.

## 2.5 Exchange-Correlation Functionals

### 2.5.1 Hartree-Fock Theory of the Homogeneous Electron Gas

Within Hartree-Fock theory, the many-body wavefunction of the  $N$ -electron system is approximated by an antisymmetric product (a Slater determinant) of one-electron orbitals. For an electron gas in a homogeneous compensating positive background charge, the Hartree-Fock equations may be solved exactly. The ground-state energy for electron is given by

$$E_0 = \frac{3}{5}E_F - \frac{3}{4\pi}k_F = \frac{3}{5}(3\pi^2\rho_0)^{2/3} - \frac{3}{4\pi}(3\pi^2\rho_0)^{1/3}, \quad (2.18)$$

it is a *function* of the homogeneous electron density  $\rho_0$ . The first term describes the contribution of the kinetic energy, the second the *exchange* energy which is found to be proportional to the cube root of the electron density.

The *correlation energy* is defined as an energy difference between the exact ground-state energy of the interacting many-electron system and the Hartree-Fock ground-state energy. Even for a homogeneous electron gas, the exact solution for the many-electron system can be found only through elaborate Quantum Monte Carlo (QMC) simulations. Perdew and Zunger [3] have parameterized QMC simulations of Ceperley and Alder [4], leading to a correlation energy as a function of electron density given by

$$E_c = \frac{\gamma}{1 + \beta_1 r_s^{1/2} + \beta_2 r_s} \quad (2.19)$$

or

$$E_c = A \ln r_s + B + C r_s \ln r_s + D r_s, \quad (2.20)$$

depending on if applied to regions of low-density [(2.19),  $r_s > 1$ ] or high-density [(2.20),  $r_s < 1$ ], whereas the quantity  $r_s$  is a convenient measure of the electron density, defined as the radius of the sphere containing the volume per electron,

$$r_s = \sqrt[3]{\frac{3}{4\pi\rho}} \quad (2.21)$$

and the parameters used in (2.19) are  $\gamma = -0.1423$ ,  $\beta_1 = 1.0529$ ,  $\beta_2 = 0.3334$  and in Eq. (2.20), the parameter set  $A, B, C, D$  was found to be  $A = 0.0311$ ,  $B = -0.048$ ,  $C = 0.0020$ ,  $D = -0.0116$ . As the correlation function is discontinuous in  $r_s = 1$ , it has irregularities in this region. Therefore, several improvements have been proposed, such as e.g. by Koures and Harris (KH) [5].

### 2.5.2 Local-Density Approximation (LDA)

The oldest, simplest and probably the most important functional is the local density approximation (LDA), which was proposed by Hohenberg and Kohn in their original DFT paper [1]. The LDA consists of locally approximating the true exchange-correlation energy of a system by the exchange-correlation energy associated with a homogeneous electron gas of the same density. The homogeneous gas is the only system for which the form of the exchange-correlation energy is known precisely.

The LDA is only dependent on the local density, and the total energy is commonly written as

$$E_{xc}^{LDA}[\rho(\vec{r})] = \int d^3\vec{r} \rho(\vec{r}) \epsilon_{xc}[\rho(\vec{r})] \quad (2.22)$$

where  $\epsilon_{xc}[\rho(\vec{r})]$  is the exchange-correlation energy density corresponding to a homogeneous electron gas of density  $\rho(\vec{r})$ .

A symbolic graphical description of the local character of LDA approximation is shown in Fig. 2.2.

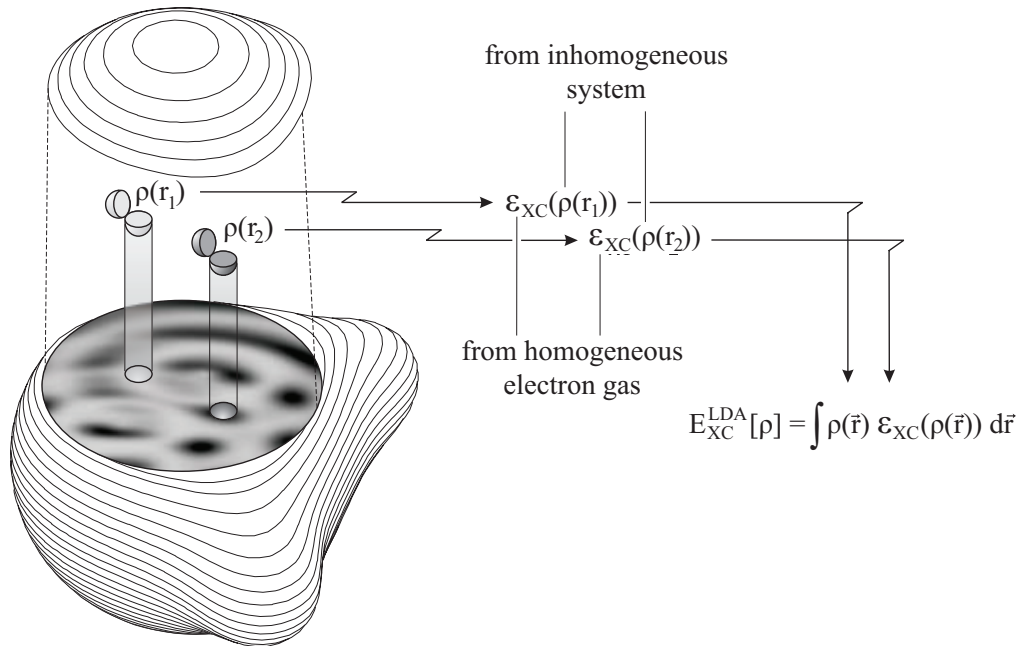


Figure 2.2: *The local density approximation (reprint from Ref. [7]).*

### 2.5.3 Local-Spin-Density Approximation (LSDA)

The extension of LDA functional to spin-polarized systems is important especially for correct description of elements expressing magnetism. The formulation is straightforward for exchange energy part, where the exact spin-scaling is known, but for correlation energy term further approximations must be employed.

A spin polarized system in DFT employs two spin-densities,  $\rho_\alpha$  and  $\rho_\beta$  with the total  $\rho = \rho_\alpha + \rho_\beta$ , and the form of the *local-spin-density approximation (LSDA)* [9] is as follows:

$$E_{xc}^{LSDA}[\rho_\alpha(\vec{r}), \rho_\beta(\vec{r})] = \int d^3\vec{r} \rho(\vec{r}) \epsilon_{xc}[\rho_\alpha(\vec{r}), \rho_\beta(\vec{r})] . \quad (2.23)$$

For the exchange energy, the exact result (not just for local density approximations) is known in terms of the spin-unpolarized functional [8]:

$$E_x[\rho_\alpha, \rho_\beta] = \frac{1}{2} \left( E_x[2\rho_\alpha] + E_x[2\rho_\beta] \right) . \quad (2.24)$$

The spin-dependence of the correlation energy density is approached by introducing the relative spin-polarization:

$$\zeta(\mathbf{r}) = \frac{\rho_\alpha(\vec{r}) - \rho_\beta(\vec{r})}{\rho_\alpha(\vec{r}) + \rho_\beta(\vec{r})} . \quad (2.25)$$

A value of  $\zeta = 0$  corresponds to the paramagnetic spin-unpolarized situation with equal  $\alpha$ , and  $\beta$ , spin densities, whereas  $\zeta = \pm 1$  corresponds to the ferromagnetic (fully polarized) situation where one spin density vanishes. The spin correlation energy density for a given values of the total density and relative polarization,  $\epsilon_c(\rho, \zeta)$ , is constructed so to interpolate the extreme values. Several forms have been developed in conjunction with LDA correlation functionals [9, 10].

### 2.5.4 Generalized Gradient Approximation (GGA)

Hohenberg and Kohn presumed that the LDA would be too simple to work for real systems and so proposed an extension to the LDA known as the gradient expansion approximation (GEA) [1]. The GEA is a series expansion of increasingly higher order density gradient terms. The first order form of the GEA was subsequently implemented and tested for atoms and molecules and was a complete failure. Anyway, GEA provided the basis for the generalized gradient approximation (GGA),

which is currently the most used exchange-correlation functional in computational material physics.

The vital steps that lead to the GGA were principally made by Perdew and co-workers [6] who devised a cutoff procedure that sharply terminates the GEA exchange-correlation hole in real-space using delta functions, in order to restore the sum rule and non-positivity hole conditions. As a result of this procedure the GGA can be conveniently written in terms of an analytic function known as the enhancement factor,  $F_{xc}[\rho(\vec{r}), \nabla\rho(\vec{r})]$ , that directly modifies the LDA energy density,

$$E_{xc}^{GGA}[\rho(\vec{r})] = \int d^3\vec{r} \rho(\vec{r}) \epsilon_{xc}^{hom}(\rho(\vec{r})) F_{xc}[\rho(\vec{r}), \nabla\rho(\vec{r})]. \quad (2.26)$$

Using GGA, very good results for molecular geometries and ground-state energies have been achieved. In recent years, several GGA implementations have shown their efficiency and became a kind of standard choice for calculations, namely in chronological order: Perdew-Wang (PW86) [14], Perdew-Wang (PW91) [12], Perdew-Burke-Ernzerhof (PBE) [16], Hammer-Hansen-Nørskov (RPBE) [17] *etc.*

Potentially more accurate than the GGA functionals are the *meta*-GGA functionals. These include a further term in the expansion, depending on the density, the gradient of the density and the Laplacian (second derivative) of the density.

Difficulties in expressing the exchange part of the energy can be relieved by including a component of the exact exchange energy calculated from Hartree-Fock theory. Functionals of this type are known as hybrid functionals, such as those by Perdew-Burke-Ernzerhof (PBE0) [19], or Heyd-Scuseria-Ernzerhof (HSE03) [20].

In the following, the **PW91** functional will be described in more detail, since it was used for the calculation presented later in this thesis. As published by Perdew and Wang in 1991 [12], this model was based solely on the data for an homogeneous electron gas [4] and relations which appeared to be important for constructing functionals. It contains an cutoff in the direct space (in contrast to PW86 functional). The exchange functional is an improvement of that by Becke [21]. PW91 fulfils almost all conditions for GGA functionals, even those discovered after its origination. The exchange functional has the form

$$\epsilon_x^{PW91}(\rho) = \epsilon_x^{LDA}(\rho) \left[ \frac{1 + a_1 s \sinh^{-1}(a_2 s) + (a_3 + a_4 \exp(-100s^2))s^2}{1 + a_1 s \sinh^{-1}(a_2 s) + a_5 s^4} \right] \quad (2.27)$$

where  $a_1 = 0.19645$ ,  $a_2 = 7.7956$ ,  $a_3 = 0.2743$ ,  $a_4 = -0.1508$ ,  $a_5 = 0.004$ . The correlation functional is approximated as

$$\epsilon_c^{PW91}(\rho) = \epsilon_c^{LDA}(\rho) + H(\rho, s, t) \quad (2.28)$$

where  $H(\rho, s, t)$  is a function of density  $\rho$  and energy gradients  $s = |\nabla\rho|/(2k_F\rho)$  (applied already in Eq. (2.27)) and  $t = |\nabla\rho|/(2k_s\rho)$  (where  $k_F = \sqrt[3]{3\pi^2\rho}$  is the local Thomas-Fermi wavevector):

$$H(\rho, s, t) = \frac{\beta^2}{2\alpha} \log \left[ 1 + \frac{2\alpha}{\beta} \frac{t^2 + At^4}{1 + At^2 + A^2t^4} \right] + C_{c0}[C_c(\rho) - C_{c1}]t^2 e^{-100s^2} \quad (2.29)$$

and the factor  $A$  is

$$A = \frac{2\alpha}{\beta} \left[ \exp \left( -2\alpha \frac{\epsilon_c^{LDA}(\rho)}{\beta^2\rho} \right) - 1 \right]^{-1} \quad (2.30)$$

and  $\alpha = 0.09$ ,  $\beta = 0.0667263212$ ,  $C_{c0} = 15.7559$ ,  $C_{c1} = 0.003521$ , whereas the function  $C_c(\rho)$  is defined as

$$C_c(\rho) = C_1 + \frac{C_2 + C_3 r_S + C_4 r_S^2}{1 + C_5 r_S + C_6 r_S^2 + C_7 r_S^3} \quad (2.31)$$

where and  $r_S = (4/3\pi\rho)^{-1/3}$  is the local Seitz parameter defined already in Eq. (2.21) and the constants have the values  $C_1 = 1.667 \cdot 10^{-3}$ ,  $C_2 = 2.568 \cdot 10^{-3}$ ,  $C_3 = 2.3266 \cdot 10^{-2}$ ,  $C_4 = 7.389 \cdot 10^{-6}$ ,  $C_5 = 8.723$ ,  $C_6 = 4.72 \cdot 10^{-1}$ , and  $C_7 = 7.389 \cdot 10^{-2}$ . The PW91 model contains, however, several minor insufficiencies, which have been removed in the forthcoming PBE model.

## 2.6 The Bloch Theorem

In order to use DFT calculations on infinite systems (such as solids are), one assumes that the structure of the system is homogeneous in all directions and introduces the periodic boundary conditions (PBC). For the set of coordinates of atomic nuclei, we introduce a supercell that involves the periodically repeated pattern of atoms obeying translational symmetry rules.

The **Bloch theorem** [22] states, that the eigenvalues in a periodic solid have the form

$$\psi_{n\vec{k}}(\vec{r}) = e^{i\vec{k}\cdot\vec{r}} u_{n\vec{k}}(\vec{r}), \quad (2.32)$$

where  $n$  is the ‘‘band index’’ and  $\vec{k}$  a wavevector confined to the first Brillouin zone of the reciprocal lattice.  $u_{n\vec{k}}$  is translationally invariant, i.e.

$$u_{n\vec{k}}(\vec{r} + \vec{R}_e) = u_{n\vec{k}}(\vec{r}), \quad (2.33)$$

where  $\vec{R}_e$  is a vector of the crystal lattice. Eigenstates of this form are called *Bloch functions*. Under a translation by a lattice vector  $\vec{R}_e$ , Bloch functions transform according to

$$T_{vecR_e}\psi_{n\vec{k}}(\vec{r}) = \psi_{n\vec{k}}(\vec{r} + \vec{R}_e) = e^{i\vec{k}\vec{R}_e}\psi_{n\vec{k}}(\vec{r}). \quad (2.34)$$

Bloch functions  $\psi_{n\vec{k}}$  and their eigenvalues are periodic in  $\vec{k}$ -space,

$$\psi_{n,\vec{k}+\vec{K}}(\vec{r}) = \psi_{n\vec{k}}(\vec{r})E_{n,\vec{k}+\vec{K}}(\vec{r}) = E_{n\vec{k}}(\vec{r}). \quad (2.35)$$

where  $\vec{K}$  is an arbitrary reciprocal lattice vector.

Hence it is sufficient to consider them and their eigenvalues only in the first Brillouin-zone. Deriving the Schrödinger equation with Bloch functions yields an equation for an periodic function  $\psi_{\vec{k}}(\vec{r})$ . Using periodic boundary conditions leads to a Hermitian eigenvalue equation over the Wigner-Seitz cell in the crystal. For a fixed  $\vec{k}$ , there is an infinite number of solutions with raising energy values.

## 2.7 Planewaves and Pseudopotentials

The electron orbitals used to express the single particle density as defined in Eq. (2.14) may be expanded in terms of any convenient basis set. In practice, a plane wave basis set

$$\psi_{\vec{k}}^n(\vec{r}) = \sum_{\vec{K}} c_{\vec{K}}^{n,\vec{k}} e^{i(\vec{k}+\vec{K})\cdot\vec{r}}. \quad (2.36)$$

based on the Bloch theorem (Chapter 2.6) is used with a number of benefits:

- A planewave basis set is unbiased, it does not assume any preconceptions on the form of the problem.
- Due to Bloch theorem, planewaves are the natural choice for the representation of electron orbitals in a periodic system.
- The kinetic energy operator is diagonal in a planewave representation. Similarly the potential is diagonal in real space. The use of Fast Fourier Transforms (FFT) in changing between these representations provides a large saving in computational cost.

The main disadvantage of a planewave basis set is its inefficiency. The number of basis functions required to describe atomic wavefunctions accurately near to a nucleus would be enormous.

This difficulty is overcome by the use of **pseudopotentials** [24], which represent the potential of the ionic cores. This approximation is based on the assumption that only the valence electrons have significant effect the physical and chemical properties of the system. The pseudopotential represents the potential of the nucleus and the core electrons subject to the following conditions:

- The valence wavefunction remains unchanged outside the core region (beyond  $r_c$  boundary).
- The pseudo wavefunction within the core matches correctly at the boundary.
- The pseudo wavefunction, as well its first derivative, must be continuous at the boundary:

$$\phi^{PS}(r)|_{r=r_c} = \phi^{AE}(r)|_{r=r_c} \quad \wedge \quad \frac{\partial \phi^{PS}}{\partial r}(r)|_{r=r_c} = \frac{\partial \phi^{AE}}{\partial r}(r)|_{r=r_c} \quad (2.37)$$

(the indices *PS* and *AE* stand for pseudo and all-electron energies, respectively).

- The pseudo wavefunction is nodeless within the core region.

The graphical representation of the behavior of a wavefunction and potential is depicted in Fig. 2.3. All the above-mentioned basic criteria have to be fulfilled for the pseudopotential to be usable. Further criteria have to be introduced for constructing various classes of pseudopotentials, such as ultra-soft (or Vanderbilt) pseudopotentials (USPP), norm-conserving pseudopotentials (NCP) etc.

The so-called **projector-augmented wave method** (PAW) [119] is an improvement of the pseudopotential technique approach and was originally developed by P. Blöchl [26]. It is based on a transformation of the pseudo wavefunction to the all-electron wavefunction. The all-electron wavefunction  $\psi$  consists of three parts:

$$\psi = \tilde{\psi} + \sum_i^N c_i \phi_i - \sum_i^N c_i \tilde{\phi}_i \quad (2.38)$$

where  $\tilde{\psi}$  is the pseudo wavefunction,  $\phi_i$  are the all-electron partial waves and  $\tilde{\phi}_i$  are the pseudo partial waves. A tilde is used to distinguish between the all-electron (AE) quantities and the pseudo (PS) quantities (such as  $\tilde{\psi}$ ) representing only one part of the AE solution.

The PS wavefunction is represented by planewaves that are a good description of the wavefunction in regions far away from the nuclei, but deviates significantly



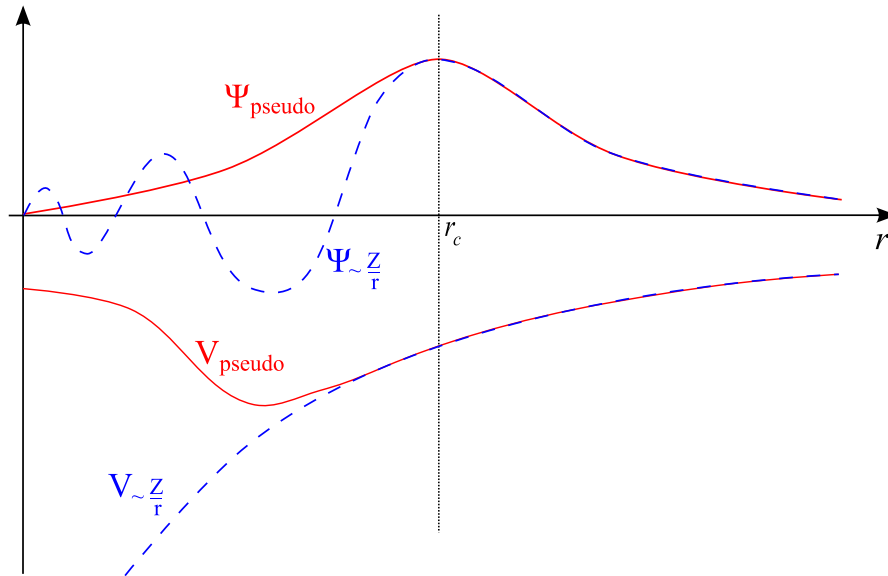


Figure 2.3: Comparison of a wavefunction in the Coulomb potential of the nucleus (blue) to the one in the pseudopotential (red). The real and the pseudo wavefunction and potentials match above a certain cutoff radius (core radius)  $r_c$ . Sketch inspired by Ref. [25].

from the AE wavefunction near the nucleus. Hence the AE partial waves  $\phi_i$  are introduced to correct this error. These AE partial waves are calculated once as solutions of the radial part of the Schrödinger equation for the isolated atoms. Inside the so-called augmented (core) region, they deviate from the PS wavefunction, however outside this region they match. The AE partial waves ensures that the nodal structure of the wavefunction is physically correct near the nucleus.

The contribution of the PS partial waves  $\tilde{\phi}_i$ , which are located near the atomic nuclei is subtracted from the PS wavefunction since this region is already included in the AE partial waves. Similar to the AE partial waves, the  $\tilde{\phi}_i$  are constructed as solutions of the radial Schrödinger equation for isolated atoms fitted to match the PS wavefunction.

## 2.8 Analysis of the Electronic Properties

There are powerful tools for analyzing the electronic structure and properties offered by the state-of-the-art computational materials science. Few of them will be mentioned here, in particular the density of states and charge density analysis.

### 2.8.1 Density of States (DOS)

An important quantity for many purposes is the **density of states (DOS)** per unit of energy  $E$  (and per unit of volume  $\omega$  in extended matter) [27],

$$n(E) = \frac{1}{N_k} \sum_i \sum_{\vec{k}} \delta(\epsilon_{i,\vec{k}} - E) = \frac{\omega_{cell}}{(2\pi)^d} \int_{BZ} \delta(\epsilon_{i,\vec{k}} - E) d\vec{k}. \quad (2.39)$$

In the case of independent-particle states, where  $\epsilon_{i,\vec{k}}$  denotes the energy of an electron (or phonon),  $\rho(E)$  from (2.39) is the number of independent-particle states per unit energy.

In principle, the calculation of integral in (2.39) is not a trivial task. Three popular types of methodologies for this Brillouin zone integration are mentioned here: namely the linear tetrahedron method (LTM) by Jepsen and Andersen [28], modified tetrahedron method (MTM) by Blöchl et al. [29] and the Gaussian broadening method (GBM) by Methfessel and Paxton [30].

The total density of states as defined by (2.39) is in fact a projection of all bands of the electronic bandstructure over all  $k$ -points. As one wishes to analyze space-resolved DOS in the real space, the **local density of states (LDOS)** may be defined as follows:

$$n(\vec{r}, E) = \sum_i \sum_{\vec{k}} |\Psi_{i\vec{k}}(\vec{r})|^2 \delta(\epsilon_{i,\vec{k}} - E). \quad (2.40)$$

In order to study the interaction of atoms with each other, we define the **projected density of states (PDOS)**:

$$n(\alpha, E) = \sum_i \sum_{\vec{k}} |\langle \Psi_{\alpha\vec{k}}(\vec{r}) | \Psi_{i\vec{k}}(\vec{r}) \rangle|^2 \delta(\epsilon_{i,\vec{k}} - E), \quad (2.41)$$

where  $\Psi_{\alpha\vec{k}}$  denotes orthonormal states to  $\Psi_{i\vec{k}}$ . The PDOS is in principle a projection of the DOS onto atomic orbitals.

When plotting DOS spectra, an attention is given to the position of the zero-point. The **Fermi Energy**  $E_F$  refers to the energy of the highest occupied quantum state in a system of fermions at absolute zero temperature.

As the Fermi energy  $E_F$  appears in all DOS spectra, it used to be shifted to zero energy level in *periodic systems*, where the spectrum is usually continuous.

For *molecules* or other localized clusters, the Fermi energy is arbitrarily shifted to the value  $E_F = \frac{1}{2}(E_{HOMO} + E_{LUMO})$ , i.e. to the average value between the lowest-

unoccupied (LUMO) and highest-occupied (HOMO) electronic state. Molecules usually have electronic states at discrete energy values, thus giving bar diagrams.

### 2.8.2 Charge Density Analysis

The charge density in general is defined as the amount of charge in a specified volume. As it depends on the position vector  $\vec{r}$ , in quantum mechanics it can refer to the spatial charge distribution over the volume of a molecule or a unit cell of a periodic solid.

The electronic charge density is related to the wavefunction by the equation

$$\rho(\vec{r}) = e^2 \sum_{n\vec{k} \in \text{occ}} |\psi_{n\vec{k}}(\vec{r})|^2, \quad (2.42)$$

where  $e$  is the charge of electron ( $e = 1.6021733 \cdot 10^{-19}$  Coulomb),  $\psi_{n\vec{k}}(\vec{r})$  is the wavefunction of the  $n$ -th electron band and the sum in (2.42) goes over occupied electronic states only.

The visualization of the charge density is helpful for elucidating the bonding of atoms to each other and it is preferably made by the means of plotting 3D isosurfaces (a surface for a discrete isovalue) or 2D contour plots (a set of isocontours).

## 2.9 The Hellmann-Feynman Theorem

The Hellmann-Feynman theorem (proved independently by H. Hellmann in 1937 [31] and R. Feynman in 1939 [32]) relates to a derivative of the total energy of a system in the electronic ground state, and is usually applied to calculate forces acting on atoms. It shows that for a system in its ground state, the force on an ion is the equal to the expectation value of the derivative of the Hamiltonian  $\hat{H}$  with respect to that ion position.

Let  $\psi$  be the eigenvectors of the Hamiltonian, then the derivative of energy with respect to an arbitrary parameter  $\lambda$  is given by

$$\frac{\partial E}{\partial \lambda} = \frac{\partial}{\partial \lambda} \langle \psi | H | \psi \rangle = \left\langle \frac{\partial \psi}{\partial \lambda} | H | \psi \right\rangle + \langle \psi | H | \frac{\partial \psi}{\partial \lambda} \rangle + \langle \psi | \frac{\partial H}{\partial \lambda} | \psi \rangle \quad (2.43)$$

and since for the ground state, the following terms neglect

$$\left\langle \frac{\partial \psi}{\partial \lambda} | H | \psi \right\rangle \Big|_{\psi=\psi_0} + \langle \psi | H | \frac{\partial \psi}{\partial \lambda} \rangle \Big|_{\psi=\psi_0} = 0$$

one may write that the forces acting on the atoms are

$$\vec{F} = -\frac{\partial E}{\partial \vec{R}} = -\frac{d}{d\vec{R}}\langle\psi|H|\psi\rangle = -\langle\psi|\frac{\partial H}{\partial \vec{R}}|\psi\rangle. \quad (2.44)$$

This allows the force, as well as the energy, to be calculated for a given atomic configuration without recalculating the electronic states, or finding their derivatives. This makes force calculations (see Section 2.10.2) simple and more manageable in terms of time.

## 2.10 Structure Optimization and Vibrational Analysis

### 2.10.1 Static Optimization of Molecular and Crystal Structures

The crucial point when performing *ab-initio* calculations is to find the electronic ground state of the system, i.e. particular arrangement of atoms corresponding to the lowest potential energy. Hence expressions “structure optimization” (or “relaxation”) and “energy minimization” are in fact synonymous.

In principle, when searching for the optimal geometry, the quantum-mechanical code performs several *ionic relaxation steps*, i.e. that it moves all nuclei to an appropriate directions (according to energy gradients), in which each nucleus should have lower potential energy. After each ionic step, the ground state energy of this particular atomic arrangement has to be evaluated by the means of a self-consistent cycle of *electronic relaxation steps*.

Once the difference of any 2 consecutive energy values is lower than a given threshold value, the self-consistent cycle is finished, and new positions of atoms are proposed, unless the energy gradients (or forces on atoms) are lower than pre-defined threshold values (accuracy condition given by the user).

For finding the ground state according to the energy and its gradients, the following numerical algorithms are widely spread in periodical *ab-initio* codes:

- *Steepest descent* method
- *Conjugate-gradient* (CG) method
- *Residual minimization* method (RMM)

Visualization scheme of search paths for locating the minimum of the function (in this case, Kohn-Sham energy functional) by an iterative process using the steepest descent and conjugate gradient methods is shown in Fig. 2.4. In the steepest de-

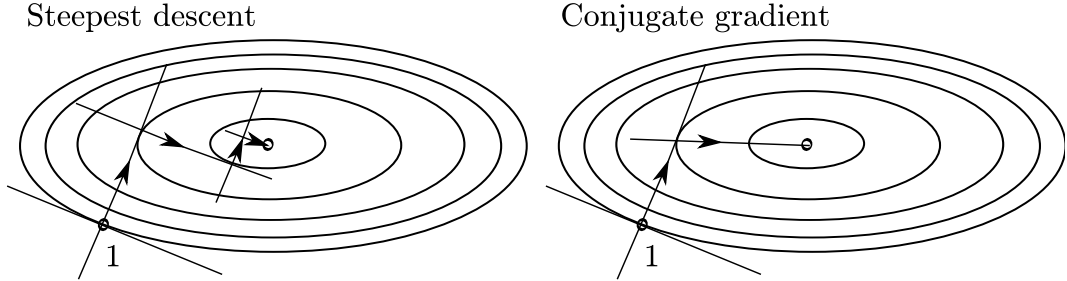


Figure 2.4: Sketch of the search paths for the minimum of a function (i.e. energy) using the steepest descent (left) and conjugate-gradient approach (right). In both cases, the search begins at point 1. The conjugate-gradient method converges faster. (after Ref. [33]).

scent procedure, one starts at an arbitrary point in a multidimensional space (e.g. point 1 in Fig.2.4) and evaluates the gradient of the function [33]. The negative of the gradient vector gives the direction of the steepest descent which is followed until a minimum is reached along this line. At that point, the procedure is repeated until the value can no longer be lowered within a given convergence threshold. It is evident in Fig.2.4 that this is a reasonable, but not optimal search strategy. A more efficient approach is the conjugate gradient (CG) method, which first also starts along the line of steepest descent. However, in the following step, the search direction contains information not only from the gradient at the current point, but also from the previous gradient in the form  $\vec{d}_m = \vec{g}_m + \gamma_m \vec{g}_{m-1}$ , with  $\vec{d}_m$  being the search direction in step  $m$  and  $\vec{g}_m$  is the steepest descent direction at point  $m$ :

$$\vec{g}_m = - \left. \frac{\partial \varepsilon_{KS}(\vec{x})}{\partial \vec{x}} \right|_{\vec{x}=\vec{x}_m}, \quad (2.45)$$

where the function to be minimized  $\varepsilon_{KS}$  is the Kohn-Sham energy functional, and the introduced coefficient  $\gamma_m$  is defined by:

$$\gamma_m = - \frac{\vec{g}_m \cdot \vec{g}_m}{\vec{g}_{m-1} \cdot \vec{g}_{m-1}} \quad (2.46)$$

with the initial condition  $\gamma_1 = 0$ .

For a variety of purposes, one prefers to locate the ground state according to threshold of residual forces on atoms (accessible with the help of Hellmann-Feynman theorem) rather than the energy threshold. After the Kohn-Sham ground state of the system is found, various electronic and optical properties may be evaluated.

### 2.10.2 Vibrational Analysis of Molecular and Adsorbate Structures

The vibrational eigenmodes of molecules and adsorbate complexes (consisting of the molecules and the substrate atoms to which the molecules are anchored) have been calculated in the *harmonic approximation* [34], using a *direct force constant approach*.

The displacements of a single atom in the molecule or adsorption complex by a vector  $\vec{u}(l)$  ( $l$  labels the atom) induces forces  $\vec{F}(ml)$  acting on the surrounding atoms which are calculated using the Hellmann-Feynman theorem. In the second step, all symmetry operations  $S$  of the point group of the molecule are applied to the displacement vector  $\vec{u}(l)$  and to the force field.

Generally, applying  $S$  on  $\vec{u}(l)$  rotates the vector and eventually shifts its origin to another atom of the molecule. If the displacement vector is linearly independent of all previously generated vectors,  $S\vec{u}(l)$  and  $S\vec{F}(ml)$  are stored in datafields  $\vec{u}_i(l)$  and  $\vec{F}_i(ml)$ .

If, after applying all point group operations, a set of three linearly independent displacement vectors and a set of three force fields has been generated for each atom, an orthogonal transformation to a set of orthogonal displacement vectors  $\tilde{u}_\alpha(l)$ ,  $\alpha = 1, 2, 3$ , oriented along Cartesian axes is performed and the same transformation is also applied to the force field,  $\tilde{F}_\alpha(ml)$ .

In the harmonic approximation, the *force constant matrix* (*Hessian matrix*) is then given by

$$\phi_{\alpha\beta}(lm) = -\frac{\tilde{F}_\beta(ml)}{\tilde{u}_\alpha(l)}, \quad (2.47)$$

and as a final step, the calculated force constant matrix is symmetrized with respect to all point group operations.

The *dynamical matrix* is given by

$$D_{\alpha\beta}(lm) = -\frac{1}{\sqrt{M_l M_m}} \phi_{\alpha\beta}(lm), \quad (2.48)$$

the vibrational eigenmodes are characterized by the *eigenvalues*  $\omega_\beta^2$  as well as the *eigenvectors*  $\vec{e}_\beta(l)$  of the dynamical matrix, evaluated as a solution of the equation of motion

$$\vec{D} \cdot \vec{u} = \omega^2 \vec{u}. \quad (2.49)$$

Experimental representation of the vibrational properties of molecules and adsorption complex is available from electron energy loss spectroscopy (EELS) and infrared absorption spectroscopy. The wavenumbers and intensities of the vibrational normal modes are then directly comparable with experimental results.

Furthermore, the calculation of vibrational (or, for solid state materials: phonon) spectra has a use for checking the structure to be in the ground state. In the ground state, there should be no imaginary vibrational frequencies. For a transition state, there should be exactly one “hard” (high-frequency) imaginary vibrational mode, whose eigenvectors show on breaking old chemical bonds and forming new ones.

### 2.10.3 Vibrational Properties Using DFPT

Recently, the theory atoms’ response to electric fields has become applicable for interpreting macroscopic parameters such as linear optical properties [35] – the static dielectric tensor, the piezoelectric tensor, the vibrational frequencies and the matrix of the Born effective charges.

Density-functional perturbation theory (DFPT) or linear response (LR) theory for vibrational spectra starts from the following expression [36, 37]:

$$\frac{\partial^2 E(\vec{R})}{\partial \vec{R}_i \partial \vec{R}_j} \equiv \frac{\partial \vec{F}_i}{\partial \vec{R}_j} = \int \frac{\partial \rho_{\vec{R}}(\vec{r})}{\partial \vec{R}_j} \frac{\partial V_{\vec{R}}(\vec{r})}{\partial \vec{R}_i} d\vec{r} + \int \rho_{\vec{R}}(\vec{r}) \frac{\partial^2 V_{\vec{R}}(\vec{r})}{\partial \vec{R}_i \partial \vec{R}_j} d\vec{r} + \frac{\partial^2 E_{ion}(\vec{R})}{\partial \vec{R}_i \partial \vec{R}_j}, \quad (2.50)$$

relating the second derivatives of the total energy  $E(\vec{R})$  to the ground-state electron density  $\rho_{\vec{R}}(\vec{r})$  and to the linear response of the charge density to a displacement of the ions,  $\partial \rho(\vec{r})/\partial \vec{R}_i$ . The  $V_{\vec{R}}(\vec{r})$  stands for the electron-ion interaction and  $E_{ion}(\vec{R})$  is the direct ion-ion interaction. Within DFPT, the charge-density and wave-function linear response to a perturbation of a wave-vector  $\vec{q}$  is given by a closed set of equations which can be solved in terms of lattice-periodic functions and is decoupled from similar equation for other Fourier components of the same perturbation. Only sums over occupied orbitals are involved [36].

In a *dipole approximation*, the **intensity** of the infrared active modes may be calculated [38] in terms of the oscillator strengths [39] determined by the Born effective charges and the displacement vectors:

$$I(\omega) = \sum_{\alpha=1}^3 \left| \sum_{l=1}^M \sum_{\beta=1}^3 Z_{\alpha\beta}^*(l) e_{\beta}(l) \right|^2, \quad (2.51)$$

where  $e_\beta(l)$  is the normalized vibrational eigenvector of the  $\omega$ -th mode,  $\alpha$  and  $\beta$  indicate the Cartesian polarizations,  $l$  labels the different atoms of the system, and  $Z_{\alpha\beta}^*(l)$  is the Born effective charge tensor of the  $l$ -th atom.

The ionic effective charges  $Z_{\alpha\beta}^*(l)$  are - from the computational point of view - essentially the second derivatives of the energy of the molecule with respect to an applied electric field and to the amplitude of a vibrational distortion. As such, they are directly accessible to second-order density-functional perturbation theory (DFPT) [40, 41], which looks to be a very powerful and accurate method to compute the vibrational properties of extended systems [42].

The Born effective charge [34] (also called transverse or dynamic charge) of a crystalline system, defined as the induced polarization due to a unit sublattice displacement, is a fundamental quantity connecting the electrostatic fields of the lattice to its phononic properties [43]. It contains important information not only about the electronic structure and the bonding properties of the system, but also about the coupling of its longitudinal- and transverse-optical phonon modes to the external infrared radiation. The  $Z_{\alpha\beta}^*(l)$  is to be understood as a coefficient of proportionality between a change of macroscopic polarization in direction  $\alpha$  caused by an atomic displacement in direction  $\beta$  under conditions of zero external field.

Furthermore, the intensity of each normal mode as a result of (2.51) is a scalar number and it is directly comparable with experimental absorption intensities.

## 2.11 Calculation of Reaction Barriers

Any chemical reaction, e.g. a dissociation, has an **energy barrier** (or in chemists' words: activation energy), which is needed to be overcome so that the reaction may proceed. If one knows both the initial and final state of the reaction (reactants and products), there are still doubts how the reaction intermediates, mainly the transition state, looks like. The **transition state** is exactly the arrangement of atoms where "old" bonds are breaking and "new" bonds are simultaneously forming, and it corresponds to a maximum of an energy profile of the reaction.

The transition state (highest-energy reaction intermediate) of each elementary reaction step is to be calculated separately from the relaxations of the low-energy structures - the reactants and products. Up to date, there are several methodologies for calculating the transition states in periodic-DFT codes: e.g. the often used and appreciated **nudged-elastic band (NEB) method** [44, 45], or the alternative **improved dimer method** [46]. The latter method has been used in this work.



### 2.11.1 Improved Dimer Method

The improved dimer method by Heyden et al. [46] is based on the original dimer method by Henkelman and Jónsson [47], which is a local saddle-point search algorithm that uses only first derivatives of the potential energy and is, therefore, especially appropriate for large systems. The dimer method uses two points in  $3n$ -dimensional space (a *dimer*), which are slightly displaced by a fixed distance of  $2\Delta R$  (see Fig. 2.5). The term  $n$  represents the number of atoms. The locations

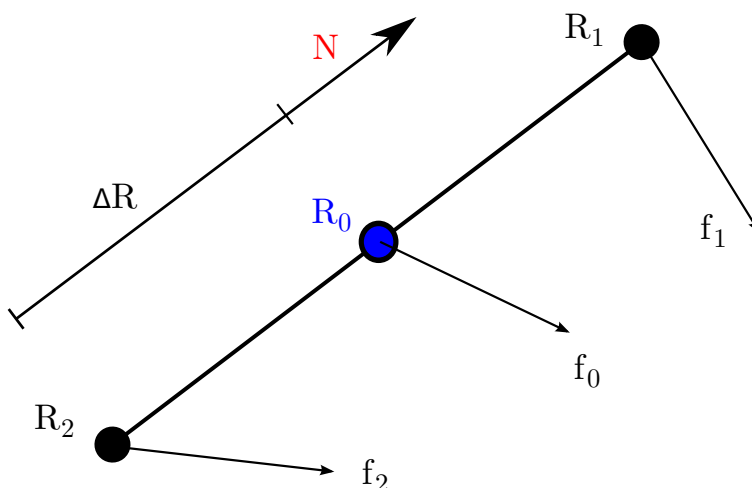


Figure 2.5: *Definition of the various points in  $3n$ -dimensional space used by the improved dimer method (after Ref. [46]).*

of the dimer end points  $\mathbf{R}_1$  and  $\mathbf{R}_2$  are defined by:

$$\mathbf{R}_1 = \mathbf{R}_0 + \Delta R \mathbf{N} \quad \text{and} \quad \mathbf{R}_2 = \mathbf{R}_0 - \Delta R \mathbf{N}, \quad (2.52)$$

where  $\mathbf{N}$  is a unit vector along the dimer axis and  $\mathbf{R}_0$  is the dimer midpoint.

The saddle-point search algorithm involves two steps:

1. *Rotation.* The dimer axis is rotated into the lowest curvature mode of the potential energy (PES) at the midpoint of the dimer  $\mathbf{R}_0$ .
2. *Translation.* The dimer is translated for a certain step length on the potential energy surface thereby moving towards a saddle point.

In significant contrast to quasi-Newton-Raphson algorithms, where the Hessian  $\mathbf{H}$  is updated, the curvature of the PES  $C_x$  is calculated numerically only along one

direction (which is the dimer axis) and therefore is more accurate than a curvature calculated with an updated Hessian:

$$C_N = \mathbf{N}^T \mathbf{H} \mathbf{N} \approx \frac{(\mathbf{f}_2 - \mathbf{f}_1)^T \cdot \mathbf{N}}{2\Delta R} \approx \frac{E_1 + E_2 - 2E_0}{\Delta R^2}. \quad (2.53)$$

Here  $\mathbf{f}_1$  and  $\mathbf{f}_2$  are the forces acting on configurations 1 and 2 and  $E_i$  ( $i = 0, 1, 2$ ) is the energy at the corresponding configuration. It is obvious from (2.53) that during a rotation of the dimer axis (the first step of the algorithm), the minimum of the curvature in the rotation plane is equivalent to the minimum of the dimer energy,  $E = E_1 + E_2$ .

In fact, the improved dimer method does not need both endpoint configurations  $\mathbf{R}_1$  and  $\mathbf{R}_2$ , only 1 configuration is calculated and the another point is set up as a mirror image. The direction  $\mathbf{N}$  should always correspond to a an only vibration eigenvector which has an imaginary frequency, i.e. specifying a saddle point of the PES that is the transition state.

Once the minimum curvature is found, the dimer is translated (second step the algorithm) in a direction orthogonal to  $\mathbf{N}$  by a calculated stepsize left or right, depending on whether the curvature  $C_N$  is convex or concave.

After the energy for an updated configuration  $\mathbf{R}_0$  lies under the give convergence criterion, the algorithm stops. The resulting transition state should be checked by a calculation of the full Hessian matrix and observing that there is only one imaginary mode corresponding to the proposed reaction pathway.

In this procedure, one has designed a transition state structure unless knowing the initial and the final state of a reaction (or phase transition etc.). In order to find the initial and the final structure, one needs to estimate them by shifting the atoms of transition structure by the dimer direction forwards and backwards. Using classical static relaxation procedures mentioned in Section 2.10.1, these guesses simply need to be optimized to the appropriate start- and end-configurations of the reaction, which in fact corresponds to jumping from the saddle point to minima.

# Chapter 3

## Adsorption on Solid Surfaces

In this chapter, experimental and theoretical knowledge base of the phenomenon called adsorption will be summarized.

It will be explained what proceeds with a gas molecule when it meets a solid surface, how to measure this process experimentally, how to simulate the force holding the molecule and how to forecast the behavior of this reactive system.

### 3.1 Adsorption by Experiment

The importance of surface reactions has raised in the course of development. Thus approx. 90 % of all chemical products are nowadays being produced by means of catalytic reactions [48], whereas the chemical process itself takes place on the catalyst surface.

Therefore it is necessary to stick an atom or a molecule from the gas phase onto the surface of a solid (or a liquid). This process is called **adsorption** as whole (see Fig. 3.1). The free particle (*adsorptive*) from the gas phase becomes an **adsorbate** upon sticking on the surface (**adsorbent**). The inverse process – the releasing from the surface – is called **desorption**.

Adsorption phenomena are usually divided, according to the value of the binding energy as well as reaction mechanism, into two classes:

- *physisorption* corresponding to “small” binding energies; the molecule does not undergo any significant change of the electronic structure,

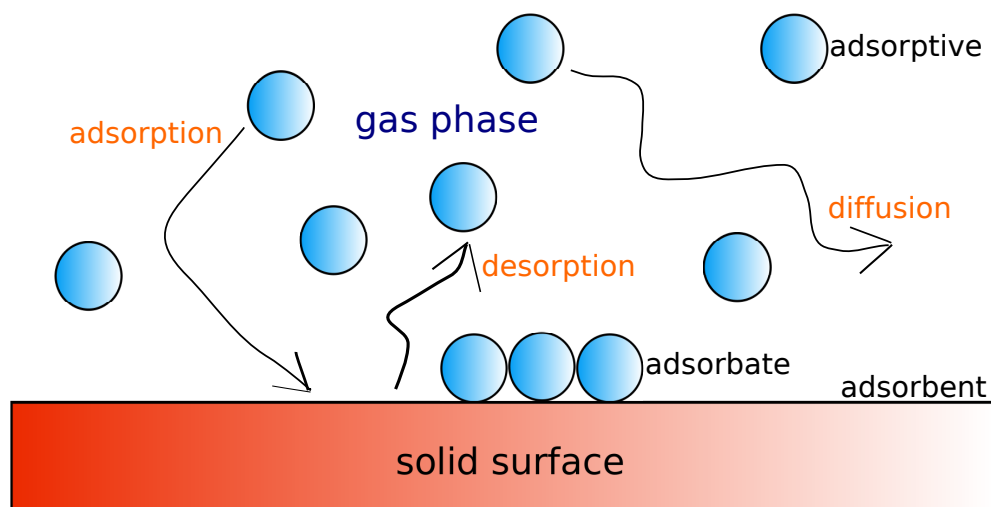


Figure 3.1: *Nomenclature of the adsorption phenomena.*

- *chemisorption* corresponding to “large” binding energies (or “adsorption” energies); the adsorption process provides a significant perturbation of the electronic structure.

For the first case (**physisorption**), the substrate-adsorbate interactions are mainly to be described by Van der Waals forces and involve almost no mixing between the orbitals of the adsorbate and the substrate.

For **chemisorption** systems, there may be a further classification of the binding into covalent, metallic and ionic bonds. This is based on survey of electronic, electrical, vibrational and thermal properties.

The theory of adsorption may be approached from three complementary points of view [49]:

- the *macroscopic or thermodynamical approach*, used to derive relations between the thermodynamical properties of the system at equilibrium;
- the *microscopic approach*, in which the principles of quantum mechanics are used to calculate vast of physical descriptors of the substrate-adsorbate interactions;
- and the *statistical mechanics* methods, which establish the connection between macroscopic and microscopic quantities and relate the two previous approaches.

Aside from the development of experimental methods for surface analysis and reaction control, there is a steady interest in theoretical description methods. These should open a better view of the processes employed within various catalytic reactions [50]. However, since the surface is an infinitely large system, which exhibits additional effects compared to a single molecule, it is necessary to employ additional approximations in the theoretical description. The character as well as the field, in which the approximations are applied, limit the usability of individual theoretical model. The models will be discussed more comprehensively in Chapter 3.2.

For the adsorption of monomolecular layers, we may define the observable **surface coverage**  $\Theta$  defined as follows:

$$\Theta = \frac{N}{N_m}, \quad (3.1)$$

where  $N$  is the number of actually adsorbed molecules and  $N_m$  is the number of molecules at full coverage.

The surface coverage  $\Theta$  in a gas-surface (i.e. adsorptive-substrate) system depends on the fractional pressure  $p$  of the gas and the temperature  $T$ :  $\Theta = f(p, T)$ .

There is a straightforward observable that shows the strength of the adsorbent–adsorbate interaction: the **adsorption enthalpy**. Since adsorption constants are equilibrium constants, they obey van’t Hoff’s equation, that relates to the adsorption enthalpy:

$$\left( \frac{\partial \ln K}{\partial \frac{1}{T}} \right)_\theta = -\frac{\Delta H}{R}, \quad (3.2)$$

where  $K$  is adsorption constant,  $T$  is the temperature,  $\Delta H$  is the adsorption enthalpy,  $R = 8.314 \text{ J mol}^{-1} \text{ K}^{-1}$  is the universal gas constant. The values of adsorption enthalpy and the surface coverage are routinely yielded by experimental techniques such as TPD (temperature-programmed desorption) or TPR (temperature-programmed reduction).

The group of spectroscopy techniques, that are usually used in order to investigate the structure and bonding of adsorbates experimentally, include [50]:

1. **Electron scattering methods.**

Here is in many ways the “benchmark” method since 1970’s the LEED (low energy electron diffraction), which probes in a *long-range* way even several atomic layers of the near-surface region and gives complete adsorbate geometry. Two rather different techniques that exploit the same underlying

phenomenon of coherent interference of elastically scattered low energy electrons are photoelectron diffraction (PhD) and surface extended X-ray absorption fine structure (SEXAFS). These two techniques are *element specific* and *local*.

## 2. X-Ray scattering methods.

Here the weak X-ray scattering signal is reproduced within the surface X-ray diffraction (SXRD), which provides good information on lateral distances of heavier adsorbed atoms. A quite different surface structural technique is X-ray standing wavefield (XSW) absorption, which can provide chemical-state specific structural data (chemical shifts) and the position of the adsorbate atom relative to the nearest substrate atoms.

## 3. Ion scattering.

These methods using beams of low atomic number ions such as  $H^+$ ,  $He^+$ ,  $Li^+$  and  $Ne^+$  at low energies formally exploit the well-defined crystallography of the surface but not explicitly the long-range order of an adsorbate, mainly used for atomic adsorbates.

## 4. Scanning probe microscopy and spectroscopic methods.

The most common method able to offer atomic-scale resolution is the scanning tunneling microscopy (STM), which provides a real-space mapping of surface atoms with sub-atomic resolution, whereas it is a probe of the spatial variations of the surface *electronic* structure, not of the relative locations of the atomic centres on the surface so the spectrum is a contour of constant partial electronic density of states outside the surface.

Among the spectroscopic methods, most obvious are the vibrational spectroscopies, infra-red reflection absorption (RAIRS) and electron energy loss (HREELS), where the behavior of molecular adsorbates on surfaces may be studied by means of vibrational excitations.

Core level photoemission (X-ray photoelectron spectroscopy – XPS), may also show “chemical shifts” in the photoelectron binding energy of adsorbates which depend on the coordination to the substrate.

## 3.2 Adsorption by *Ab-Initio* Modeling

In nature, crystals are not infinite but finite macroscopic three-dimensional (3-D) objects terminated by surfaces [51]. Many phenomena and processes (such as adsorption) occur at the interface between a condensed phase and the environment. Modeling surfaces is then of great theoretical and practical interest. A surface can

be created by cutting a crystal, which we simulate as an infinite object, through a crystalline plane. Two semi-infinite crystals are then generated containing an infinite number of atoms in the direction orthogonal to the surface, where periodicity, which is essential for applying the Bloch theorem, is lost. Further approximations to treat this problem are needed, for which alternative methods have been proposed such as those based on clusters, embedded clusters, or slabs. The focus will be given here on the slab model.

### 3.2.1 The Slab Model

The slab model consists of a film formed by a few atomic layers parallel to the  $(hkl)$  crystalline plane of interest. The film, of finite thickness, is limited by two surface planes, possibly related by symmetry. For sufficiently thick slabs, this model provides a faithful description of the ideal surface. The adequacy of the model must be checked by considering convergence of geometry, energy, and electronic properties with an increasing number of atomic layers included in the slab.

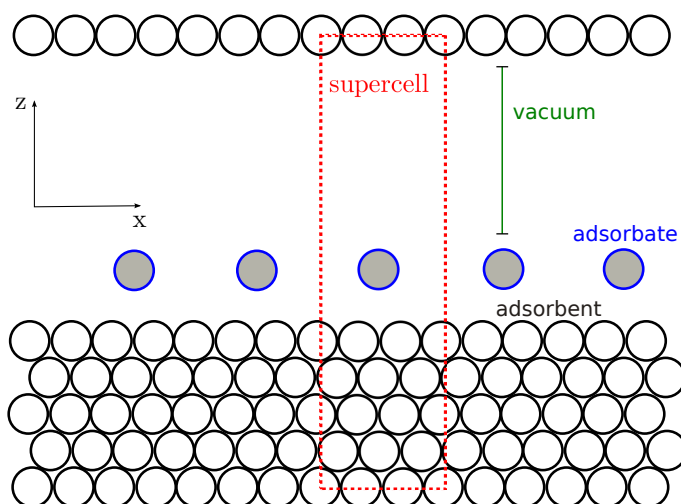


Figure 3.2: *Scheme of using the slab model. Side view of an supercell, which contains the layers of substrate atoms, the adsorptive and sufficiently large vacuum space.*

In actual calculations, one uses slabs by forcing 3-D periodicity (3-D slab model, Fig. 3.2). The three-dimensional system consists of an array of slabs of selected thickness along one direction, separated by vacuum zones. The vacuum zones must be large enough for the fictitious interactions between slabs to be negligible.

### 3.2.2 The Adsorption Energy

An appropriate model of a surface is crucial to study the adsorption of atoms or molecules [51]. Within DFT methods, the process of chemisorption can be modeled easily, whereas for physisorption – which is characteristic by weak van der Waals interactions – the correct description may sometimes be a challenge.

The *binding energy* between surface and adsorbate,  $\Delta E$ , is a key observable. It corresponds to the process in which the molecules move from an ideal gas state onto the surface, and it is defined as

$$\Delta E = E(\text{slab}/\text{ads}) - (E(\text{slab}) + N \cdot E(\text{mol})) \quad (3.3)$$

where  $E(\text{mol})$  is the energy of one isolated adsorbed molecule and  $N$  is the number of adsorbed molecules per unit cell. These energies are defined per unit cell and are negative.

$\Delta E$  can also be written as the sum of two contributions:

$$\Delta E = \Delta E_{\text{ads}} + \Delta E_L \quad (3.4)$$

The first contribution is the binding energy per unit cell per adsorbed molecule and is defined as

$$\Delta E_{\text{ads}} = E(\text{slab}/\text{ads}) - (E(\text{slab}) + E(\text{ads})) \quad (3.5)$$

where  $E(\text{slab}/\text{ads})$  is the total energy of the slab in interaction with the periodic array of adsorbed molecules,  $E(\text{slab})$  is the energy of the slab alone, and  $E(\text{ads})$  is the energy of the periodic array of adsorbed molecules without the underneath solid surface.  $\Delta E_L$  is the lateral interaction energy, per unit cell, among the adsorbate molecules, i.e., without the underneath surface, and can be either positive (repulsion) or negative (attraction), depending on the nature of the ad-molecules. In the limit of low coverage, i.e., large distances between molecules,  $\Delta E_L$  tends to zero, so that  $\Delta E_{\text{ads}} \sim \Delta E$ .

Modeling different coverages is of interest in adsorption processes and can be achieved easily by enlarging the underlying surface unit cell (i.e., within a supercell approach), so that the density of adsorbed molecules can be increased or reduced. In the limit of low coverage, lateral interactions tend to vanish and adsorbed molecules can be considered as isolated.



# Chapter 4

## Self-Assembled Monolayers

During recent decades, the phenomenon of self-assembly became more than popular [52, 53]. Exploring processes with a negligible demand of activation energy is definitely a challenging aim. The self-assembly of organic molecules on metal substrates may be used for catalysis [54, 55, 56, 57], bio-sensors [58, 59, 60], corrosion protection [61, 62], molecular recognition [63] *etc.*

### 4.1 The Phenomenon of Self-Assembly

Self-assembly, in a general sense, might be defined as the spontaneous formation of complex hierarchical structures from pre-designed building blocks, typically involving multiple energy scales and multiple degrees of freedom.

The self-assembly is also a very general principle in nature, as seen in the formation of, *e.g.*, membranes from lipid molecules, or the living cell as probably the most important paradigm. Self-assembled monolayers are ordered molecular assemblies that are formed spontaneously by the adsorption of a surfactant with a specific affinity of its headgroup to a substrate.

In 1980's, alkane thiols [ $\text{CH}_3(\text{CH}_2)_n\text{SH}$ , where  $n=0,1,2,\dots$ ] have been observed to adsorb readily on gold surfaces. Beside the fact that this was one of the new challenging proofs that gold really does easily undergo some chemical reaction, this opened the way for investigating the behavior of these organic compounds on the surface of various metals.

Adsorption of thiols on metal surfaces will be focused in the following.

A generalized view of an SAM-covered metal surface is depicted in Fig. 4.1. The head group (which is simply  $\text{CH}_3$ - for alkane thiols) is responsible for the functionalizing of the monolayer. In this way, one may synthesize a thin film (monolayer) of desired properties by means of chemical variation of the head group. There are

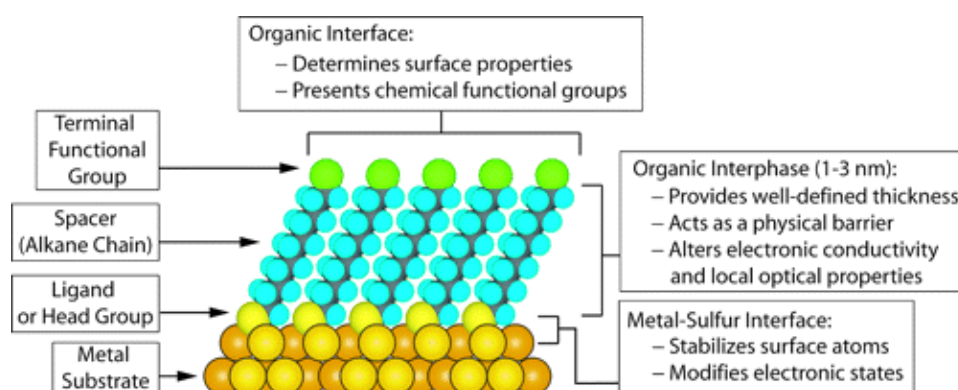


Figure 4.1: Schematic diagram of an ideal, single-crystalline SAM of alkanethiolates supported on a metal surface with (111) texture. The anatomy and characteristics of the SAM are highlighted. After Ref. [64].

several other classes of organic molecules that undergo adsorption on solid surfaces to form monolayers. The first spontaneous formation of organic monolayers was described in 1946 by Bigelow [65] for the case of alkylamines on platinum. Later, further SAMs have been observed as well: alkyltrichlorosilanes on glass [66] in 1980, dialkyldisulfides on gold in 1983, and alkanolic acids on  $\text{Al}_2\text{O}_3$  in 1985 [67].

Nowadays, the most important and the most studied SAMs are those of sulfur-head compounds (thiols, disulfides, sulfides) especially on gold (*e.g.*, Ref. [68]), but also on other metals (Ag [69, 70, 71, 72, 73, 74], Cu [69, 75], Fe [76, 77, 78], Al [79]) and semiconductors (GaAs(100) [80], InP(110) [81]). Thiols do adsorb on liquid mercury as well [82, 83]. Adsorption of thiols on Ni, Pd, and Pt will be discussed separately in detail in the following chapters.

Furthermore, also selenols  $\text{CH}_3(\text{CH}_2)_n\text{SeH}$  as Se-analogues of alkane thiols have been observed to grow on Au(111) [84, 85, 86] from solution.

An interesting discussion of the formation and stability of SAMs on engineering metals such as steel, stainless steel, aluminium, copper, and brass has been published by Van Alsten [87].

## 4.2 Kinetics and Mechanism of SAM growth

In principle, it may be stated that the monolayer is formed first by physisorption and a subsequent chemisorption. A number of studies on the **growth kinetics** of SAMs for alkanethiols on Au(111) surface have been performed, using ellipsometry, contact angle measurements [88], surface acoustic wave devices [89], second-harmonic generation [90], near-edge X-ray absorption fine structure [91], and quartz crystal microbalances [92]. The studies found that the growth rate is proportional to the number of unoccupied adsorption sites, in agreement with simple first-order Langmuir adsorption kinetics [89, 90, 91]

$$\frac{d\theta}{dt} = -k(1 - \theta) \quad (4.1)$$

where  $\theta$  is the fraction of occupied surface sites,  $t$  is time, and  $k$  is a rate constant that contains the flux of thiol molecules to the surface and the sticking coefficient.

Concerning the preferred surface **adsorption site** on gold (111) [93], the general picture of the  $(\sqrt{3} \times \sqrt{3})R30^\circ$  alkanethiolate lattice that one had until some time ago was that the S heads were placed in equivalent sites somewhere between the fcc hollow and the bridge site (Fig. 4.2). However, some years ago even on-top

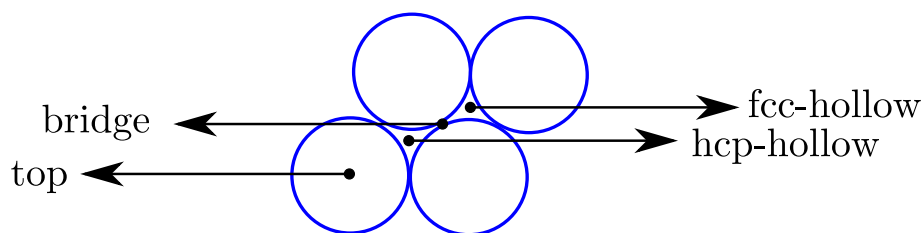


Figure 4.2: Possible adsorption sites for an alkanethiolate molecule on (111) surface: on-top, bridge (2-fold) and hollow (3-fold, hcp- and fcc-like).

adsorption has been reported [94, 95], although all DFT calculations agree that the top site adsorption has the lowest adsorption energy (i.e. it is the least favorable site).

As described by Poirier and Pylant [96] using ultrahigh-vacuum scanning tunneling microscopy (STM) for long-chain alkanethiols (with as well as without a substitution on the terminal  $-\text{CH}_3$  group), the formation of the monolayer follows a two-step process that begins with condensation of low-density crystalline islands, characterized by surface-aligned molecular axes, from a lower density lattice-gas phase.

At saturation coverage of this phase, the monolayer undergoes a phase transition to a denser phase by realignment of the molecular axes with the surface normal (Fig. 4.3). One may therefore see that molecule-substrate and molecule-molecule interactions play an important role here.

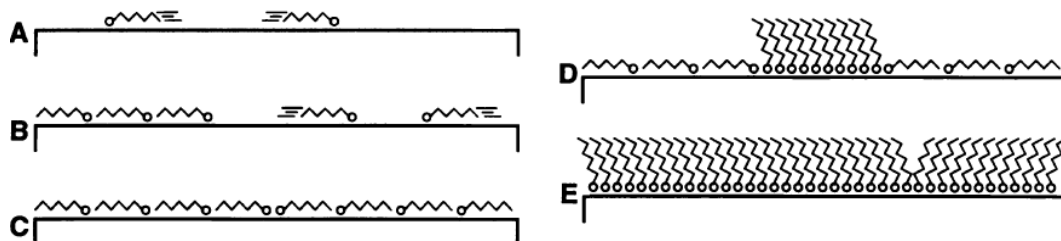


Figure 4.3: *Schematic of self-assembly mechanism for n-alkanethiols on Au(111). (A) Thiols adopt the highly mobile lattice-gas phase at very low coverage. (B) Above a critical value of surface coverage, striped-phase islands, characterized by surface-aligned molecular axes, nucleate heterogeneously and grow in equilibrium with a constant-pressure lattice gas. (C) Surface reaches saturation coverage of striped phase. (D) Surface undergoes lateral-pressure-induced solid-solid phase transition by nucleation of high-density islands at striped-phase domain boundaries. (E) High-density islands grow at the expense of the striped phase until the surface reaches saturation. After Ref. [96].*

### 4.3 Alkanethiol SAMs on Nickel

A detailed description of experimental results on the adsorption of alkanethiols on nickel helps to find the corroboration of theoretical results in the following chapters. Adsorption on nickel was quite thoroughly studied.

In 1991, Castro and White [97] studied the decomposition of methane thiol on Ni(111) using TPD, SSIMS and AES spectroscopies. The experiments show that the thermal stability of the adsorbate is very limited. At 100 K, the  $\text{CH}_3\text{SH}$  adsorption is mostly molecular. With elevating temperature, thermal decomposition occurred below 150 K, proceeding by S-H bond cleavage to form adsorbed species  $\text{H}(a)$  and  $\text{CH}_3\text{S}(a)$ . For low thiol coverages (i.e. those lower than  $1/3$ ), complete decomposition to desorbing hydrogen and residual sulfur and carbon was observed. In the case of higher coverages, one could observe a desorption of a mixture of decomposition products  $\text{CH}_4$ ,  $\text{C}_2\text{H}_6$  and  $\text{H}_2$  in the TPD spectrum. If pre-adsorbed sulfur ( $\theta = 0.25$  ML) was present on the surface, thiol desulfurization and dehydrogenation was inhibited.

Theoretical investigation of  $\text{CH}_3\text{S}$  adsorption on Ni(111) cluster (28 atoms, 3-layers) was performed using configuration-interaction (CI) methodology by Yang et al. [98]. Adsorption on both three-fold (hollow) sites and bridge sites were found to be energetically stable with adsorption energy of  $2.65 \text{ eV}$ , whereas metastable configuration on atop sites is disfavored by  $0.17 \text{ eV}$  with respect to bridge/hollow. For bridge and atop adsorption, C-S bond is strongly tilted from the surface normal. Each adsorption mode may be distinguished by slightly different C-S stretch vibrational frequency.

Fisher et al. [99] studied the methane thiolate  $\text{CH}_3\text{S}$  on Ni(111) using CS-NIXSW (chemical-shift normal-incidence X-ray standing wavefield absorption). Two distinct adsorption species were found according to temperature: at lower temperatures (below 132 K), hollow and bridge sites are occupied, whereas at slightly higher temperatures, only hollow adsorption modes occur and surface reconstruction was confirmed.

Multiple-method experimental study (high resolution XPS, HREELS and TPD) by Rufael et al. [100] gave following results: low-temperature (below 150 K) methane thiolate prefers bridge adsorption sites with a tilted configuration, between 150 and 250 K a fraction of the bridge-bonded thiolate molecules is converted into hollow sites with their C-S bonds oriented nearly perpendicular to the surface. The C-S bond in the hollow-bonded thiolate is more stable and does not undergo hydrogenolysis (which leads to methane  $\text{CH}_4$ ) until 300 K. Hydrogenolysis in general proceeds within 250 – 350 K temperature range. Co-adsorbed surface hydrogen was detected to favor the formation of thiolate in the bridge site.

Mullins et al. [101] also studied experimentally the adsorption and orientation of  $\text{CH}_3\text{S}$  on Ni(111) using angle-resolved X-Ray photoelectron spectroscopy (AR-XPS). For surface coverage of  $\theta = 0.25 \text{ ML}$  (monolayer) with 0.1 ML of sulfur present on the surface, one could determine an adsorbed species within the temperature range of 150 – 250 K, where the thiolate occupied 3-fold fcc-hollow sites tilted at  $35^\circ$  to the surface normal. Above the upper temperature limit, the surface was supposed to undergo reconstruction, since 4-fold adsorption sites appeared.

Dimethyl disulfide  $(\text{CH}_3\text{S})_2$  may also easily serve as a precursor of methane thiolate, as presented by Rufael et al. [102] in combined experimental study using HREELS, XPS, LEED, AES, TPD and deuterium labeling techniques. They observed that below 150 K, all S-S bonds in dimethyl disulfide are broken, forming adsorbed methane thiolate. Surface reconstruction appeared for high coverages (0.33 ML) of  $\text{CH}_3\text{S}$  and 0.10 ML of sulfur (the S is produced by  $\text{CH}_3\text{S}$  decomposition yielding hydrocarbons – methane and ethane).

## 4.4 Alkanethiol SAMs on Palladium

Concerning the adsorption on platinum, there are unfortunately no experimental results dealing with short-chain alkanethiols, which are of more interest in our particular study. However, measurements on long-chain alkanethiols are available, and they serve at least few informations about the preferred adsorption sites, vibrational spectroscopy properties and STM and LEED patterns.

A study by Love *et al.* [103] reveals that in a set of long-chain thiols ( $C_8 - C_{26}$ ) on Pd(111), the perfection of crystalline ordering increases with the chain length. The average orientation of an ensemble of all-*trans*-conformer chains with a tilt angle of  $14 - 18^\circ$  with respect to the surface normal is elucidated from the RAIR spectroscopy. The SAMs are stable in air at room temperature, although the sulfur present at the surface oxidizes in a period of few days. Based on LEED and STM studies, the most common surface structures correspond to the translational symmetries of  $(\sqrt{7} \times \sqrt{7})R19.1^\circ$  (2/7 and/or 3/7 coverage) and  $(\sqrt{3} \times \sqrt{3})R30^\circ$  (1/3) overlayers, whereas the former one probably prevails, as the thiol has a density of the chains in the monolayer of  $45.8 \text{ \AA}^2/\text{molecule}$ , which corresponds very well with the  $\sqrt{7}$  periodicity. This may, however, not exclude the existence of the  $\sqrt{3}$  periodicity for shorter alkane chains, especially for methane thiol.

Carvalho *et al.* [104] studied solely 1-eicosanethiol  $\text{CH}_3(\text{CH}_2)_{19}\text{SH}$  on Pd for its possible use in microcontact printing (commonly abbreviated as  $\mu\text{CP}$ ), i.e. the thiol served as a protecting group of nano-sized electrical conductors. The authors claim a total chemisorption of the thiol, where sulfur atoms form the interface between the metallic phase and alkyl chains. A similar study objected on the use of Pd-thiol systems in  $\mu\text{CP}$  was published by Love *et al.* [105]

## 4.5 Alkanethiol SAMs on Platinum

As for adsorption of thiols/thiolates on platinum, the early publication in 1985 by Koestner *et al.* [106] presented experimental study of  $\text{CH}_3\text{SH}$  decomposition on Pt(111) surface using HREELS and NEXAFS. It was found out that upon the first dehydrogenation step, the formed  $\text{CH}_3\text{S}$  exhibits tilted configuration on the surface, with a tilt angle of the S-C bond  $45 \pm 10^\circ$  from the surface normal. A metastable product of further dehydrogenation – thioformaldehyde – was also observed. Measured vibrational frequencies of adsorbed  $\text{CH}_3\text{S}$  species may serve for comparison with *ab-initio* results, even if the accuracy is not fully convincing.

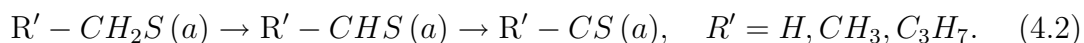
Rufael et. al studied experimentally the hydrogenolysis of adsorbed  $\text{CH}_3\text{SH}$  on Pt(111) [107] and its thermal decomposition [108] on the same surface plane. Concerning the temperature-dependent behavior, at 110 K there is no more evidence of surface thiol on previously clean Pt surface, whereas a presence of pre-adsorbed sulfur enhances the stability of S-H bonds up to 180 K.

Theoretical investigation of  $\text{CH}_3\text{S}$  adsorption on Pd(111) and Pt(111) 11-atoms clusters by Sellers [109] using Hartree-Fock and perturbation theory calculations clearly differentiated into perpendicular adsorption on platinum and strongly tilted ( $62.4^\circ$ ) configuration on palladium surface. The adsorption was postulated to happen preferentially in the hollow sites, with the adsorption energy of 3.43 eV and 2.75 eV for Pd and Pt, respectively.

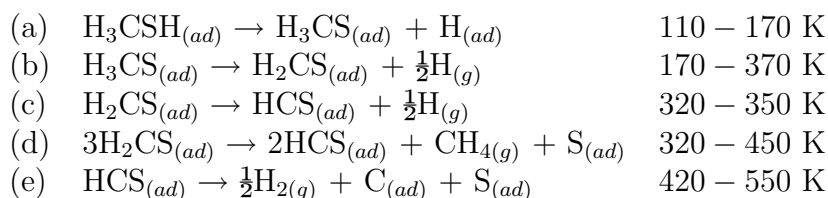
Kim et al. [110] tried to examine the adsorption site of methane thiol on Pt(111) experimentally in the temperature range 298 – 1073 K by means of time-of-flight scattering and recoiling spectrometry (TOF-SARS) and LEED. Surprisingly, at room temperature, the diffuse LEED pattern of the adsorbed  $\text{CH}_3\text{SH}$  monolayer was  $(\sqrt{3} \times \sqrt{3})R30^\circ$  and the sticking probability  $\sim 1 \times 10^{-3}$ . With elevating temperature, sequential dehydrogenation was observed.

The surface structure of methane thiol on Pt(111) was also investigated by Lee et al. [111] using NIXSW spectroscopy. At  $T \approx 223$  K, only surface-bound methane thiolate was believed to be present, occupying an offset-atop bonding site, although alternatively a model with co-occupation of atop and fcc hollow sites (with the same probability) was also stated.

An interesting study of alkyl chain length effect on thermal decomposition behavior of alkanethiols ( $\text{R-SH}$ , where  $\text{R} = \text{CH}_3, \text{C}_2\text{H}_5, \text{and } \text{C}_4\text{H}_9$ ) on Pt(111) has been published by Lin et al. [112]. This combined TPD and XPS study revealed that the density of adsorption of alkanethiol decreases with increasing length of the alkyl chain. The molecules were observed to undergo a stepwise dehydrogenation:



In more detail, the decomposition mechanism of  $\text{CH}_3\text{SH}$  on Pt(111) at saturation coverage according to TPD and XPS spectra results may be summarized as follows:



As a sample study of long-chain alkanethiol adsorption on Pt(111), the work by Li et al. [113] should be mentioned. Their experimental study involved water contact angle measurements, ellipsometry, RAIRS spectroscopy on *n*-alkanethiols  $\text{CH}_3(\text{CH}_2)_m\text{SH}$  ( $m = 5, 7, 9, 11, 13, 15, 17, 19, 21$ ). The authors observed adsorbed molecules with a hydrocarbon chain backbone tilted away from the surface normal by less than  $15^\circ$ . The longer the hydrocarbon chain, the better crystalline-like overlayer structure (clearer adsorption pattern) was found. Furthermore, XPS spectra revealed that only metal–thiolate bonding is solely formed by interaction of the thiol headgroups with the surface.



# Chapter 5

## Computational Results

### Computational Details

The first-principles calculations have been performed using a DFT approach by the means of the VASP code (*Vienna Ab-initio Simulation Package*) [114, 115, 116, 117] as available on computer clusters of the research groups of prof. J. Hafner and prof. G. Kresse (main developer of the package). VASP enables extensive parallelization in environments such as *e.g.* LAM, MPI, MVAPICH, or OpenMPI [118].

The generalized gradient approximation (GGA), with the exchange-correlation functional by Perdew and Wang (PW91) [12] was used for all structure relaxations. The electron-ion interaction was described by the projector-augmented wave (PAW) method [119]. The Kohn-Sham one electron valence eigenstates were expanded in terms of plane-wave basis sets with a cutoff energy of 400 eV (except the preliminary calculations on clean metals).

All calculations, where Ni atoms occurred, have been performed spin-polarized, so that to ensure the magnetic character of the metallic substrate.

The  $k$ -point sampling of the two-dimensional electronic Brillouin zone of the periodic supercells was performed using the Monkhorst-Pack scheme [120]. Usually, Methfessel-Paxton smearing [121] of  $\sigma = 0.2$  eV was utilized to improve convergence for systems containing metal atoms, whereas Gaussian smearing with low  $\sigma$  values were used for cells with isolated molecules. In both cases, the corrected energy for  $\sigma \rightarrow 0$  was employed in the evaluation.

## 5.1 Bulk Metals

At the beginning, calculations on the structure of the bulk metals have been performed. This included the evaluation of equilibrium lattice constants, surface energies and bulk moduli for Ni, Pd and Pt.

### 5.1.1 Preliminary Calculations

#### The Influence of the $k$ -Point Sampling

Palladium bulk calculation (where the bulk metal structure is described by a single atom in an rhombohedral unit cell) has been performed in order to check the influence of  $k$ -point sampling in the reciprocal space on the convergence of energy values. The lattice constant was kept fixed here to the experimental value of  $a_{exp} = 3.8907$  Ångström. The grids of  $1 \times 1 \times 1$  up to  $20 \times 20 \times 20$   $k$ -points were evaluated in 30 steps. The test calculation was repeated for both spin-polarized and non-spin-polarized systems, respectively (Fig. 5.1). For both systems, the total energy

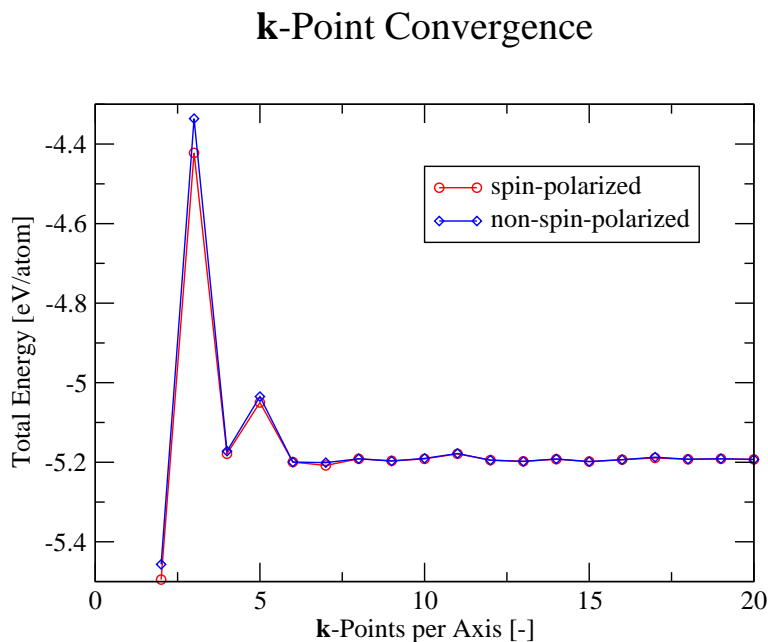


Figure 5.1: *Convergence test of the total energy with respect to  $k$ -point sampling.*

convergence curve follows the same trend. We may state, that the total energy of FCC unit cell is converged already with  $6 \times 6 \times 6$   $k$ -points for the used parameters of

the calculation (cutoff energy 270 eV, Methfessel-Paxton smearing). Use of spin-polarization does not have any significant effects on the energy, beside the fact that one does not need spin-polarized calculation (which is more demanding on computer power) for a non-magnetic element.

### The Influence of the Energy Cut-Off

The cut-off energy for plane wave basis set is an important and sensitive variable to be set. The influence of the cut-off energy on the convergence of the total energy of the rhombohedral single-atom unit cell has been evaluated, with a fixed  $k$ -point-mesh of  $20 \times 20 \times 20$   $k$ -points (which is already an apparently converged value) and Methfessel-Paxton smearing. For a demonstration of magnetism effects, the calculation has been performed for both the spin-polarized and non-spin-polarized system (Fig. 5.2). The lattice parameter was kept fixed again to the experimental value of  $a_{exp} = 3.8907 \text{ \AA}$ . In both cases, the total energy was evidently well con-

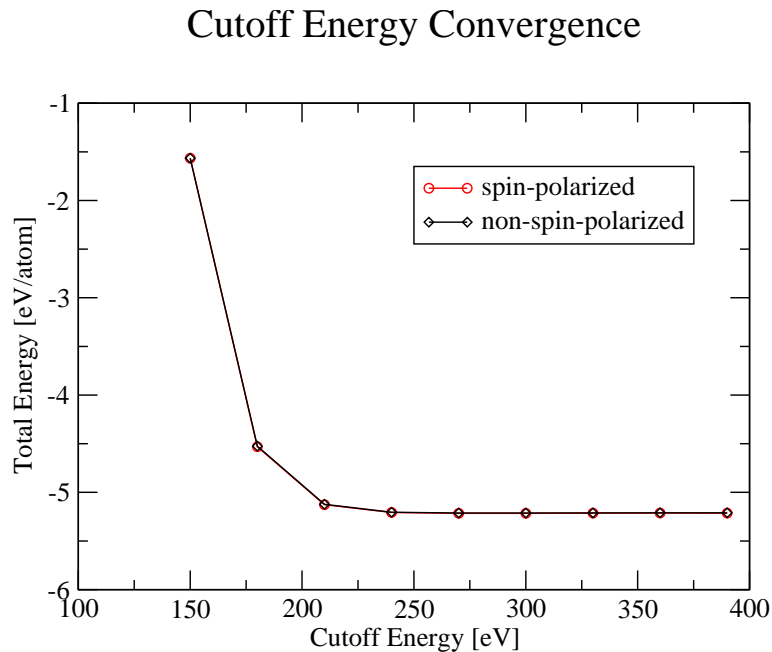


Figure 5.2: *Convergence test of the total energy with respect to energy cutoff.*

verged with kinetic energy cut-offs over 240 eV, whereas a default cut-off value for palladium in GGA\_PAW pseudopotentials in VASP package is 270 eV.

### 5.1.2 Determination of the Lattice Constants, Bulk Moduli and Cohesive Energies

#### Lattice Constants

The *lattice constant* (*lattice parameter*) is an essential parameter for the description of the metal bulk structure. The lattice constant has been determined for nickel (both magnetic and non-magnetic settings), palladium and platinum. All the metals of the nickel group crystallize in FCC (*face-centered cubic*) cells, which can be preferably described by an rhombohedral primitive cell including single metal atom set up to the origin. Therefore one evaluates the lattice constant directly as a lattice vector length. The method used was an automated scan via changing the cell volume (lengths of cell basis vectors) and evaluating the total energy after the first ionic step of the each relaxation. The  $k$ -point grid of  $20 \times 20 \times 20$   $k$ -points has been applied as used previously, with an energy cutoff of 270, 250 and 230 eV (for Ni, Pd, and Pt, respectively).

Numerical solution of the minimum search of the total energy with respect to the lattice constant (or cell volume) should in principle not be done simply by means of quadratic regression, since the energy function is not second order polynomial.

In this work, we have used the so-called Murnaghan equation of state [122]:

$$E(V) = E_0 + \frac{B_0 V}{B'_0} \left( \frac{(V_0/V)^{B'_0}}{B'_0 - 1} + 1 \right) - \frac{B_0 V_0}{B'_0 - 1}. \quad (5.1)$$

where  $B_0$  is the equilibrium value of bulk modulus for pressure  $P = 0$ ,  $B'_0$  is the isothermic derivative  $\partial B / \partial P$  and  $V_0$  is the equilibrium cell volume. The process of nonlinear regression by the means of fitting of  $E = E(V)$  function (Fig. 5.3) yields directly the optimal value of the cell volume together with bulk modulus of the solid material.

Lattice constants have been evaluated by means of the numerical fitting to the Murnaghan equation (5.1). Since the unit cell used is a cubic cell, for which the volume is  $V_0 = a_0^3$ , the lattice vector was evaluated quite simply as the cubic root of the equilibrium cell volume.

We obtained values of the lattice constants 3.52, 3.96 and 3.99 in good agreement with experiment (see comparison in Table 5.1).

Magnetism (spin-polarization) had some minor effects on the lattice constant of nickel: the spin-polarized result of  $a_0 = 3.52$  Å was in principle identical with

### Determination of the Lattice Constants

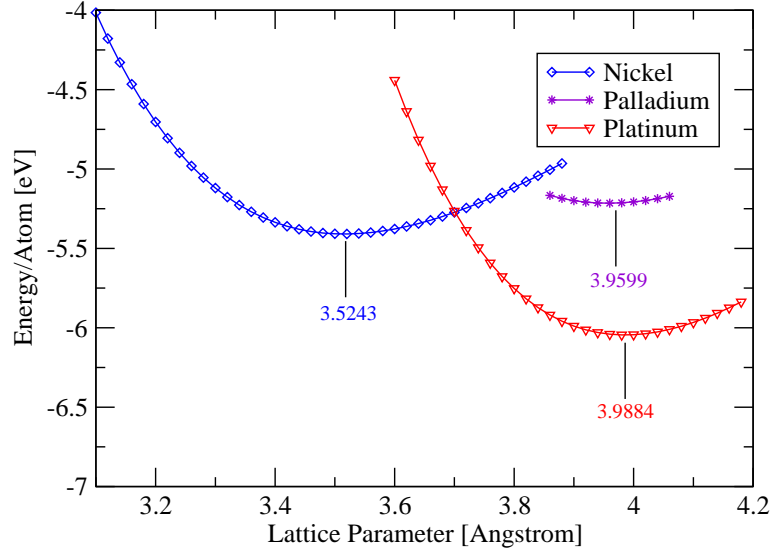


Figure 5.3: *Determination of the equilibrium lattice constants for bulk Ni, Pd, Pt.*

experimental value of 3.52 Å (both rounded down), whereas the non-spin-polarized calculation gave a slightly underestimated value of  $a_0 = 3.52$  Å (rounded up). In order to ensure the correct magnetic behavior of nickel, all consecutive calculations with nickel-containing systems have been performed with spin polarization.

### Bulk Moduli

The *bulk modulus (compression modulus)* of a substance measures the substance's resistance to uniform compression. It is defined as the pressure increase needed to cause a given relative decrease in volume. It can be formally defined by the equation:

$$B = -V \frac{\partial p}{\partial V} = -V \frac{\partial^2 E}{\partial V^2} \quad (5.2)$$

where  $p = \partial E / \partial V$  is pressure,  $V$  is volume, and  $\partial p / \partial V$  denotes the partial derivative of pressure with respect to volume. The inverse of the bulk modulus is called *compressibility*. The values of bulk moduli (Table 5.1) were calculated using the Murnaghan equation of state (Eq. 5.1) and we can confirm a good agreement with experimental results, since even larger over-/underestimations of up to 10 % are rather caused by the insufficient accuracy and thus limited reliability of experimental methods.

Table 5.1: Lattice constants  $a_0$ , bulk moduli  $B_0$  and cohesive energies  $E_{coh}$  for Ni, Pd, Pt with comparison to experimental data ('exp.'). <sup>a</sup> Ref. [123], <sup>b</sup> Ref. [124].

Metal		$a_0$ [Å]	$B_0$ [GPa]	$E_{coh}$ [eV/atom]
Ni	calc.	3.52	186.80	4.87
	exp.	3.52 <sup>a</sup>	180 <sup>a</sup>	4.44 <sup>b</sup>
Pd	calc.	3.96	162.03	3.71
	exp.	3.89 <sup>a</sup>	180 <sup>a</sup>	3.89 <sup>b</sup>
Pt	calc.	3.99	242.72	5.85
	exp.	3.92 <sup>a</sup>	230 <sup>a</sup>	5.84 <sup>b</sup>

### Cohesive Energies

The *cohesive energy* (or *atomization energy*) of a crystal is defined as the energy that must be added to the crystal to separate its components into neutral atoms at rest, at infinite separation, with the same electronic configuration [124]. In other words, the cohesive energy of a solid is the energy required to break the atoms of the solid into isolated atomic species:

$$E_{coh} = E_{solid} - \sum_A E_A^{isolated} \quad (5.3)$$

where  $A$  represents the different atoms that constitute the solid. The values of the cohesive energy calculated in this work are compared with experimental results (Table 5.1) and we confirm here a satisfying agreement. The experiments proceed by measuring the latent heat of sublimation at various low temperatures, and values are consequently extrapolated to zero Kelvin temperature.

For a calculation of separated atoms, a cubic supercell with 10 Å lattice parameter was found to be sufficiently large to express the total energy of the isolated atoms. Thus the van der Waals interaction in the atomic distance of 10 Å is already negligible – according to total energy convergence check over cell vector lengths of 2.0 to 20 Å in each direction (Fig. 5.4). The integration of the Brillouin zone was performed over  $\Gamma$ -point only using Gaussian smearing with the width of 0.1 eV.

The energy associated with the bulk solid was evaluated in an rhombohedral unit cell for the optimized lattice constant with  $20 \times 20 \times 20$   $k$ -point grid and Methfessel-Paxton smearing method of 0.2 eV width.

The calculations on both bulk and separated-atom systems have been performed with a higher accuracy concerning the cutoff energy, which was set up to 400 eV. The comparison of the unit cell sizes and shapes is given in Fig. 5.5. The lattice

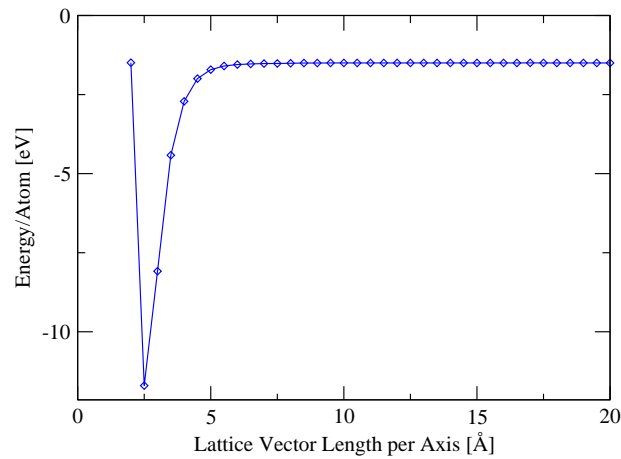


Figure 5.4: *The convergence of Pd total energy with respect to lattice vector length. The minimum at approx. 2.5 Å is the nearest-neighbor distance. For cell sizes over 5 Å, the atoms are broken from a lattice and become separated. At 10 Å distance, the interaction between atoms is already almost negligible.*

parameters are in both cases equal to nearest neighbor distance.

cubic:

$$c = 10.00 \text{ Å}$$

rhombohedral:

$$r(\text{Ni}) = 2.49 \text{ Å}$$

$$r(\text{Pd}) = 2.80 \text{ Å}$$

$$r(\text{Pt}) = 2.82 \text{ Å}$$

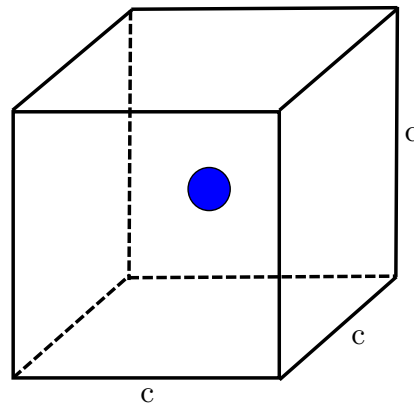
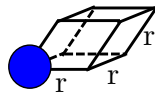


Figure 5.5: *Unit cells used for calculation of the cohesive energy: bulk system (left) and isolated atom (right-hand picture).*

## 5.2 Clean (111)-Metal Surfaces

According to experimental measurements, the project demands a simulation of well-defined (111)-metal surface planes with of  $(\sqrt{3} \times \sqrt{3})R30^\circ$  superstructure [52], as sketched in Figs. 5.6 (a) and (b). The corresponding supercell for the slab model, which later serves as an adsorbent surface, is therefore a monoclinic cell containing 3 metal atoms in each metal layer.

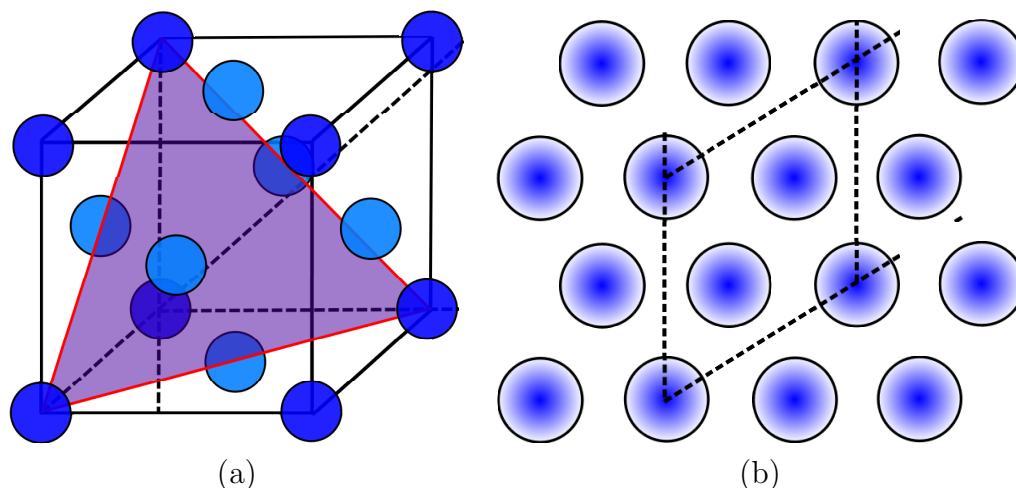


Figure 5.6: (a) Sketch of FCC (face-centered cubic) unit cell and cutting it to form the (111) crystallographic plane. (b) The definition of  $(\sqrt{3} \times \sqrt{3})R30^\circ$  superstructure over the (111) surface plane. If the nearest neighbor distance be  $d$ , then the length of each rhomb side is  $\sqrt{3}d$  and the basis vectors are rotated by  $30^\circ$  counter-clockwise from the horizontal axis.

One of the general questions in using metal slab models attended by vacuum is the number of the metal layers to be used in the calculations. Mostly only 1-2 topmost layers play the role of the surface and undergo a slight reconstruction, whereas the “deeper” layers behave rather as a bulk and stay intact.

The computational load increases steeply with the number of layers, however, an insufficient layer number leads to the fact that the model behaves like a thin layer. Five to six layers have already shown good convergence in total energies and interlayer distance contractions.

In our case, a slab consisting of 5 metal layer has been used, whereas during the geometry optimization the coordinates of the two upmost metal layers were allowed to relax while the three bottom layers were fixed to their calculated bulk positions (Fig. 5.7).



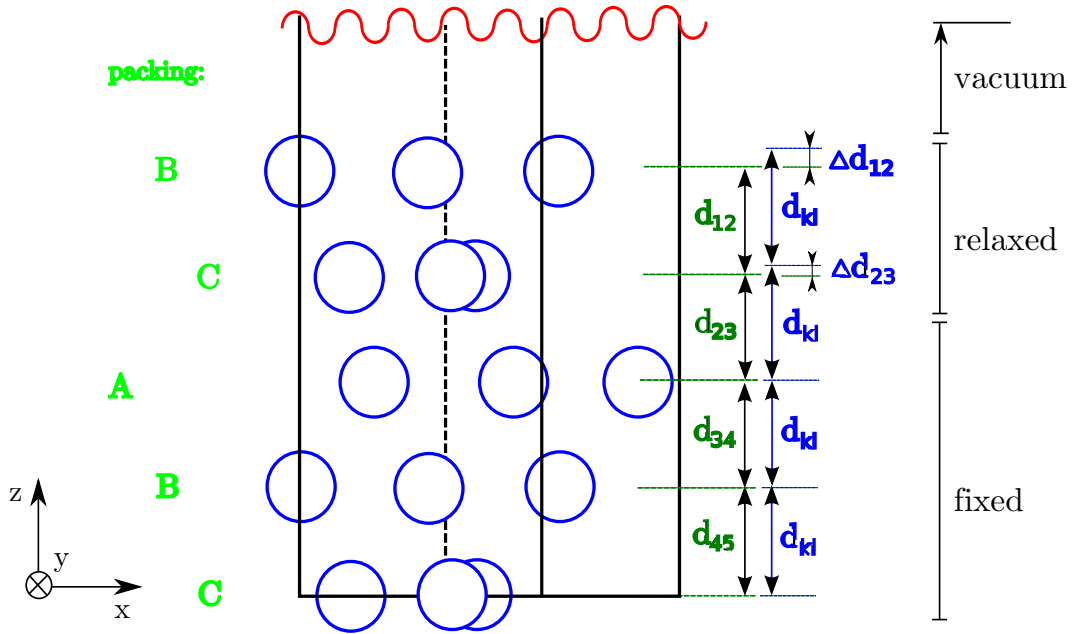


Figure 5.7: A side view of the 5-layer clean metal (111)-surface.

### 5.2.1 Surface Relaxation

When relaxing a surface with atomic positions of a truncated bulk, one observes a slight *contraction* of the upmost surface layers open to vacuum environment, it is said that a *relaxation* of a surface occurs. In cases where tremendous changes in atomic positions take place, e.g. rearrangement to another surface crystallographic plane, we refer to surface *reconstruction*, that is, the periodicity of the surface layer changes from that implied by pure bulk termination.

The relative contractions of surface layers exceed rarely 1 % for close-packed metals, however, this effect may not be neglected (unless it should be accounted as one of the terms playing role in evaluating adsorption energies later on).

The interlayer spacings were evaluated here as the mean value of the  $z$ -axis coordinate of metal atoms in the corresponding layer, and the contractions as the deviations from the ideal bulk positions (as described in Fig. 5.7). The results are summarized in Table 5.2.

A critical analysis of DFT predictions for surface relaxations, surface energies and work functions for a number of metals, including Pd and Pt has recently been presented by Singh-Miller and Marzari [126] and we find good agreement with

Table 5.2: Interlayer spacings  $d_{kl}$  (incl. their percentual deviations  $\Delta d_{kl}$ ) and surface energy  $\gamma$  with comparison to other calculations and experiment.

Metal		$d_{12}$ [Å]	$d_{23}$ [Å]	$d_{34}$ [Å]	$d_{45}$ [Å]	$\gamma$ [J/m <sup>2</sup> ]
		$\Delta d_{12}$ [%]	$\Delta d_{23}$ [%]	$\Delta d_{34}$ [%]	$\Delta d_{45}$ [%]	Ref. [125]
Ni	calc. <sup>a</sup>	2.013	2.039	2.035	2.035	1.957
	exp. <sup>c</sup>	2.008	2.033	2.033	2.033	2.380
	$\Delta$ calc. <sup>a</sup>	-0.9	+0.2	0.0	0.0	
	$\Delta$ exp. <sup>c</sup>	-1.2	0.0	0.0	0.0	
Pd	calc. <sup>a</sup>	2.294	2.280	2.286	2.286	1.336
	exp. <sup>b</sup>	2.25	2.25	2.25	2.25	1.31
	$\Delta$ calc. <sup>a</sup>	+0.1	-0.3	0.0	0.0	
	$\Delta$ exp. <sup>b</sup>	+0.25	-0.34	0.0	0.0	
	$\Delta$ exp. <sup>d</sup>	0.0±4.4	0.0	0.0	0.0	
	$\Delta$ exp. <sup>e</sup>	+1.3±1.3	-1.3±1.3	0.0	0.0	
Pt	calc. <sup>a</sup>	2.323	2.288	2.303	2.303	1.502
	exp. <sup>b</sup>	2.288	2.265	2.265	2.265	1.49
	$\Delta$ calc. <sup>a</sup>	+0.2	-0.7	0.0	0.0	
	$\Delta$ exp. <sup>b</sup>	+0.85	-0.56	—	—	
	$\Delta$ exp. <sup>f</sup>	+0.5±0.9	—	—	—	
	$\Delta$ exp. <sup>g</sup>	+1.1±4.4	—	—	—	

<sup>a</sup> This work. <sup>b</sup> Ref. [126], <sup>c</sup> Ref. [127], <sup>d</sup> Ref. [128], <sup>e</sup> Ref. [129] <sup>f</sup> Ref. [130] <sup>g</sup> Ref. [131].

their results. For Ni(111), the spin-polarized calculations are presented, and it is compatible with the earlier results of Mittendorfer et al. [132].

The comparison of the predicted surface relaxations with experiment is hampered by a wide scatter of the experimental results, but the overall trend of a modest inward-relaxation of the Ni surface, the absence of relaxation on Pd(111) and the small outward relaxation of Pt(111) are in good agreement with experiment.

## 5.2.2 Surface Energy

Surface formation energy (or shortly *surface energy*) may be computed within the slab model approach [51] as

$$E_{surf}^n = \frac{(E^n - nE_{bulk})}{2A} \quad (5.4)$$

where  $E^n$  is the energy of an  $n$ -layer slab,  $E_{bulk}$  is the energy of a single layer's

worth of bulk material, and  $A$  is the area of primitive surface unit cell. For a cell with basis vectors  $\{\vec{i}, \vec{j}, \vec{k}\}$  and vacuum space in the  $\vec{k}$ -direction, the cell area is

$$A = \vec{i} \cdot \vec{j}.$$

The factor 1/2 in Eq. (5.4) accounts for the existence of two limiting surfaces.  $E_{surf}^n$  is then the energy per unit area required to form the surface from the bulk, and it is intrinsically a positive quantity (if not, the bulk would exfoliate). As more layers would be added in the calculation by increasing the slab thickness ( $n \rightarrow \infty$ ),  $E_{surf}^n$  will converge to the surface formation energy per unit area. This important check should be performed, when studying surfaces.

In metals or small band gap semiconductors, convergence might be slower and numerical noise larger. As an alternative of Eq. (5.4), one may use the following definition for the surface energy:

$$E_{surf}^n = \frac{E^n - n(E^n - E^{n-1})}{2A}. \quad (5.5)$$

In this expression,  $E_{bulk}$  has been replaced by  $E^n - E^{n-1}$ . So the surface energy is determined from a series of calculations. If each additional layer in the slab is seen as the central one, it is clear that  $E^n - E^{n-1}$  should converge to the energy of a single layer in the bulk crystal.

If the surface formation energy of different surfaces is available, the relative stability may be evaluated. Surface stability has relevance in determining the crystal morphology, although kinetic effects can in many cases also play an important role.

In this study, we have only considered the (111) surface planes, and it may be shortly stated, that for the relevant metals, this plane has the lowest surface energy and is therefore the most stable one.

Surface energies  $\gamma$  of the surfaces of particular metals have been calculated in order to compare them with experimental results, as summarized in Table 5.2. The evaluation of  $\gamma$  has been performed for a surface model containing 5 metal layers (as sketched in Fig. 5.7), from which the 2 topmost layers on the upper side were allowed to relax.

### 5.2.3 Surface Workfunction

The *work function* of the uniform surface of a metal is defined as the difference in potential energy of an electron between the vacuum level and the Fermi level

[124]. The vacuum level is the energy of an electron at rest at a point sufficiently far outside the surface so that the electrostatic image force on the electron may be neglected (ideally as much as 100 Å from the surface and more). The Fermi level is, in principle, the electrochemical potential of the electrons in the metal.

One can also say that the workfunction  $\Phi$  of a metal is the energy needed to extract an electron at 0 K. It is usually calculated as an energy difference between the Fermi level and the vacuum potential level:

$$\Phi = E_{vac} - E_F, \quad (5.6)$$

where  $E_{vac}$  is the vacuum potential in the centre of vacuum between the slabs and  $E_F$  is the Fermi energy level of the metal.

The calculated values for the surface workfunction of the clean (111) metal surfaces are to be found in Table 5.3. The agreement of our calculated value with the experimental results (which are, in fact, very heterogeneous depending on the method used) is very good, even if the values are somehow underestimated. The percentual deviations with respect to the experiment are listed as well. Please note that the listed experimental values are measured at the temperature of 293.15 K. For the workfunctions, our calculations predict an increase in the series from Ni to Pt, in semiquantitative agreement with experiment.

Table 5.3: *Surface workfunction of clean (111) surfaces of Ni, Pd and Pt.*

Metal	$E_{vac}$ [eV]	$E_F$ [eV]	$\Phi^{calc}$ [eV]	$\Phi^{exp}$ [eV]	$\Delta\Phi$ [%]
Ni	3.38	-1.75	5.13	5.15 <sup>a</sup>	-0.47
Pd	3.67	-1.62	5.30	5.55 <sup>b</sup>	-4.50
Pt	4.92	-0.85	5.78	6.10 <sup>c</sup>	-5.25

<sup>a</sup> Ref. [133], <sup>b</sup> Ref. [134], <sup>c</sup> Ref. [135].

From computational point of view, it is important to include the dipole corrections (IDIPOL-tag in the VASP package) in the appropriate direction (here along the  $z$ -axis) in order to obtain the correct description of the constant value of the effective potential in vacuum.

The profile of the effective potential (plane-averaged) for the case of palladium is shown in Fig. 5.8. The minima in the plot correspond to the positions of palladium atom layers in the slab, whereas the flat maximum of the potential is reached in the thick vacuum layer.

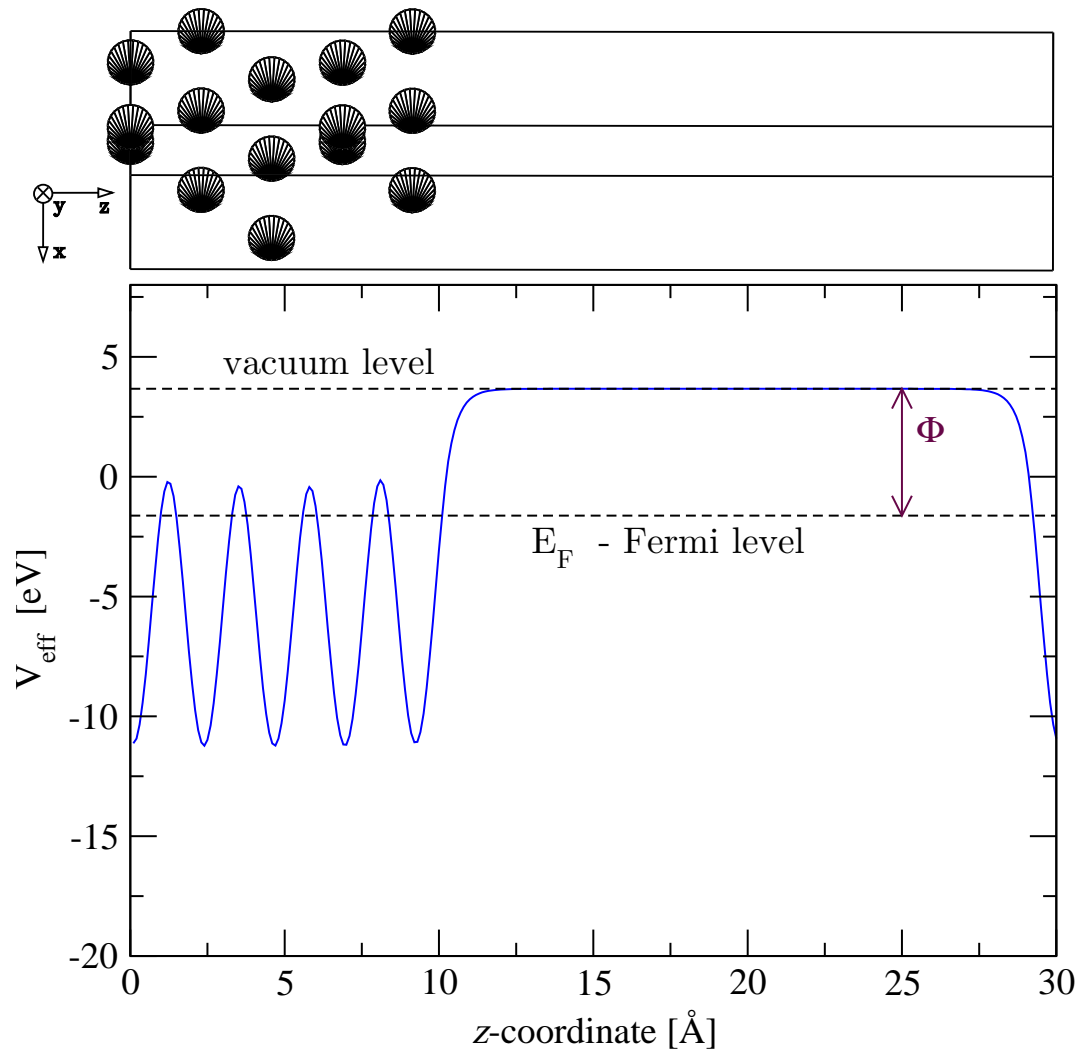


Figure 5.8: *The effective potential profile of the clean Pd(111) supercell along the z-axis and the visualization of the workfunction.*

## 5.3 Molecules and Molecule-Radicals

Structure calculations on methane thiol ( $\text{CH}_3\text{SH}$ ) and methane thiolate anion-radical ( $\text{CH}_3\text{S}$ ) have been performed in order to elucidate exactly the nature of the species in the gas state (i.e., isolated molecules). Initial structure parameters were taken from pre-optimized data of the N.I.S.T. structure database [136] and were used as an input geometry for re-optimization within the VASP Package.

Here, for the calculations of these localized systems, the integration of the Brillouin zone proceeded over  $\Gamma$ -point only. Gaussian-method smearing with the modified parameter  $\sigma = 0.01$  was used to ensure an correct description of discrete system and electron occupation levels (orbital energies), which are then given as narrow peaks in the density of states spectra.

Structure optimization and calculation of properties used RMM algorithm until forces on atoms were  $F \leq 10^{-2} \text{ eV}/\text{\AA}$ , each SCF cycle was terminated after reaching  $\Delta E \leq 10^{-6} \text{ eV}$  threshold.

In some of the chapters concerning molecular species, there have been performed several calculations using the GAUSSIAN 03 package [137]. In these calculations at DFT level of theory, the 6-31G(d) local basis set was used for Perdew-Wang 91 exchange and correlation functional (PW91PW91). Tight convergence criteria (keyword `opt=tight`, i.e.  $F \leq 7.7 \cdot 10^{-4} \text{ eV}/\text{\AA}$ ), has been applied.

### 5.3.1 Molecular Geometry

The structure relaxation of both molecular species yielded results that are in good agreement with experimental values. The geometry parameters of both species are summarized in Tables 5.4 and 5.5. There are intentionally given the results of both VASP (plane-wave basis set) and GAUSSIAN 03 (local basis set) calculation using implementations of the same exchange-correlation functional (PW91). Furthermore, a comparison with previous theoretical calculations at the MP2 level of theory ([138, 139]) is presented.

Concerning the bond lengths and angles, one can summarize that VASP results are found to be in excellent agreement with experiment (which can, however, not resolve the slight differences in the C-H bond lengths, and H-C-H and C-S-H angle resulting from the violation of  $C_{3v}$  symmetry) with a maximum error in the bond length of  $0.01 \text{ \AA}$ . Results obtained with GAUSSIAN are found to be slightly less accurate, probably due to insufficient convergence with the standard basis.

Table 5.4: *Methane thiol ( $CH_3SH$ ) structure parameters.* <sup>a</sup> Ref. [138], <sup>b</sup> Ref. [140].

Property	VASP	G03	Theor. <sup>a</sup>	Exp. <sup>b</sup>
C-S bond length [Å]	1.822	1.835	1.814	1.819
S-H bond length [Å]	1.350	1.359	1.340	1.340
C-H1 bond length [Å]	1.102	1.099	1.090	1.090
C-H2, C-H3 bond length [Å]		1.099	1.090	1.090
C-S-H bond angle [Å]	97.0	96.6	98.6	96.5
S-C-H1 bond angle [°]	106.1	106.1	106.6	107.6
S-C-H2(H3) bond angle [°]	111.5	111.6	106.6	
H1-C-H2(H3) bond angle [°]	108.7	108.6		108.5
H2-C-H3 bond angle [°]	110.3	110.2		

Table 5.5: *Methane thiolate ( $CH_3S$ ) structure parameters.* <sup>a</sup> Ref. [139], <sup>b</sup> Ref. [140].

Property	VASP	G03	Theor. <sup>a</sup>	Exp. <sup>b</sup>
C-S bond length [Å]	1.785	1.807	1.814	1.767
C-H1 bond length [Å]	1.105	1.100	1.092	1.098
C-H2, C-H3 bond length [Å]	1.098	1.065	1.089	
S-C-H1 bond angle [°]	106.4	106.7	106.9	111.5
S-C-H2(H3) bond angle [°]	112.1	112.1	112.2	
H1-C-H2(H3) bond angle [°]	107.4	107.5		
H2-C-H3 bond angle [°]	111.2	110.8		

The MP2 calculation yields perfect agreement with the experimental values, but preserve the threefold symmetry of the methyl group.

The methane-thiolate radical could have full  $C_{3v}$  point group symmetry. However, as the highest occupied molecular orbital is twofold degenerate and only partially occupied, it is unstable against a Jahn-teller distortion lowering the symmetry to  $C_s$  and the total energy per molecule by 55 meV. The fully relaxed ground state is double-degenerate, with one long and two slightly shorter C-H bonds in the methyl group, corresponding to one S-C-H angle which is slightly lower and two which are larger than average and corresponding changes in the H-C-H angles of the methyl group. The two degenerate ground states are separated by a saddle point which also has  $C_s$  symmetry, but two slightly longer (1.102 Å) and one shorter (1.096 Å) C-H bond and corresponding changes in the bond angles. The saddle point energy is only 0.5 meV above the ground state.

In this case the C-S bond length calculated using VASP is in definitely better agreement with experiment and with MP2 calculations [139] than the GAUSSIAN

result. The difference in the C-H bond lengths induced by the Jahn-Teller splitting is predicted to be largest in the GAUSSIAN calculations and distinctly lower if calculated using VASP or MP2. The predictions based on GAUSSIAN could possibly be improved by choosing a larger basis set, but this was not attempted here. The Jahn-Teller induced splitting is too small to be resolved by experiment.

We have also examined whether the use of a B3LYP hybrid functional [141, 142] instead of a conventional gradient-corrected functional influences the molecular geometries. For CH<sub>3</sub>SH the C-S bond length is increased by 0.0007 Å, while the S-H and C-H bond lengths shrink by 0.008 Å and 0.006 Å, respectively. For CH<sub>3</sub>S the C-S bond is stretched by 0.006 Å, the C-H distances are shortened by 0.008 Å. The bond angles remain unchanged.

As the hydrogen in the S-H bond may enjoy free rotation, it is preferentially situated in the way to minimize the steric interaction with the CH<sub>3</sub> group, hence the (largest) H-C-S-H dihedral angle is found approx. 180°.

The optimized molecular structure of both molecules is depicted in Fig. 5.9.

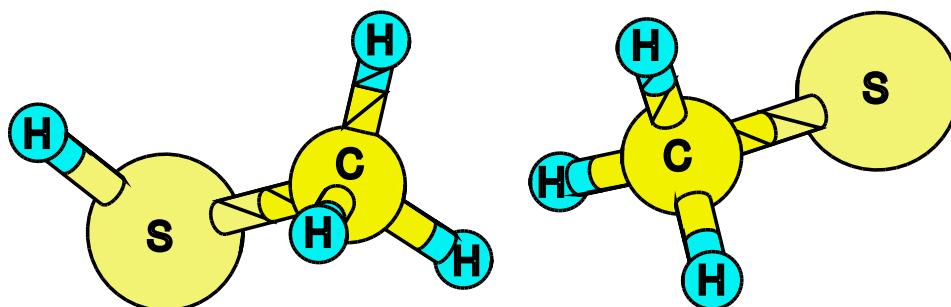


Figure 5.9: A ball-and-stick sketch of CH<sub>3</sub>SH and CH<sub>3</sub>S equilibrium structure.

### 5.3.2 Electronic Properties

Eigenvalue spectra for CH<sub>3</sub>SH and CH<sub>3</sub>S species in gas-phase single molecules are represented by the bar plots of the total density of states (DOS, see Fig. 5.10). One obtains 10 ground state energy eigenvalues for CH<sub>3</sub>S, whereas there are 12 eigenvalues for CH<sub>3</sub>SH. The term “band” in the following text is meant to be a band in the DOS spectrum appearing at a discrete energy level, i.e., it is not explicitly related to the electronic bandstructure. Since the bands are well separated, the word orbital will also be used as a synonym.

The spatial arrangement of electrons may be depicted as the charge density plot



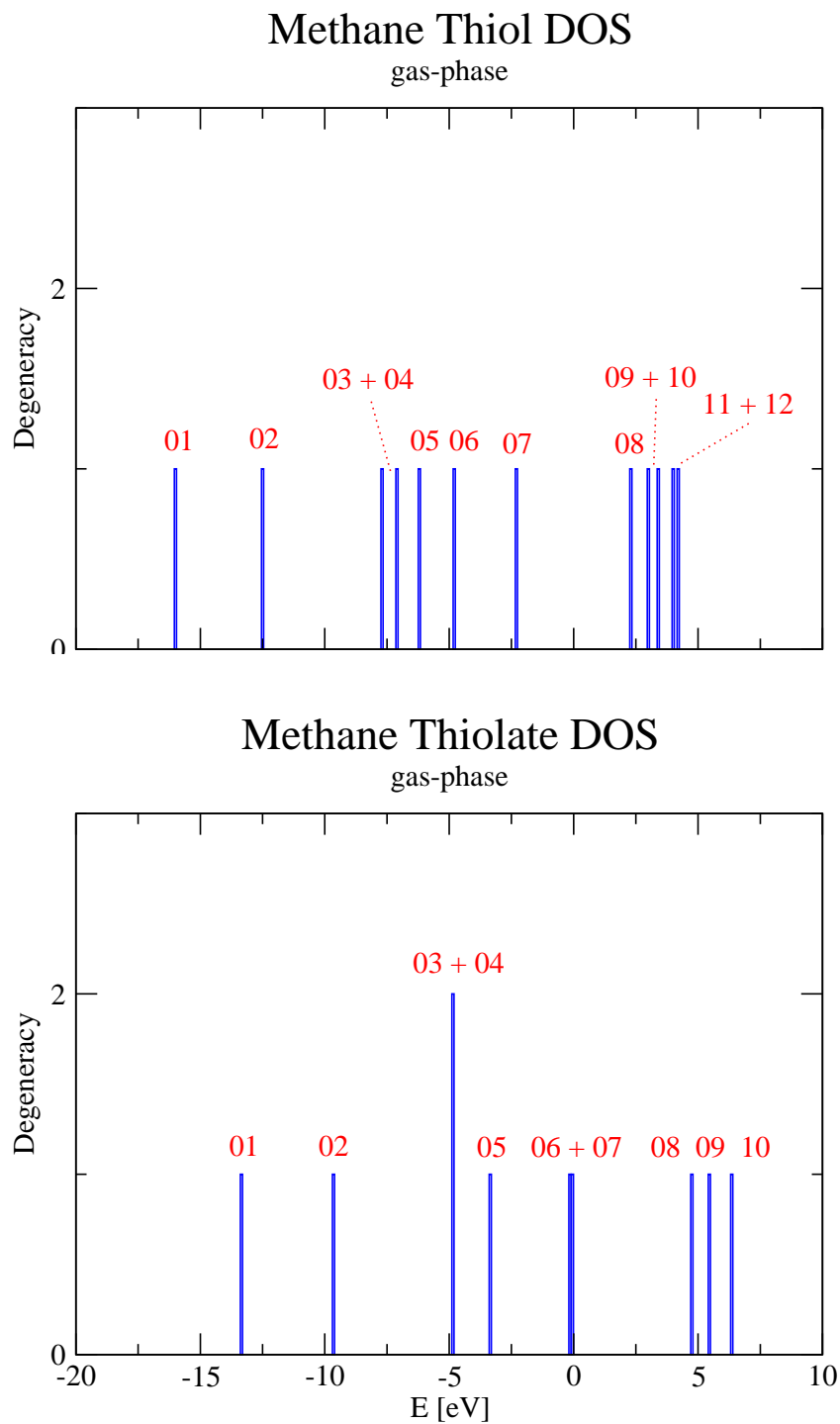


Figure 5.10: Total density of states (DOS) spectra for  $\text{CH}_3\text{SH}$  and  $\text{CH}_3\text{S}$ .

for the commensurate energy band. For a localized systems in a sufficiently large unit cell, as  $\text{CH}_3\text{HS}$  molecule or  $\text{CH}_3\text{S}$  radical in  $10 \text{ \AA}$  cubic box, this arrangement corresponds to the shape of molecular orbitals, since each band in the DOS describes an orbital at a discrete energy level. The plots of **charge densities** follow in Figs. 5.11 and 5.12. These plots may help to distinguish the nature of the particular bands (orbitals), as described further. Although the description may sometimes be a bit questionable, the  $\text{CH}_3\text{SH}$  and  $\text{CH}_3\text{S}$  systems are still easy to be “read” in terms of hybridization of atomic orbitals.

In the case of **methane thiol**  $\text{CH}_3\text{SH}$ , the system consists of altogether 26 electrons (in the vicinity of 6 atomic nuclei). Since the VASP package uses pseudopotentials, the inner electrons (core electrons) remain treated by the pseudo wavefunction and they are not explicitly distinguished in our eigenvalue spectrum. Only the valence electrons are responsible for the chemical bonding, and we have 14 of them (1 on each hydrogen atom, 4 on carbon, 6 on sulfur). According to the Pauli principle, the electrons are then to be seen as 7 electron pairs. The first 7 bands in the eigenvalue spectrum are doubly occupied orbitals, the bands 08-12 are unoccupied.

The lowest energy band 01 of  $\text{CH}_3\text{SH}$  in Fig. 5.11 in principle corresponds to the overlap of the  $s$  orbitals of carbon and of sulfur with spherical symmetry,  $\sigma : s(C) - s(S)$ , forming the strong C-S bond (the  $\sigma$  sign stands for the chemical single bond with highest electron density on the connection line between the bonding atoms). The band 02 contains (in opposite to 01) no overlap between C and S, but rather describes the S-H bond  $\sigma : s(S) - s(H)$  and at the same time, the hybridization on the  $\text{CH}_3$  moiety,  $\sigma : s(C) - s(H)$ .

Bands 03 and 04 lie quite near to each other on the energy scale (the energy difference is 0.59 eV). The band 03 depicts the overlap of the  $p_z$  orbital of carbon with the neighboring hydrogen atoms,  $p_z(C) - s(H)$ , together with mixing with  $p_z$  state of sulfur,  $p_z(C) - p_z(S)$ . Band 04 is essentially the  $p_y$  orbital of carbon, in slight interaction with 2 symmetrically closest hydrogen atoms,  $p_y(C) - s(H)$ .

The band 05 represents in principle the interaction of  $p_x$  orbital of carbon with  $p_x$  orbital of sulfur,  $p_x(C) - p_x(S)$ , whereas the interaction of the carbon  $p_x$  orbital and of the sulfur  $p_x$  orbital with adjacent hydrogen atoms is also apparent from the picture. The band 06 is to be understood essentially as the interaction of the carbon  $p_x$  orbital with the sulfur  $p_z$  orbital.

Bands 07 and 08 form the pair of the so called HOMO and LUMO orbitals (Highest-Occupied and Lowest-Unoccupied Molecular Orbitals). The band 07 (the HOMO) is the lone pair of sulfur – the  $p_y(S)$  non-bonding state. It is clear, that

this orbital plays an important role in chemical reactivity (incl. adsorption) of methane thiol. The band 08 (the LUMO) is through an anti-bonding state consisting of  $p_x(C) - p_x(S)$  mixed with  $p_z(S) - s(H)$  interaction. The HOMO-LUMO gap is found to be 4.52 eV. The gap width is 0.93 eV lower than the value of 5.45 eV estimated from ultraviolet photoemission [143].

Band 09 represents an anti-bonding state in which  $\sigma : p_x(C) - p_x(S)$  interaction clearly predominates. For band 10, we may conclude that it is an anti-bonding interaction of the sulfur  $p_z$  orbital with the adjacent hydrogen  $s$  orbital,  $p_z(S) - s(H)$ . Band 11 is a high-energy anti-bonding state, formed perhaps by interaction of the  $p_z$  orbital of carbon with  $s$  orbital of sulfur,  $p_z(C) - s(S)$ . Band 12 seems to be an electronic state formed by anti-bonding  $s(S) - s(H)$  overlap.

In the case of **methane thiolate**  $\text{CH}_3\text{S}$ , the system consists of altogether 25 electrons, 13 of which are valence electrons (1 on each hydrogen atom, 4 on carbon, 6 on sulfur). Thus there are 6 electronic pairs and 1 unpaired electron. Therefore, the first 6 bands in the eigenvalue spectrum are doubly occupied (bonding) orbitals, the band 07 is single-occupied (bonding and “very reactive”) and the bands 08-10 are unoccupied.

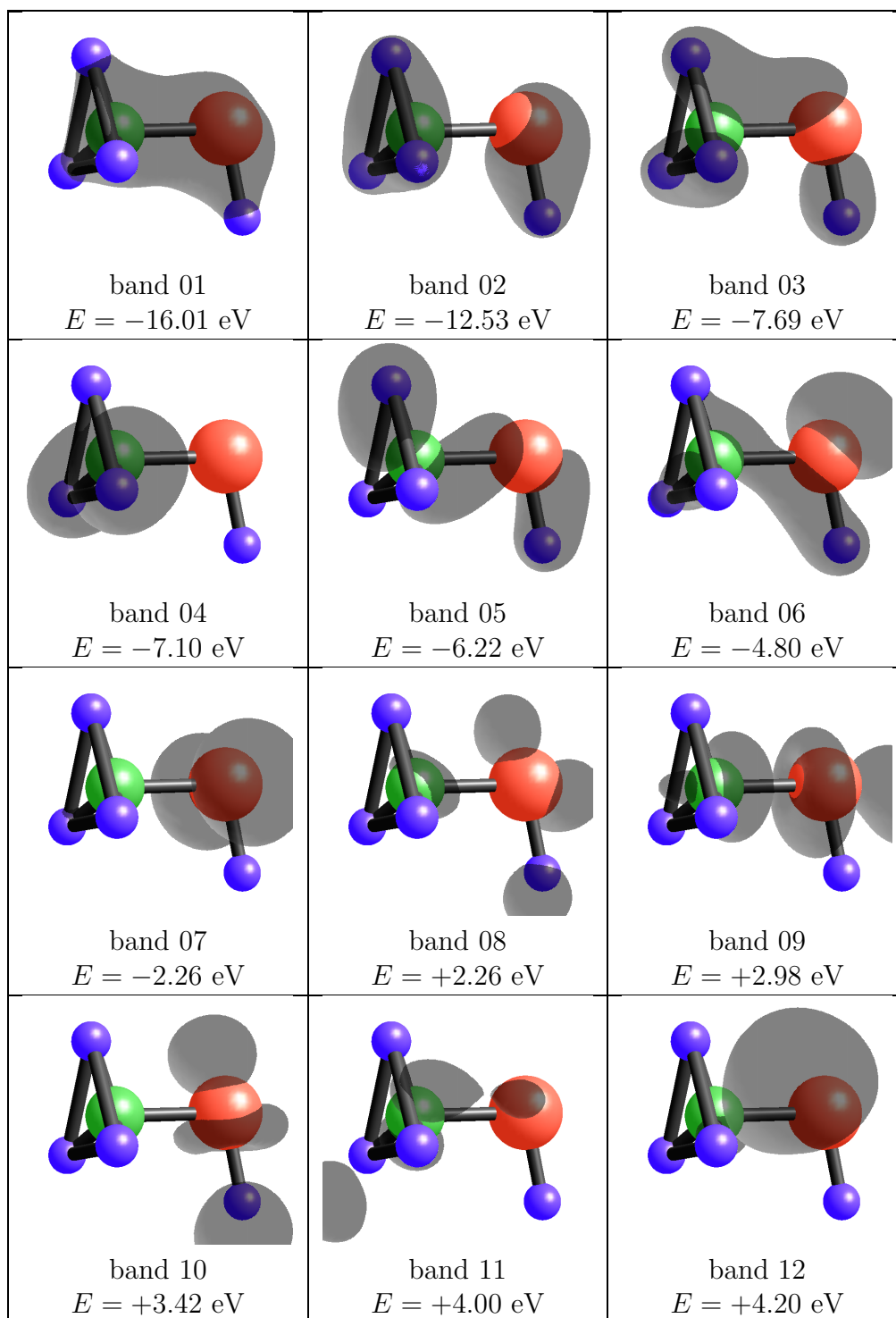
The detailed description of the electronic states of  $\text{CH}_3\text{S}$  will be to some extent very similar to that of  $\text{CH}_3\text{SH}$ . As for the band 01, which is similarly a bonding  $\sigma : s(C) - s(S)$  interaction. Band 02 is, on the contrary, the anti-bonding state  $\sigma^* : s(C) - s(S)$ , whereas the  $s(C)$  is in fact given by the hybridization on  $\text{CH}_3$ .

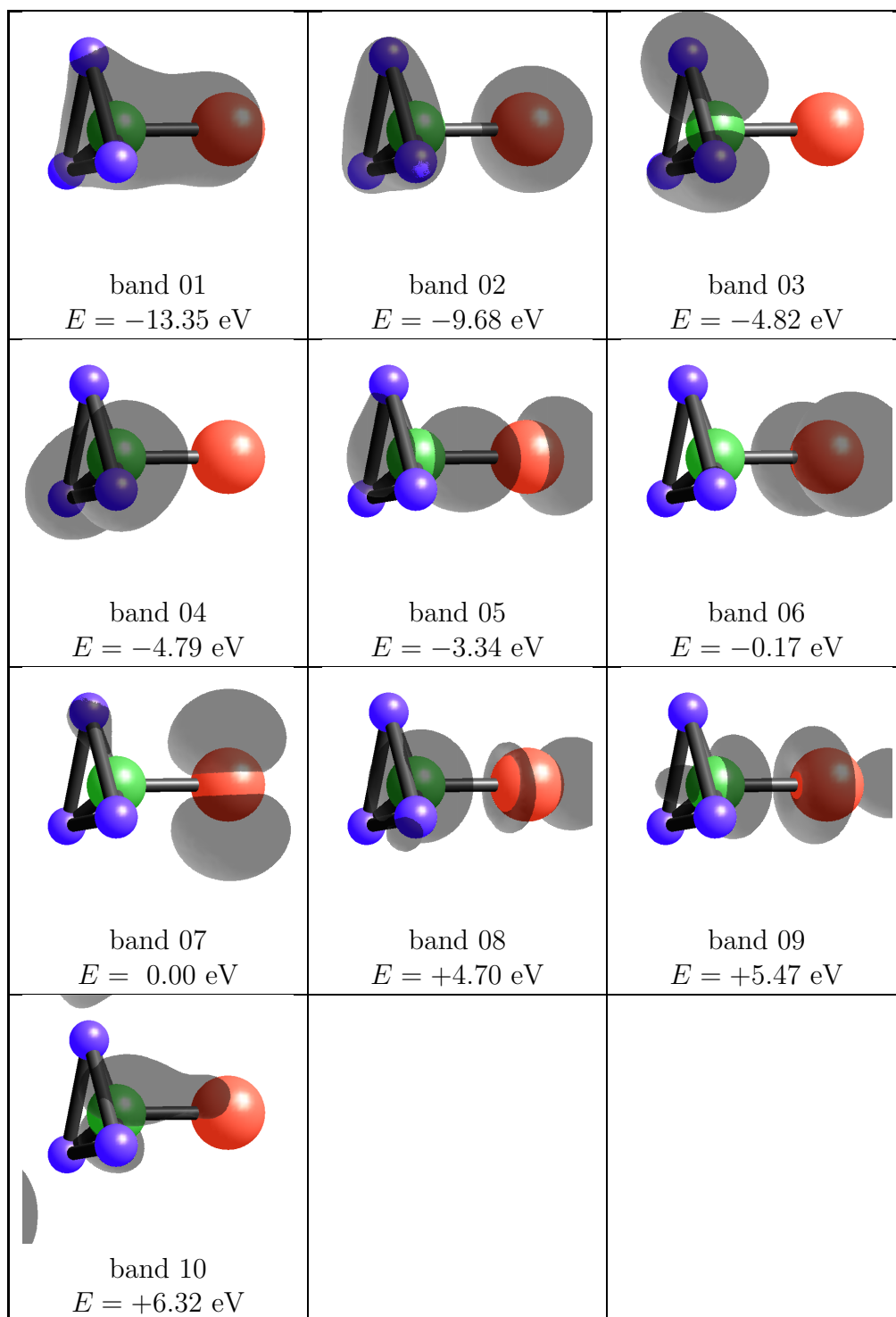
Furthermore, the bands 03 and 04 are degenerated, with an energy difference of just 0.03 eV. Band 03 represents the overlap of carbon  $p_z$  orbital with the adjacent hydrogens,  $p_z(C) - s(H)$ , whereas in band 04 the  $s(H)$  orbitals overlap with  $p_y(C)$ .

Band 05 is a textbook example of an  $\sigma : p_x - p_x$  bonding overlap between carbon and sulfur  $\sigma : p_x(C) - p_x(S)$ . Band 06 is the highest doubly occupied one, its shape concludes that it is almost unaltered sulfur  $p_y(S)$  orbital, i.e. the S lone pair.

Band 07 bears only one unpaired electron, and it is our HOMO, with a shape of sulfur  $p_z(S)$  orbital. It is the key to the chemical reactivity of the  $\text{CH}_3\text{S}$  molecule radical. The energy of this band is intentionally set up to be the zero-level (i.e. the Fermi energy,  $E_F$ ) as it is apparent from Fig. 5.10. The HOMO is split by 0.17 eV if the symmetry is lowered by Jahn-Teller distortion.

Band 08 is an anti-bonding state, which corresponds to an  $s(C) - p_x(S)$  interaction. Band 09 is an anti-bonding overlap of  $p_x(C) - p_x(S)$  orbital. Finally, band 10 is probably an  $p_z(C) - s(S)$  orbital anti-bonding interaction.

Figure 5.11: *Partial charge density plots of CH<sub>3</sub>SH.*

Figure 5.12: *Partial charge density plots of CH<sub>3</sub>S.*

### 5.3.3 Vibrational Analysis

The vibrational analysis of CH<sub>3</sub>SH molecule and CH<sub>3</sub>S radical has been performed both using the VASP and GAUSSIAN code. The calculations of the dynamic matrix for a ground state of the molecules and its evaluation gives wavenumbers of the vibrational normal modes for the treated structure.

The tabular description of the molecular vibrations, calculated by several methodologies (*vide infra*), is to be found in Tab. 5.6 and Tab. 5.7. Therein, the abbreviation V-FC stands for VASP results calculated by the force-constant method (wavenumbers only), V-LR for those calculated by the linear response theory (wavenumbers and intensities). The column G03-B3LYP stands for GAUSSIAN 03 results using B3LYP/6-31G(d) functional and basis set, whereas G03-PW91 column involves those calculated by PW91PW91/6-31G(d) functional and basis set.

In VASP calculations, special settings concerning the displacement of atoms is used when calculating the Hessian matrix. The value of the corresponding parameter was therefore set to  $POTIM = 0.02 \text{ \AA}$ . In addition, dipole corrections (IDIPOL=4) have been taken into account.

The intensities of the normal modes have been evaluated either automatically (in GAUSSIAN 03 package, which contains routines using an older implementation of the force-constant method based on the variation of the dipole moments) or manually by user script (for VASP, which for DFPT calculation serves the matrices of Born effective charge tensors as well as the appropriate vibrational eigenvectors, both needed to calculate intensities using formula as proposed by Gianozzi [42]).

The vibrational intensities were calculated for all modes (i.e.,  $3N$  modes, where  $N$  is the number of atoms), however, only normal modes ( $3N - 6$ ) are presented. For the normal modes, the intensities have been normalized, so that the highest value was set up to 1.000.

A simulation of CH<sub>3</sub>S infrared spectra is to be seen in Fig. 5.14. The calculated frequencies and intensities of normal vibration modes in CH<sub>3</sub>SH may be visually compared with experimental spectra [144] of the substance in gas state (Fig. 5.13).

To allow a comparison with the experimental infrared spectrum, the calculated intensity eigenvalue spectrum was broadened with a Gaussian resolution

$$y = h \cdot e^{-\frac{(x-x_0)^2}{2w^2}}$$

where  $h$  is scaled normalized intensity ( $h = 0.95I$ , dimensionless),  $x_0$  is the corresponding wavenumber [ $\text{cm}^{-1}$ ] and  $w$  is the broadening parameter (we used

Table 5.6: *Methane thiol (CH<sub>3</sub>SH) vibrational normal modes. Wavenumbers in cm<sup>-1</sup> and intensities (in parentheses) dimensionless. <sup>a</sup> Ref. [144].*

#	Vibrational mode	V-FC	V-LR	G03-B3LYP	G03-PW91	Exp <sup>a</sup>
01	C-H stretch (as)	3081	3077 (0.119)	3166 (0.324)	3110 (0.270)	3015
02	C-H stretch (as)	3076	3074 (0.150)	3161 (0.442)	3102 (0.398)	3012
03	C-H stretch (s)	2987	2991 (0.784)	3076 (1.000)	3014 (1.000)	2948
04	S-H stretch	2629	2630 (0.032)	2683 (0.961)	2629 (0.955)	2605
05	C-H deform. (as)	1442	1441 (0.210)	1517 (0.334)	1474 (0.407)	1453
06	C-H deform. (as)	1428	1426 (0.107)	1508 (0.214)	1464 (0.259)	1444
07	C-H deform. (s)	1313	1308 (0.400)	1395 (0.384)	1352 (0.312)	1332
08	C-H rocking	1063	1064 (0.351)	1118 (0.829)	1087 (0.891)	1072
09	C-H rocking	948	943 (0.036)	991 (0.260)	964 (0.336)	956
10	S-H deformation	779	779 (0.036)	809 (0.037)	792 (0.032)	802
11	C-S stretch	687	686 (1.000)	703 (0.101)	694 (0.095)	710
12	H-C-S-H rotation	234	229 (0.417)	249 (0.697)	256 (0.791)	~200

$w = 35 \text{ cm}^{-1}$ ). Both  $x$  and  $y$  axes are inverted as usual in experimental spectra, and the  $x$ -axis has a non-linear scale as desired for the comparison with spectrum from Ref. [144].

The confrontation between theory and experiment in Fig. 5.13 demonstrates very good agreement with experiment – except for the intensity of the eigenmode assigned to C-S stretching. A similar comparison with the intensities calculated using GAUSSIAN (not shown) leads to gross disagreement in the intensity of the S-H stretch and the C-H rocking modes, but better agreement for the C-S stretch mode (disregarding for the moment the general up-shift of all high-frequency modes).

The exact analysis of vibrational eigenvectors was performed in order to elucidate the character of vibrations in a free gas-phase species CH<sub>3</sub>SH and CH<sub>3</sub>S, so that these particular vibrational modes may be later assigned to their analogues in the surface-bound molecules.

The eigenvectors for CH<sub>3</sub>SH are depicted in Fig. 5.15, the analogues for CH<sub>3</sub>S in Fig. 5.16. The figures have been made using scripting within the visualisation package XCrysDen [146].

As both CH<sub>3</sub>SH and CH<sub>3</sub>S are relatively simple species, the interpretation of their vibrational spectra is not that difficult.

For both methane thiol and methane thiolate, one gets 2 asymmetric stretches and 1 symmetric stretch of the C-H bonds within the CH<sub>3</sub> group in the region

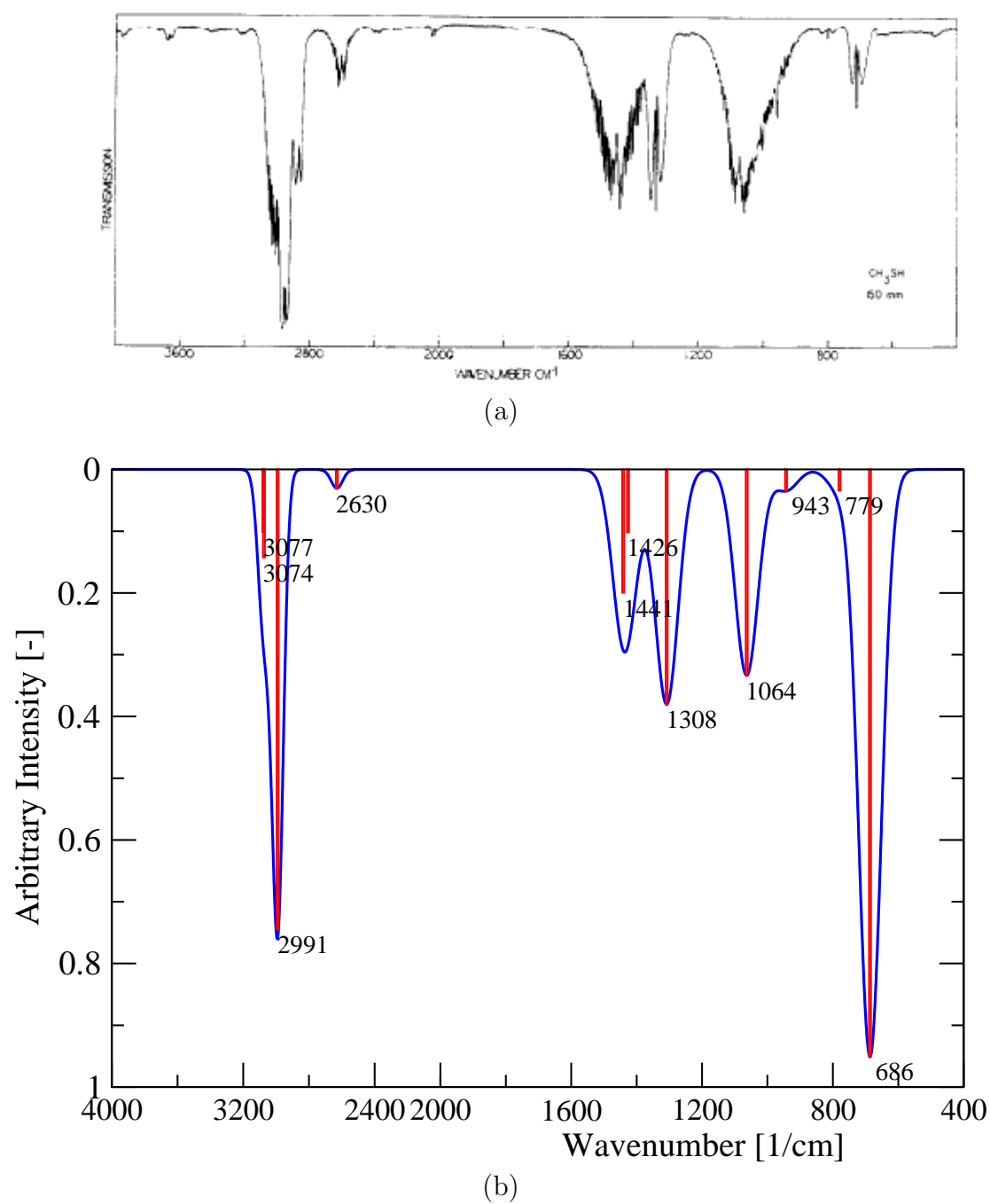


Figure 5.13: *Experimental (a) and simulated (b) vibrational spectra of  $\text{CH}_3\text{SH}$ . Experimental spectrum measured at 25 °C for 10 cm gas path length. Reprint from Ref. [144].*



Table 5.7: Methane thiolate ( $\text{CH}_3\text{S}$ ) vibrational normal modes. Wavenumbers in  $\text{cm}^{-1}$  and intensities (in parentheses) dimensionless. <sup>a</sup> Ref. [145].

#	Vibrational mode	V-FC	V-LR	G03-B3LYP	G03-PW91	Exp <sup>a</sup>
01	C-H stretch (as)	3017	3012 (0.235)	3136 (0.032)	3071 (0.018)	2776
02	C-H stretch (as)	3016	3010 (0.289)	3116 (0.250)	3046 (0.216)	–
03	C-H stretch (s)	2937	2938 (0.577)	3042 (0.089)	2969 (0.042)	2706
04	C-H deform. (as)	1375	1374 (1.000)	1502 (0.252)	1456 (0.260)	1496
05	C-H deform. (as)	1375	1369 (0.944)	1406 (0.185)	1347 (0.173)	–
06	C-H deform. (s)	1285	1280 (0.000)	1370 (0.077)	1323 (0.065)	1313
07	C-H rocking	847	848 (0.219)	885 (0.036)	853 (0.046)	–
08	C-H rocking	843	847 (0.203)	712 (0.011)	713 (0.018)	–
09	C-S stretch	732	727 (0.708)	550 (1.000)	543 (1.000)	727

around  $\sim 3000 \text{ cm}^{-1}$ . As the symmetry for  $\text{CH}_3\text{SH}$  species is broken to  $\text{C}_{2h}$ , the 2 asymmetric C-H stretching modes are slightly degenerated (difference of few  $\text{cm}^{-1}$ , depending on the computational method and basis set used). The symmetric stretch has always the lowest wavenumber.

For C-H deformation vibrations (“umbrella” modes), the situation is very similar (2 asymmetric and 1 symmetric deformation), and the vibrations appear in the spectra as very intensive peaks in the region between  $1250$  and  $1500 \text{ cm}^{-1}$ . According to the selection rules, the symmetric C-H deformation in methane thiolate should excess almost zero intensity. Anyway, due to the slightly broken symmetry, the corresponding peak has been found by experimental measurement.

Between the region of C-H stretches and C-H deformations, the weak peak of the S-H valence stretch may be found at approx.  $2630 \text{ cm}^{-1}$  for  $\text{CH}_3\text{SH}$ , whereas for  $\text{CH}_3\text{S}$ , this peak is of course missing.

Degenerate C-H rocking modes are to be found at approx.  $1000 \text{ cm}^{-1}$  for  $\text{CH}_3\text{SH}$  (the difference is about  $120 \text{ cm}^{-1}$ ), and for  $\text{CH}_3\text{S}$ , these peaks appear at  $848 \text{ cm}^{-1}$  with a small difference of very few  $\text{cm}^{-1}$ .

An important parameter is also the C-S stretching mode with absorption peaks at approx.  $700 \text{ cm}^{-1}$  for  $\text{CH}_3\text{SH}$  and  $730 \text{ cm}^{-1}$  for  $\text{CH}_3\text{S}$ . For methane thiol, one observes S-H deformation mode at approx.  $800 \text{ cm}^{-1}$  (which is, in fact, a kind of scissoring of the C-S-H angle), furthermore, the calculation also gives a low-frequency mode at approx.  $230 \text{ cm}^{-1}$ , for which the antisymmetric rotation of the SH and the  $\text{CH}_3$  moieties is specific.

The results for  **$\text{CH}_3\text{SH}$**  may be summarized as follows:

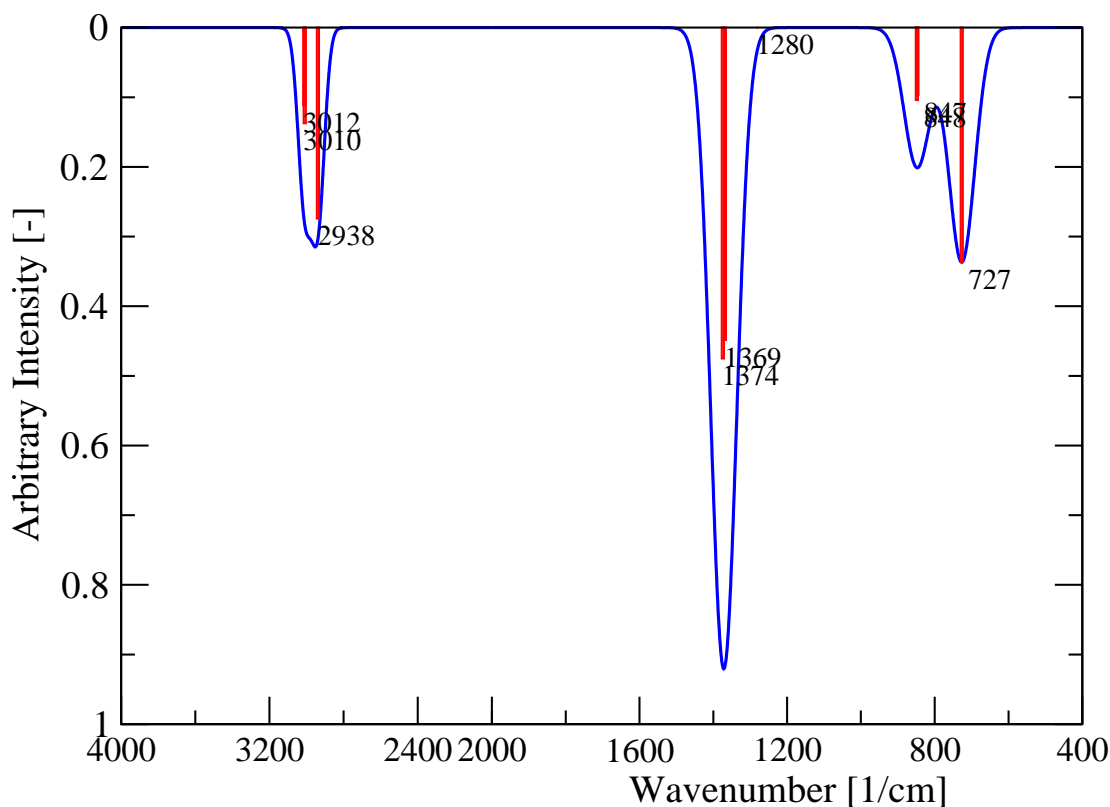
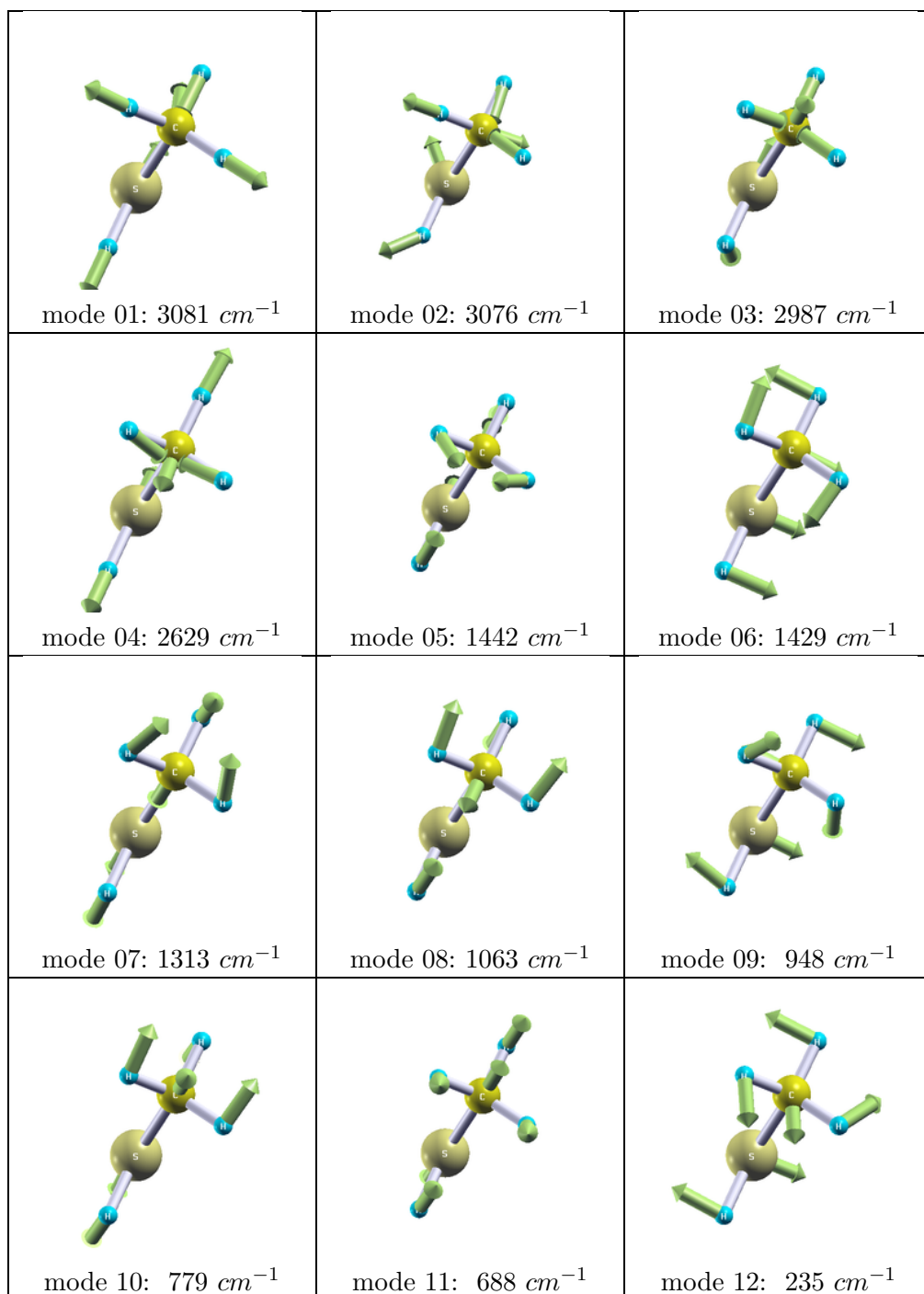


Figure 5.14: *Simulated vibrational spectra of CH<sub>3</sub>S.*

1. Force-constant and linear-response calculations performed using VASP are in excellent agreement – the largest discrepancy is  $5\text{ cm}^{-1}$  for the C-H deformation and rocking modes.
2. Larger differences are found between the force-constant calculations using VASP and GAUSSIAN – the difference is largest ( $85\text{ cm}^{-1}$ ) for the C-H stretching mode.
3. Compared to the experimental IRS data [144] the C-H and S-H stretching frequencies calculated using VASP are too high by 24 to  $66\text{ cm}^{-1}$ , C-H and S-H deformation and rocking modes are too low by up  $23\text{ cm}^{-1}$ , the C-S stretching mode is too low by the same amount (calculations using the FC method and VASP). The differences in the C-H and S-H stretching frequencies can largely be attributed to the neglect of anharmonic corrections which are largest for the high-frequency C-H stretching modes. The low-frequency torsional mode around  $230\text{ cm}^{-1}$  could not be resolved by IRS. Estimates based on the barrier height for hindered rotation from microwave data yield an estimate

Figure 5.15: *Eigenvectors of CH<sub>3</sub>SH IR normal modes.*

of  $200\text{ cm}^{-1}$  (Ref. [144]).

4. The eigenfrequencies from the GAUSSIAN calculations (using the same exchange-correlation functional as in the plane wave calculations) are too high by up to  $95\text{ cm}^{-1}$ . These differences are too large to be attributed to anharmonicity alone. To examine the influence of the choice of the functional, we have also performed a calculation using GAUSSIAN and a hybrid functional (B3LYP [141, 142]). This leads to a further enhancement of the eigenfrequencies varying between about  $60\text{ cm}^{-1}$  for the C-H stretching modes and  $30\text{ cm}^{-1}$  for the C-H rocking modes. The normal-mode intensities are hardly influenced by the choice of the functional.

Substantial differences are found between the normal-mode intensities predicted by VASP (linear response theory) and GAUSSIAN (dynamical dipole approximation). In the former case the highest intensity (normalized to 1) is predicted for the C-S stretching mode, in the latter case for the symmetric C-H stretching mode. Major differences are also found in the intensities predicted for the S-H stretch and C-H rocking modes.

A free methane thiolate radical  $\text{CH}_3\text{S}$  exists only as a reaction intermediate, the vibrational eigenstates can not be measured using conventional spectroscopies. A further difficulty arises from the fact that in the ground state with  $C_{3v}$  symmetry the highest occupied molecular orbital is only partially occupied and hence subject to a Jahn-Teller distortion. The ground state configuration has  $C_s$  symmetry, the Jahn-Teller distortion lowers the total energy by  $55\text{ meV/molecule}$ . The ground state is twofold degenerate with one of the C-H bonds in the methyl group slightly longer, the other two shorter than average. The two possible configurations are separated by a saddle-point which has also  $C_s$  symmetry, but two long and one short C-H bond and is only about  $0.5\text{ meV}$  higher in energy. Similar geometries have also been derived from MP2 calculations which found a higher barrier of  $6\text{ meV}$  separating the degenerate ground state configurations [138, 139]. In addition, methane thiolate has a first excited electronic state which is known to be pre-dissociative, with a C-S bond-length stretched to about  $2.05\text{ \AA}$ .

Vibrational eigenfrequencies for both the ground state and the first excited state have been derived from the vibronic analysis of the laser-induced fluorescence data [147, 145, 148] and four-wave mixing spectroscopy [149, 150]. For the ground-state of  $\text{CH}_3\text{S}$  Chiang and Lee [145] reported possible vibrational frequencies at  $2776, 2706, 1496, 1313, 727,$  and  $586\text{ cm}^{-1}$ , which were tentatively assigned to the asymmetric and symmetric C-H stretching, the asymmetric C-H deformation, the C-S stretching and C-H rocking modes. Interestingly, significantly higher asymmetric and symmetric stretching modes of  $3006$  and  $2966\text{ cm}^{-1}$  were proposed for the

first excited electronic state of the radical. From the analysis of the vibrational fine structure of the ultraviolet photoelectron spectra, Schwartz et al. [151] estimated a symmetric C-H stretching frequency of  $2960\pm 30\text{ cm}^{-1}$  and a C-S stretching frequency of  $725\pm 15\text{ cm}^{-1}$ , in agreement with earlier experiments by Janousek and Brauman [152] who also reported a C-H deformation mode at  $1360\text{ cm}^{-1}$ .

A detailed analysis of vibronic dynamics of  $\text{CH}_3\text{S}$  in the ground and first excited states based on a model Hamiltonian was presented by Marenich and Boggs [153] who criticized the vibrational assignments made by Chiang and Lee [145]. The assignment of the C-H deformation modes was confirmed, while that of the modes at the upper and lower ends of the spectral distribution was criticized. Our theoretical results derived using the same methods as used for methane-thiol are summarized in Table 5.7 which also includes the available experimental data. Drissi et al. [139] have calculated the vibrational eigenfrequencies within their quantum-chemical methods (MP2 with 6-31+G\* basis set), we use their results also for comparison.

The results obtained with the force-constant and linear-response approaches in VASP agree within a maximum deviation of  $5\text{ cm}^{-1}$ . Calculations with GAUSSIAN lead to higher C-H stretching and deformation modes, and also to a much more pronounced splitting of the symmetric C-H deformation and C-H rocking modes. The most significant discrepancy, however, is the very low C-S stretching frequency resulting from the GAUSSIAN simulations. The MP2 calculations of Drissi et al. [139] yield for all modes involving hydrogen atoms eigenfrequencies which are about 50 to  $150\text{ cm}^{-1}$  higher than the DFT results with VASP, but good agreement is found for the C-S stretching mode. Comparison with experiments is difficult for the reasons discussed above. Our calculations predict much higher C-H stretching frequencies than those derived from laser-induced fluorescence [147, 145, 148], but are in good agreement with the estimate derived from the vibrational fine-structure of the photoemission data [151]. Reasonable agreement exists for the symmetric C-H deformation mode, even very good agreement for the C-S stretching mode.

Compared to the methane-thiol molecule the C-H stretching and deformation modes are red-shifted by  $-28$  to  $-67\text{ cm}^{-1}$ , the C-H rocking modes by  $-105$  and  $-216\text{ cm}^{-1}$ , while the C-S stretching mode undergoes a modest blue-shift by  $+17\text{ cm}^{-1}$ . The blue-shift of the C-S mode reflects the contracted C-S bond-length, the softer C-H modes the fact that the bonding capacity of the C-atom is now concentrated on the C-S bond.

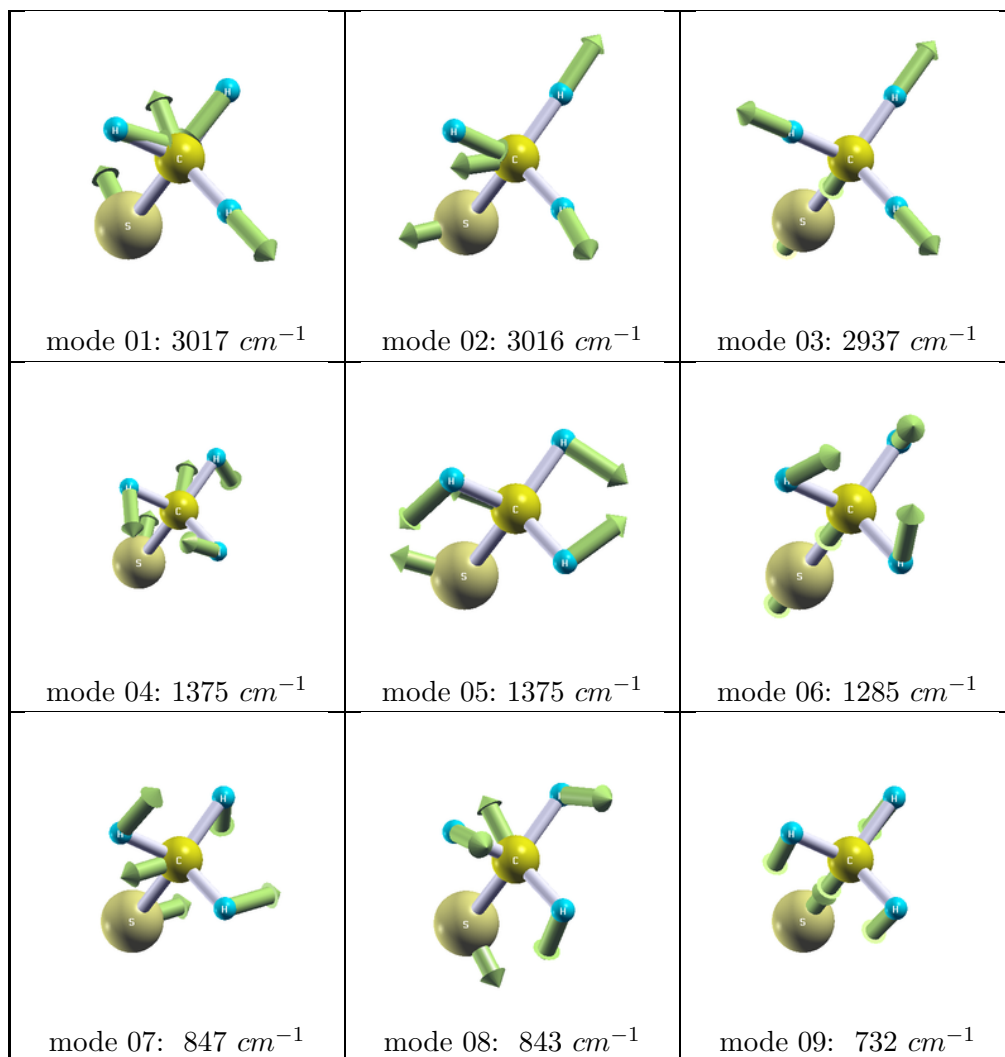
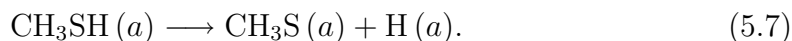


Figure 5.16: *Eigenvectors of CH<sub>3</sub>S IR normal modes.*

## 5.4 Gas-Phase Dissociation of Methane Thiol

In the subsequent chapters, one attempts to present the theoretical study of a chemical reaction on a metal surface ( $a$  stands for adsorbed state):



In fact, in advance it may be useful to look at this dissociation reaction as if it proceeded in the gas-phase as well. The point is an ability to quantify the differences in the thermodynamics of the chemical changes.

In order to evaluate the thermodynamical properties of the reaction in the gas phase, the total energies of the several different molecular (or radical) species had to be evaluated. The data are summarized in Table 5.8.

Table 5.8: *Total energies of free gas-phase molecules and radicals.*

Species (Molecule / Radical)	Energy [eV]
CH <sub>3</sub> SH	-27.696775
CH <sub>3</sub> S	-22.644887
CH <sub>3</sub> S (static) <sup>a</sup>	-22.360499
CH <sub>3</sub> S...H (5 Å, static) <sup>a</sup>	-23.756368
CH <sub>3</sub> S-SCH <sub>3</sub>	-48.059281
CH <sub>3</sub>	-18.152711
SH	-5.933521
H <sub>2</sub>	-6.789217
H	-1.118910

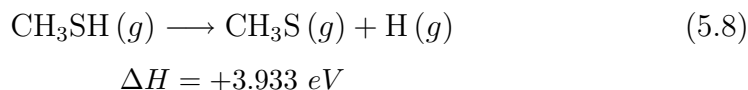
<sup>a</sup> static calculation, i.e. the CH<sub>3</sub>S was taken as a fragment of from CH<sub>3</sub>S and was not relaxed.

For the calculations on the energies of the species, a rectangular unit cell (with dimensions  $a = 14$  Å,  $b = 15$  Å and  $c = 16$  Å) was used, in contrast to the other previous calculations on small systems, where 10 Å cubic cell was the first choice. The reason for it was to neglect the impact of cell symmetry. Spin-polarization was used for each species and appeared to have considerable influence on the total energy, especially for species with unpaired electrons (radicals).

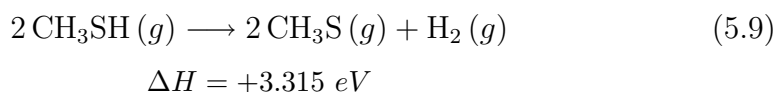
The obtained total energies enable one to make simple (though informative) judgements on the thermodynamics of some reactions proceeding in the gas phase, based on energy difference between total energies of the reaction products and reactants. Therefore, this *energy difference*  $\Delta E$  may be referred to as the *reaction enthalpy*  $\Delta H$  at 0 K temperature.

Thus we may state the reaction enthalpies  $\Delta H$  of the following reactions ( $g$  stands for gaseous state):

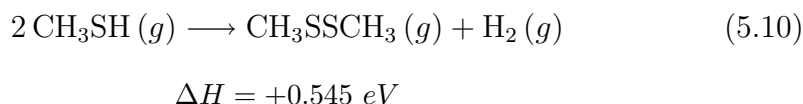
1. Simple dissociation of methane thiol to methane thiolate radical and atomic hydrogen



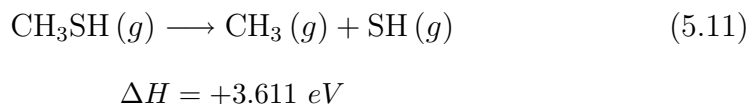
2. Dissociation of methane thiol to form methane thiolate radical and molecular hydrogen



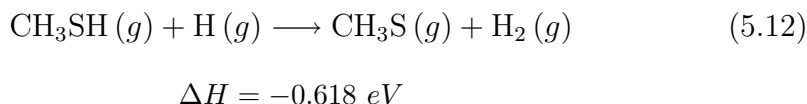
3. Disproportionalization of methane thiol to form dimethyl disulfide and molecular hydrogen



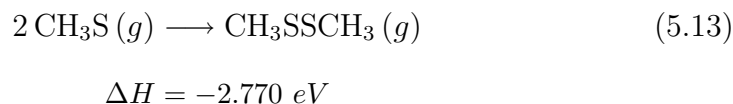
4. Dissociation of methane thiol to methyl radical and sulfhydryl radical



5. Methane thiolate radical formation by propagation from methane thiol



6. Dimerization of methane thiolate to form dimethyl disulfide



7. Dimerization of atomic hydrogen to form molecular hydrogen





The reaction (5.8) is the simplest description of methane thiol dissociation by only breaking the S-H bond to form the methane thiolate radical  $\text{CH}_3\text{S}^\bullet$  and hydrogen radical  $\text{H}^\bullet$ . This one-step reaction is strongly endothermic (by +3.933 eV), however, one is straightforward able to elucidate the possible mechanism of the S-H bond-breaking, which should be in principle similar to the bond breaking in the hydrogen molecule – the elongation of the bond to be broken.

Experimental measurements (ultraviolet photolysis) give values of the S-H bond dissociation energy in  $\text{CH}_3\text{SH}$  of about +3.74 eV, which is in good agreement with our calculated result [155, 156]. Based on reaction mechanism (5.8), one may get a typical dissociation curve (see Fig. 5.17), which is in fact very similar to those of  $\text{H}_2$  dissociation. This potential energy curve was obtained by a loop of static total energy calculations of  $\text{CH}_3\text{S-H}$  systems and elongating the S-H bond between 0.7 and 4.9 Å. The disadvantage of the reaction mechanism 5.8 is the production of unstable radicals as well as its highly endothermic character, which allows us to say that such reaction (induced e.g. by photolysis) is very unfavourable.

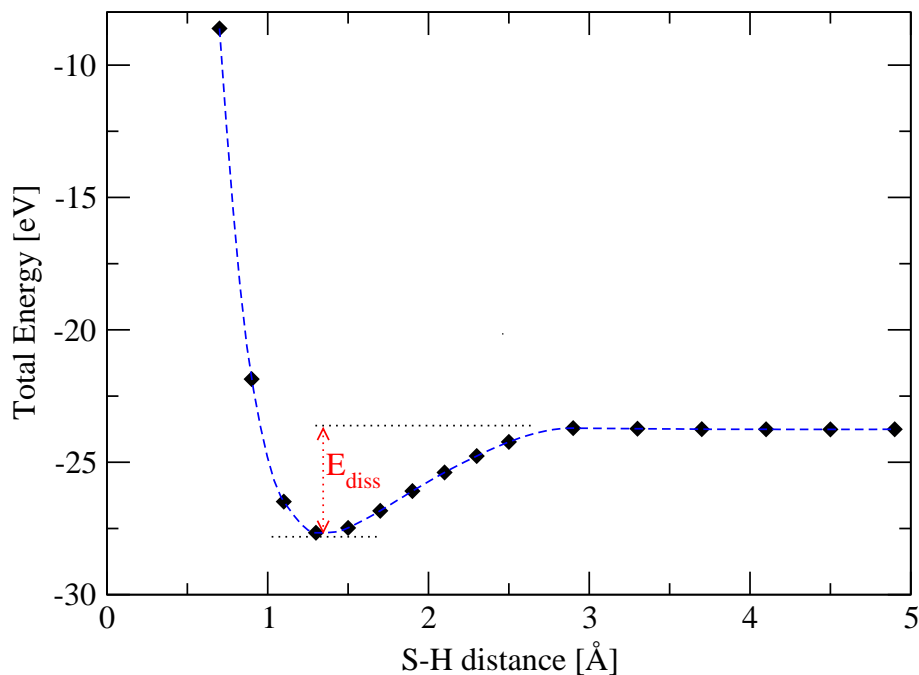


Figure 5.17: *Dissociation curve of S-H bond breaking in  $\text{CH}_3\text{SH}$ .*

Reaction (5.9) describes in fact two consecutive reactions, whereas the first step is the reaction (5.8) and the second step is the recombination (dimerization) of the free hydrogen radicals to form the  $\text{H}_2$  molecule. This reminds on the dissociation of  $\text{CH}_3\text{SH}$  on metal surfaces. Even if there is some energy gain due to hydrogen dimerisation, the reaction (5.9) is still strongly endothermic by almost +3.8 eV.

Reaction (5.10) takes into account – as an addition to the 2 preceding mechanisms – also the recombination of the methane thiolate radical. It is also known, that for methane thiolate adsorbed on metal surfaces, a reversible formation of dimethyl disulfide has been experimentally detected. It is commensurate with the statement, that in gas phase, this consecutive reaction shifts the dissociation of methane thiol into exothermic region (by approx.  $-0.5$  eV). Anyway, if the formation of dimethyl disulfide would prevail, there would be no perfectly chemisorbed monolayers on metal surfaces.

Mechanism (5.11) describes the cleavage of the C-S bond in  $\text{CH}_3\text{SH}$  forming  $\text{CH}_3\bullet$  and  $\text{H}\bullet$  – methyl and sulfhydryl (or thioxy) free radicals. It is assumed to be strongly endothermic by 3.6 eV. Even if mechanism (5.11) is energetically more favourable than (5.8) by approx. 0.3 eV, the cleavage of the S-H bond is rather dominating in all experiments on photodissociation [155, 156].

Reaction scheme (5.12) shows the propagation of radicals, as electroneutral thiol molecule produces thiolate radical and the extremely stable dihydrogen is formed. For this reason, the reaction pathway is exothermic by approx.  $-0.6$  eV and it has been observed in photolysis experiments. In other words, once the hydrogen radical is formed, it promotes the formation of thiolate from thiol.

The reactions (5.13) and (5.14) show how energetically favourable the recombination of  $\text{CH}_3\text{S}\bullet$  and  $\text{H}\bullet$  free radicals may be. If methane thiol dimerizes, an energy of about  $-3.3$  eV is released. The dimerization of hydrogen atom yields a vast of energy ( $-4.55$  eV), which is a very slightly overestimated result (by 1.6%) with respect to the experimental value by Balakrishnan [157], who evaluated the  $\text{H}_2$  dissociation energy (the reverse reaction) to be  $+4.48$  eV.

As to summarize, the dissociation of methane thiol is in principle a very strongly endothermic process. In the following chapters, the way will be shown how to turn this reaction (in fact, mainly the Eqns. (5.9) and (5.10)) exothermic. The key point is the adsorption on metals.

## 5.5 Methane Thiol on (111)-Surfaces of Ni, Pd, Pt

Experimental measurements [52] reveal that methane thiol ( $\text{CH}_3\text{SH}$ ) happens to adsorb readily on Ni-group metal surfaces forming preferably  $(\sqrt{3} \times \sqrt{3})\text{R}30^\circ$  superstructure, which corresponds to the surface coverage of  $\theta=1/3$ . Depending on the vapor pressure, this on-surface superstructure may vary to allow the existence of lower (but not higher) surface coverages of methane thiol (e.g.,  $\theta=1/4$  which would be commensurate for  $c(2 \times 2)$  cells).

For this study, surface coverage of  $1/3$  was chosen as an appropriate model of the real system. Thus we used the supercells which have been already relaxed as the clean surfaces (Chapter 5.2) and allowed the molecules to adsorb.

### 5.5.1 Adsorption Geometry

For the calculations of adsorbed structures, the following four high-symmetry surface sites have been chosen:

- the **on-top** position,
- the **bridge** arrangement,
- the **fcc-hollow** (face-centered cubic) and
- the **hcp-hollow** (hexagonal closed-packed) arrangements.

After the processing of a sufficiently accurate geometry relaxation, structural and energetic parameters for each of this arrangements have been evaluated.

The relaxations have been performed in 2 steps:

1. *pre-relaxation* using  $3 \times 3 \times 1$   $k$ -point mesh in the real space (leading to 5  $k$ -points in the reciprocal space),
2. *accurate relaxation* using  $6 \times 6 \times 1$   $k$ -point mesh in the real space (leading to 54  $k$ -points in the reciprocal space).

Such stepwise relaxation saves computational time and enables to retain a moderately dense  $k$ -point mesh of 0.04  $k$ -points/Å.

For all calculations, the two upmost metal layers and all atoms of the adsorbed molecule have been allowed to relax from their positions, whereas for the sulfur atom (which binds directly to the surface) the lateral ( $x$  and  $y$ ) coordinates have been fixed.

In some cases, because of severe convergence problems, the lateral coordinates for the topmost metal layer atoms had to be fixed as well. This applied to relaxations on platinum, since the calculations resulted in shifting the topmost metal layer under the fixed sulfur atom, thus forming a reconstructed surface, far away from the expectations of what really happens with the surface upon physisorption.

The deposition of the molecule onto the surface has been performed by means of "concatenation" of the unit cells containing molecule atoms and the metal bulk atoms. Elementary cells of 30 Å height have been retained, causing vacuum layers "fill" more than 15 Å (50%) of the cell height in case of each metal surface model.

An important observable, that one may gain draw from calculations on adsorbed systems, is the adsorption energy  $E_{ads}$  (which in fact matches to adsorption enthalpy  $\Delta H$ ). In principle, it is the energy difference between the initial and the final state of the appropriate chemical-physical process. In the case of adsorption, one simply subtracts the total energies of the final structure (metal substrate with adsorbate) and the initial structures (sum of the energy of the clean metal substrate and that of free adsorptive molecule):

$$E_{ads} = E_{adsorbate+slab} - (E_{adsorbate} + E_{slab}) \quad (5.15)$$

As previously mentioned, we decided to perform a detailed study of CH<sub>3</sub>SH adsorption on metallic surfaces, which will be presented here (i.e. adsorbate=CH<sub>3</sub>SH, slab=Ni<sub>15</sub>, Pd<sub>15</sub> Pt<sub>15</sub> respectively).

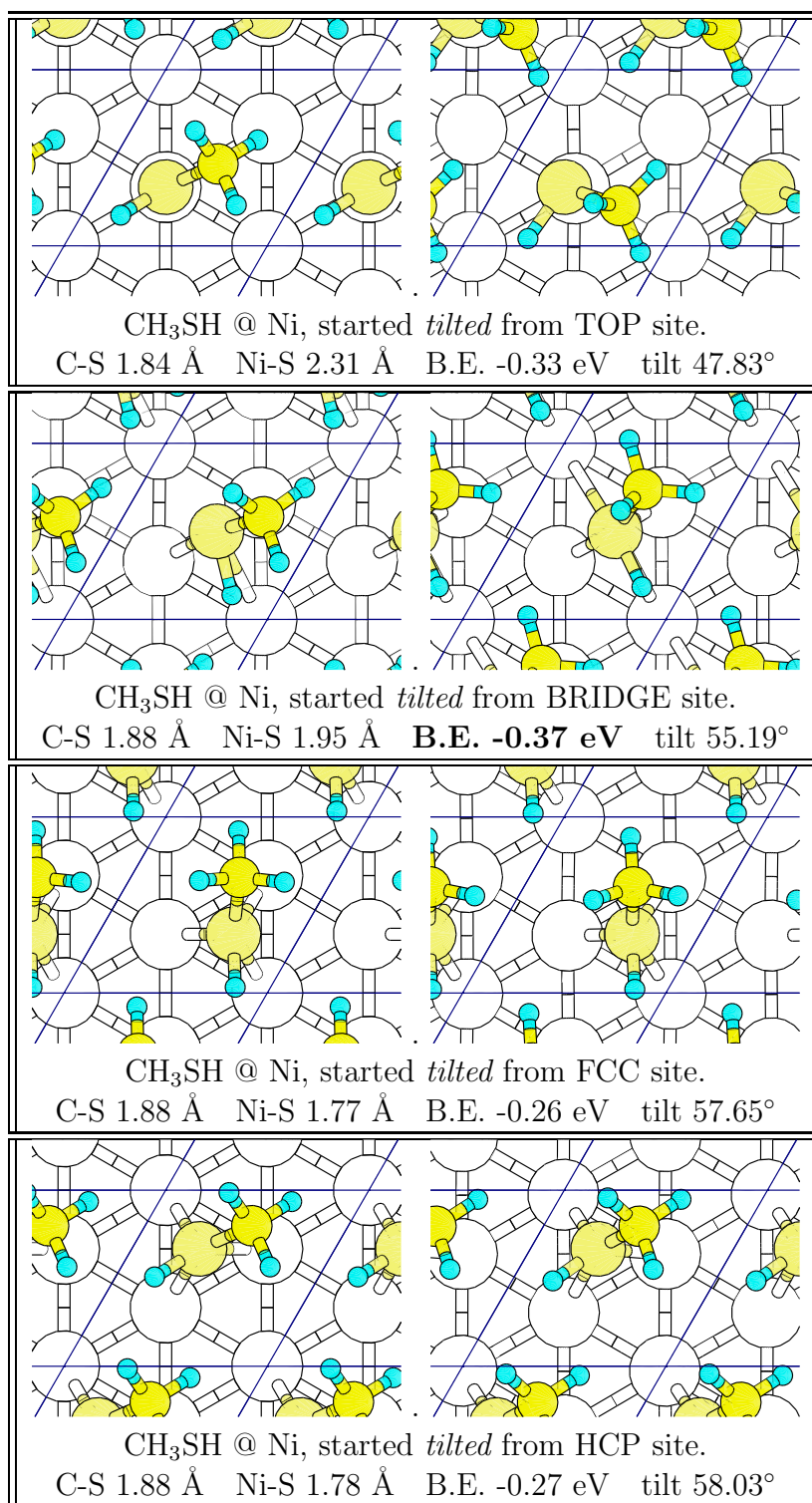
Calculated results of adsorption geometry parameters and adsorption energy within CH<sub>3</sub>SH self-assembly on Ni, Pd, and Pt to form ( $\sqrt{3} \times \sqrt{3}$ )R30° monolayer are summarized in Table 5.9. According to surface positions, where the ionic relaxation for the adsorbate was started, the high-symmetry adsorption sites are assigned as *top*, *bridge*, *fcc-hollow* and *hcp-hollow*. However, the resulting adsorption site differs in some cases from the set-up configuration, meaning that the topmost metal layer atoms undergo in-plane shifting, in other words a slight reconstruction.

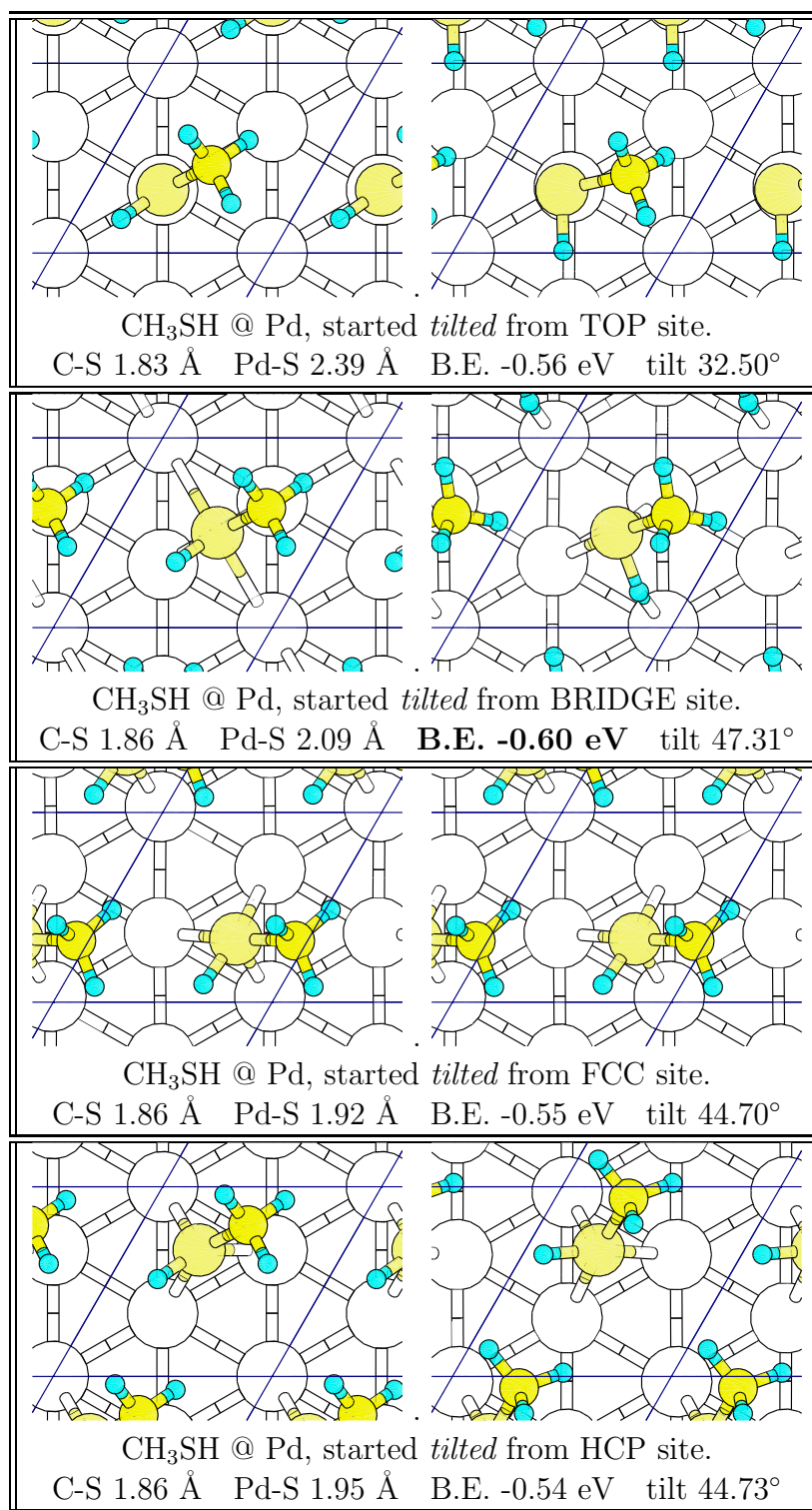
In order to visualize the adsorption arrangement of methane thiol on particular metal surfaces on all high-symmetry surface sites, a tabulated overview of input structures (always the left-hand picture for each relaxation) and optimized structures (the equilibrium position, right-hand picture) are plotted in Figs. 5.18, 5.19 and 5.20 for Ni, Pd and Pt, respectively.

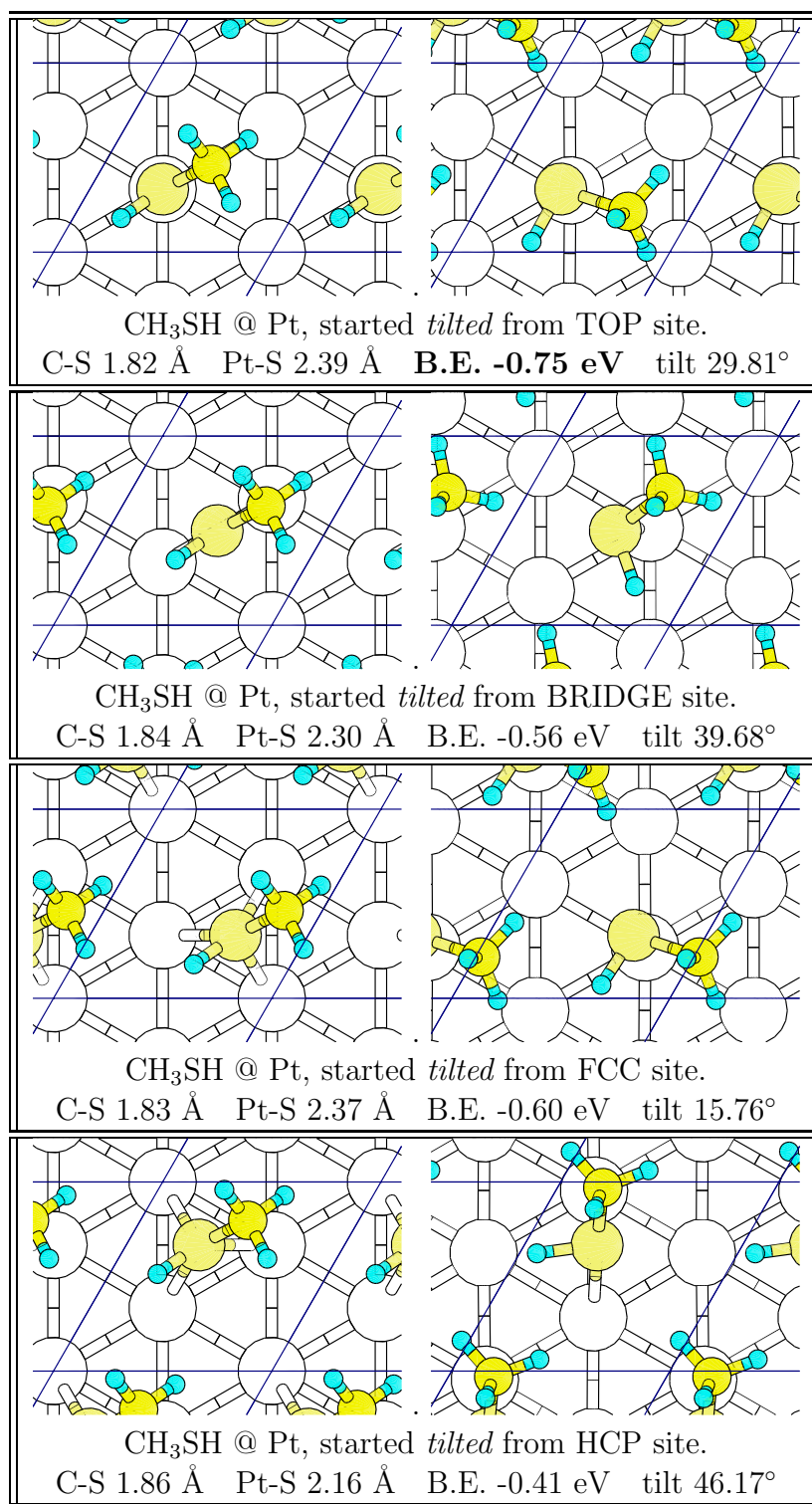
Table 5.9: Adsorption energy and geometry parameters of  $CH_3SH$  monolayer on Ni, Pd and Pt (111)-surfaces.

Starting conf.	top	bridge	fcc-hollow	hcp-hollow
<b>Nickel</b>				
Ads. site <sup>a</sup>	t/t/u	<b>b/t/u</b>	h/b-t/d	h/b-t/d
$E_{ads}$ [eV]	-0.33	<b>-0.37</b>	-0.26	-0.27
M-S [Å]	3.35 2.19 3.32	2.94 2.37 2.20	2.37 2.20 2.29	2.20 2.40 2.27
M-S <sup>b</sup> [Å]	2.31	1.95	1.77	1.78
C-S [Å]	1.84	1.88	1.88	1.88
S-H [Å]	1.36	1.37	1.37	1.37
M-H <sup>c</sup> [Å]	2.55	2.34	2.49	2.48
Tilt <sup>d</sup> [°]	47.8	55.2	57.6	58.0
C-S-H [°]	93.6	92.4	90.8	91.1
<b>Palladium</b>				
Ads. site <sup>a</sup>	t/h/d	<b>b/t/u</b>	h/b/u	h/b/u
$E_{ads}$ [eV]	-0.56	<b>-0.60</b>	-0.55	-0.54
M-S [Å]	3.59 2.32 3.64	3.11 2.64 2.38	2.39 2.59 2.58	2.39 2.59 2.61
M-S <sup>b</sup> [Å]	2.39	2.09	1.92	1.95
C-S [Å]	1.83	1.86	1.86	1.86
S-H [Å]	1.36	1.42	1.37	1.37
M-H <sup>c</sup> [Å]	2.52	1.84	2.52	2.58
Tilt <sup>d</sup> [°]	32.5	47.3	44.7	44.7
C-S-H [°]	96.5	96.1	92.5	92.3
<b>Platinum</b>				
Ads. site <sup>a</sup>	<b>t/t/u</b>	t/t/u	t/t/u	b/t/u
$E_{ads}$ [eV]	<b>-0.75</b>	-0.56	-0.60	-0.41
M-S [Å]	3.63 2.30 3.60	3.26 3.17 2.34	2.31 3.46 3.53	2.38 2.73 3.23
M-S <sup>b</sup> [Å]	2.39	2.30	2.37	2.16
C-S [Å]	1.82	1.84	1.83	1.86
S-H [Å]	1.36	1.36	1.36	1.37
M-H <sup>c</sup> [Å]	2.57	2.62	2.69	2.30
Tilt <sup>d</sup> [°]	29.8	39.7	15.8	46.2
C-S-H [°]	95.3	94.6	94.8	94.8

<sup>a</sup> Adsorption site look: nearest site position (**hollow-bridge-top**) / -CH<sub>3</sub> fragment tilt (**hollow-bridge-top**) / C-H bond tilt (**up-down**); <sup>b,c</sup> Perpendicular distance of S (or H) from the surface plane; <sup>d</sup> Tilting of the C-S bond axis w.r.t. metal surface plane.

Figure 5.18: Adsorption modes of CH<sub>3</sub>SH on Ni(111) surface.

Figure 5.19: Adsorption modes of CH<sub>3</sub>SH on Pd(111) surface.

Figure 5.20: Adsorption modes of CH<sub>3</sub>SH on Pt(111) surface.



### Adsorption Energies

The achieved adsorption energies lie in the range of  $-0.37$  eV on Ni and  $-0.75$  eV on Pt, indicating that the molecule is only physisorbed via weak polarization-induced forces.

The site dependence of the adsorption energy is only rather modest, suggesting a rather high mobility of the adsorbed molecules on the surface. For example, the barrier for a hopping between two bridge sites via a top site is only  $0.04$  eV on Ni and Pd surfaces. On Pt(111) surfaces, the barrier for a migration between two on-top sites via a hollow is slightly higher, about  $0.15$  eV. These small energy differences are in accordance with the experimental observation of a rather diffuse LEED pattern for the low-temperature molecularly adsorbed species [110]. The mobility of the molecules on the surface via diffusion is very easily achieved.

### Adsorption Geometries

Due to the weak binding to the substrate and the low symmetry of the methane thiol molecule, relaxation to an equilibrium geometry is a rather tedious process. To make sure that the optimization does not end only in a local minimum, we used altogether four different starting geometries, with the S atom placed above a high symmetry site (on-top, bridge, fcc or hcp hollow) as mentioned above, and with tilted orientation of the C-S bond towards the surface. Relaxation of the two top layers of the substrate has been permitted. In Table 5.9 we have characterized each entry by the initial and final positions of the S atom and the direction of the tilt of the C-S bond. The final adsorption site was always slightly off symmetry.

We have used the distances from the three nearest substrate atoms to characterize the adsorption site: if one distance is distinctly shorter than the other two, the site was characterized as on-top (t), for two short distances as bridge (b), for three approximately equal distances as hollow (h). However, for both bridge and hollow sites, the short distances may differ by up to  $\sim 0.3$  Å.

On a Ni(111) surface, the relaxations starting from all four initial sites lead to different local minima differing up to  $0.1$  eV in energy. The shorter metal M-S distances are around  $2.3 \pm 0.1$  Å. The tilt angle varies between  $42.2^\circ$  and  $32.0^\circ$  (with respect to the surface normal), it increases with increasing distance from the surface (from hollow to top). The orientation of the methyl group is always such that the distance between the terminal H-atoms and the metal atoms of the substrate is as large as possible to minimize the Pauli-repulsion. The shortest distance between the hydrogen atom of the thiol group and a surface atom is around  $2.4$  Å, allowing for the formation of a weak hydrogen bond.

Adsorption of the molecule leads to an activation of the S-H and C-S bonds. The S-H bond is slightly stretched from 1.35 Å in the gas-phase molecule to 1.37 Å, the C-S bond is elongated from 1.82 Å to 1.88 Å. The modest increase of the S-H bond length indicates only a weak activation for de-hydrogenation. The formation of this dense thiol overlayer reduces the inward relaxation of the top Ni-layer, but a weak interlayer contraction is also calculated for the second and third layer.

On a Pd(111) surface, the situation is similar, as all initial adsorption sites lead to local energy minima differing by at most 0.06 eV and shortest M-S distances between 2.3 and 2.4 Å. The slightly increased height above the surface correlates with a larger tilt angle.

The energetically most stable configuration on Pd is a bridge position, tilted towards a surface atom, and it differs from the three local minima in top or hollow sites by a rather short M-H distance of only 1.84 Å and a more strongly stretched S-H bond length of 1.42 Å. We have cross-checked this result by repeating the relaxation with slightly different initial configurations, but the final relaxation configuration was always the same.

On the other hand, we could not find configurations with similar short M-H distances starting from other initial sites. The elongation of the C-S bond is smaller than for adsorption on a Ni surface. Even the clean Pd(111) surface shows a weak expansion of the first and a small contraction of the second interlayer distance. The formation of a thiol-layer enhances the expansion of the first interlayer distance to more than 1 %, while the contraction of the second layer spacing is reduced.

In contrast to Ni and Pd surfaces, on Pt(111) the preferred adsorption site is on top of a substrate atom, with a very large tilt angle of 60° relative to the surface normal (30° w.r.t surface plane). In this configuration, the length of the C-S bond remains unchanged, only the S-H bond is stretched to 1.36 Å. On Pt, a position of the molecule in one of the three-fold hollows is unstable. From the fcc hollow, the molecule relaxes to a top position differing from the equilibrium configuration in terms of tilt angle and shortest M-H distance. This result indicates that the multidimensional potential-energy surface has multiple minima. From the hcp hollow the molecule relaxes to bridge position with a strong tilt of the C-S bond representing another local potential energy minimum. The relaxation of the Pt substrate is similar as observed for Pd, but the outward-relaxation of the top-layer is now even more pronounced. Concerning the computational aspects, thiol on Pt was the system where unless the lateral coordinates of S atom were fixed, the molecule relaxed into the surface under total cleavage of both C-S and S-H bonds, giving a non-realistic structure with low adsorption energy.

### 5.5.2 Electronic Properties

The electronic properties of this weakly interacting adsorbate/substrate complex are dominated by the interaction between the molecular eigenstates of the methane thiol molecule falling into the energy range covered by the  $d$ -band of the metal.

Figs. 5.21, 5.22 and 5.23 show the plots of the projected electronic density of states (PDOS) for the most stable adsorption configurations of  $\text{CH}_3\text{SH}$  on Ni, Pd, and Pt, respectively, which were discussed in the previous chapter.

In these plots, the electronic density of states of the metal atoms in the surface layer is colored in green, on the S atom in red. For comparison, the vertical bars (magenta) mark the molecular eigenstates of the free molecule. Energies are given relative to the Fermi level.

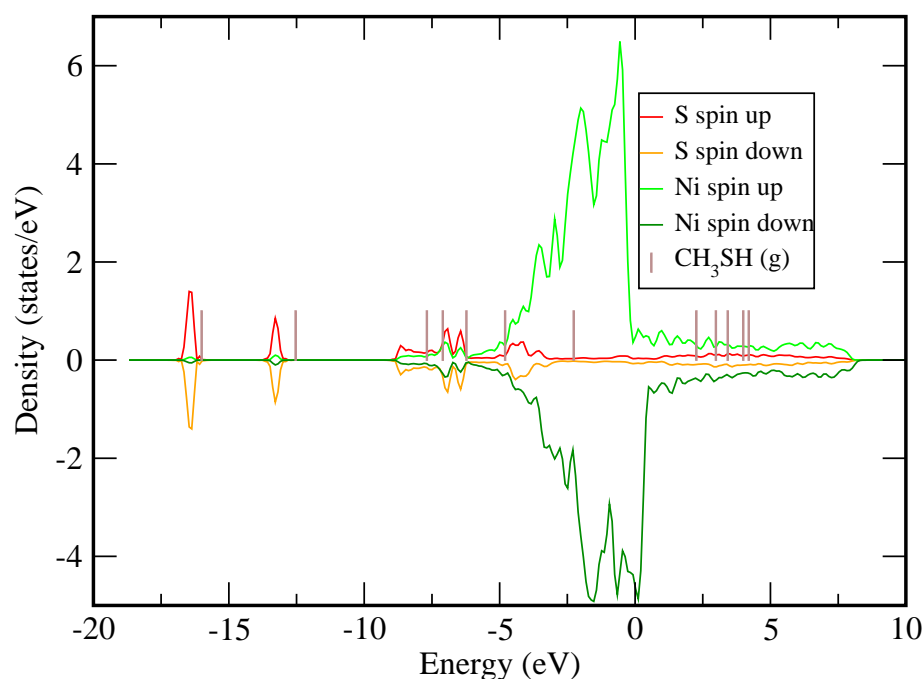


Figure 5.21: *PDOS diagram of  $\text{CH}_3\text{SH}$  @  $\text{Ni}(111)$ .*

The overall picture is the same for all substrates, considering their slightly higher (Pt), medium (Pd) and lower (Ni)  $d$ -band widths and the weak spin-polarization of Ni.

According to the DFT calculations, the HOMO-LUMO gap of the free molecule is 4.52 eV, i.e. of the same order of magnitude like the  $d$ -band width of the substrate.

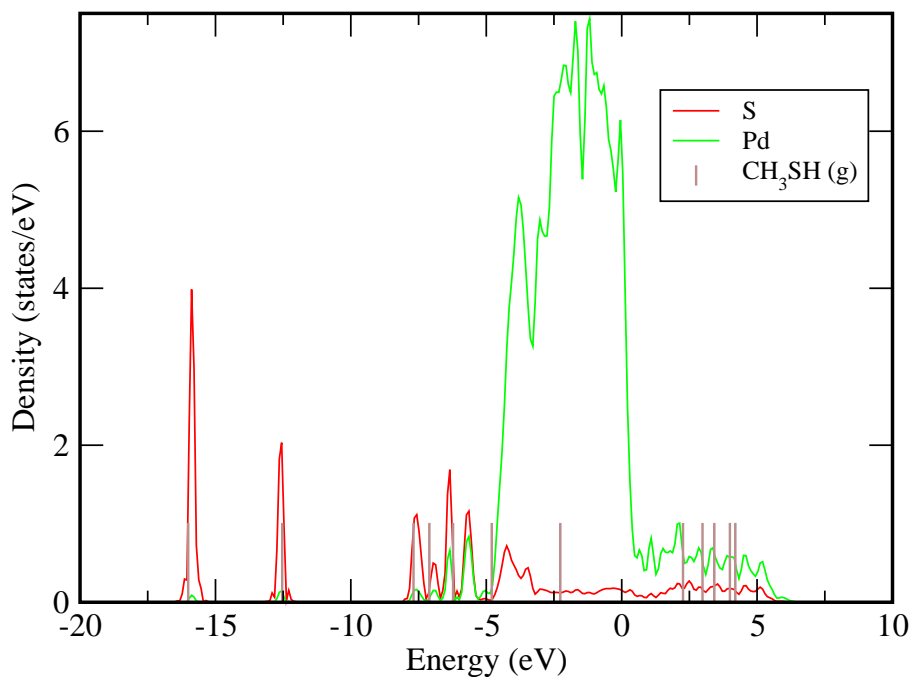


Figure 5.22: PDOS diagram of  $\text{CH}_3\text{SH}$  @  $\text{Pd}(111)$ .

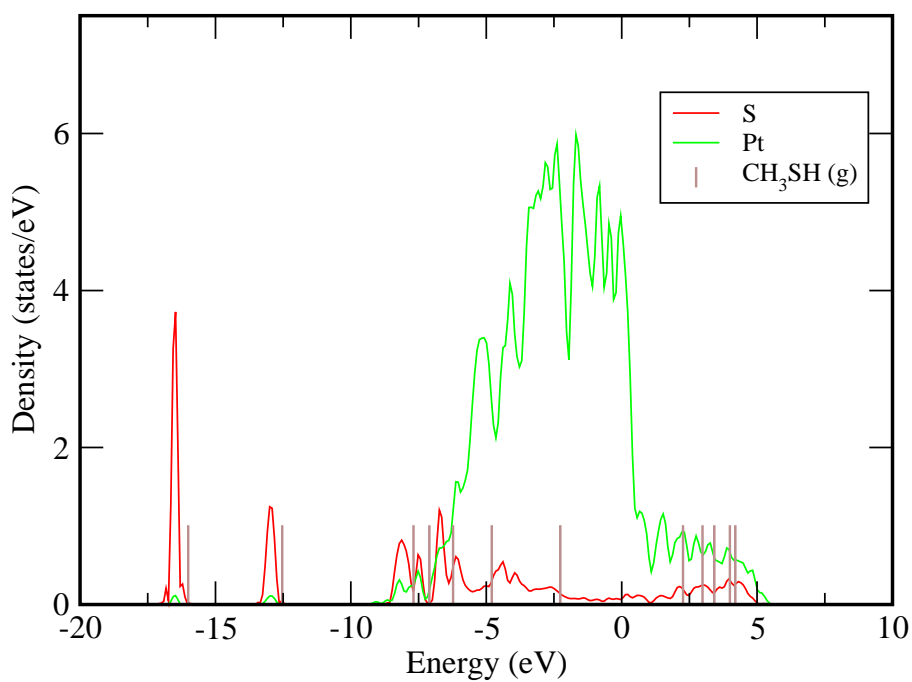


Figure 5.23: PDOS diagram of  $\text{CH}_3\text{SH}$  @  $\text{Pt}(111)$ .

If the energy scales of the density of states of the substrate and of the molecular eigenstate are aligned at the Fermi level, the position of the HOMO corresponds roughly to the center of the  $d$ -band, while the next molecular eigenstates formed by C-S and S-H bonding states at a binding energy of  $-4.80$  eV falls at the lower edge of the  $d$ -band of Ni and Pd and about 2 eV above the band edge of Pt.

The LUMO is located within the empty s-p band of the substrate. Adsorption leads to a hybridization of the highest molecular eigenstates with the  $d$ -band, leading to a shift of the occupied states to higher binding energies and the formation of a broad band of states containing an admixture of the LUMO. The incipient occupation of these antibonding states is responsible for the increased S-H and C-S bond lengths. The molecular eigenstates located at the edge of the metal band are also shifted to higher binding energies and mix with the metal  $d$ -states.

Furthermore, the formation of a dense methane thiol overlayer also leads to a reduction of the work function to 4.88 eV ( $\Delta\varphi = -0.24$  eV) for Ni, 5.10 eV ( $\Delta\varphi = -0.20$  eV) for Pd and 5.57 eV ( $\Delta\varphi = -0.21$  eV) for Pt. Even if the decrease of the workfunction seems to be in our calculations not very significant, this effect is used experimentally in tuning-up of inorganic electrodes.

### 5.5.3 Vibrational Analysis

The nature of bonding of the CH<sub>3</sub>SH molecule to the metal surfaces was further investigated by calculation of the vibrational (IR) spectra of the most stable configuration for each metal surface. The vibrational eigenmodes of the treated dense ( $\sqrt{3} \times \sqrt{3}$ )R30° layers of methane thiol on the (111) surfaces of Ni, Pd, and Pt have been calculated using both the force-constant and linear-response methods.

For the calculation of the vibrational eigenmodes, the metal atoms in the 2 topmost surface layers have been allowed to move, whereas the positions of the atoms in the deeper layers have been frozen. Only the equilibrium adsorption geometries have been used: On Ni and Pd surfaces with the S atom on a bridge-site, while on Pt the S atom is located on-top of a surface atom. On all three surfaces, the C-S axis is strongly tilted towards the surface normal, or in other words, lays nearly parallel with the surface plane. Adsorbate-substrate bonding is only weak, therefore the changes in eigenfrequencies may not be expressed by strong shifts.

The particular vibrational normal modes are listed in Table 5.10, comparing both force-constant (FC) and linear response (LR) approaches with the available experimental data (Ni and Pt only). As in each systems, 9 atoms are allowed to relax, there are altogether 27 degrees of freedom expressed by the same amount of vibrational modes. However, the modes with lower eigenfrequencies correspond to deformations of the top layers of the substrate. The assignment of the modes is based on the calculated eigenvectors.

For CH<sub>3</sub>SH/Ni(111) we note very good agreement between the force-constant and linear-response calculations – the largest discrepancies of 23 cm<sup>-1</sup> are found for a C-H rocking and the C-S stretching mode. The most pronounced changes with respect to the eigenmodes of gas-phase methane-thiol are:

1. A strong red-shift of the C-S and S-H stretching modes by -145(-167) and -213(-221) cm<sup>-1</sup>, respectively, as predicted by the FC and LR calculations.
2. A strong blue-shift of the modes involving a torsion of the methyl and S-H groups around the C-S axis in different directions. The C-H stretching modes undergo only a small changes, while C-H deformation and rocking modes are red-shifted by about 60 cm<sup>-1</sup> on average. An important observation is also the increased splitting of the asymmetric C-H stretching and deformation modes reflecting the broken symmetry of the adsorption complex in a bridge site with a tilted C-S axis. The blue-shift of the torsion mode reflects the restricted mobility of the molecule due to the binding to the substrate.

Table 5.10: Normal vibration modes for the most stable configurations of  $CH_3SH$  on Ni, Pd and Pt (111)-surfaces. <sup>a</sup> Ref. [100], <sup>b</sup> Ref. [107].

# Mode description	Nickel $\tilde{\nu}_{Ni}^{ads}$ [cm <sup>-1</sup> ]			Palladium $\tilde{\nu}_{Pd}^{ads}$ [cm <sup>-1</sup> ]			Platinum $\tilde{\nu}_{Pt}^{ads}$ [cm <sup>-1</sup> ]			$\tilde{\nu}^{free}$ [cm <sup>-1</sup> ]
	FC	LR (int)	exp <sup>a</sup>	FC	LR (int)	exp	FC	LR (int)	exp <sup>b</sup>	LR (int)
01 C-H stretch (as.)	3095	3089 (0.003)	3003	3091	3086 (0.003)	–	3087	3151 (0.000)	3010	3077 (0.119)
02 C-H stretch (as.)	3075	3072 (0.003)	–	3080	3074 (0.000)	–	3069	3063 (0.007)	2985	3074 (0.150)
03 C-H stretch (s.)	2970	2974 (0.002)	2920	2978	2974 (0.001)	–	2967	2979 (0.004)	2910	2991 (0.784)
04 S-H stretch	2416	2409 (0.046)	2560	1918	1918 (0.030)	–	2503	2512 (0.027)	2570	2630 (0.032)
05 C-H def. (as.)	1419	1425 (0.004)	1446	1431	1430 (0.001)	–	1420	1421 (0.001)	1460	1441 (0.210)
06 C-H def. (as.)	1398	1403 (0.005)	–	1409	1410 (0.000)	–	1395	1393 (0.001)	–	1426 (0.107)
07 C-H def. (s.)	1230	1238 (0.001)	1330	1260	1262 (0.000)	–	1283	1359 (0.058)	1345	1308 (0.400)
08 C-H rocking	987	996 (0.059)	1065	958	970 (0.015)	–	1033	1280 (0.010)	1060	1064 (0.351)
09 C-H rocking	849	872 (0.021)	975	894	899 (0.019)	–	934	1003 (0.026)	975	943 (0.036)
10 S-H deformation	743	748 (0.038)	820	733	750 (0.000)	–	776	935 (0.139)	820	779 (0.036)
11 C-S stretch	542	519 (0.137)	710	583	576 (0.061)	–	665	712 (0.029)	725	686 (1.000)
12 H-C-S-H rotation	466	458 (0.106)	–	423	443 (0.064)	–	535	655 (0.044)	–	229 (0.417)
13 Pt-S stretch	274	318 (0.002)	–	216	239 (0.012)	–	274	285 (0.944)	320	–
14 Ni-S / Pd-S str.	225	276 (0.299)	320	168	210 (1.000)	–	188	212 (0.119)	–	–
15	218	225 (0.130)	–	159	169 (0.515)	–	166	137 (0.052)	–	–
16	211	219 (0.175)	–	153	156 (0.289)	–	120	124 (0.000)	–	–
17	206	212 (1.000)	–	150	150 (0.274)	–	116	123 (0.610)	–	–
18	193	205 (0.086)	–	145	145 (0.348)	–	113	116 (0.260)	–	–
19	179	187 (0.032)	–	142	134 (0.091)	–	111	115 (1.000)	–	–
20	163	163 (0.771)	–	114	108 (0.004)	–	106	96 (0.357)	–	–
21	158	157 (0.183)	–	106	106 (0.047)	–	92	90 (0.887)	–	–

HREELS data for  $\text{CH}_3\text{SH}/\text{Ni}(111)$  have been reported by Rufael et al. [100]. The interpretation of the experimental data is difficult, because deposition at 100 K leads to the formation of a multilayer of  $\text{CH}_3\text{SH}$  on the Ni surface and heating to an even modest temperature of 125 K leads to the disappearance of the characteristic S-H stretching peak at  $2560\text{ cm}^{-1}$  and hence to the formation of a thiolate rather than a thiol overlayer. This observation corresponds to our finding that on a Ni(111) surface dissociation of methane-thiol is non-activated. The results included in Table 5.10 are taken from Table 1 of Rufael et al. [100] and refer to a condensed multilayer. This explains why the observed shift of the eigenmodes with respect to gas-phase thiol is much more modest than predicted by our calculations. Still, the relatively largest change is the red-shift of the S-H stretching mode while the fact that the C-S stretching mode is unchanged relative to the gas phase suggests that the measured intensities are dominated by contributions from molecules in the physisorbed multilayer.

Similar changes in the vibrational eigenmodes have also been calculated for the system  $\text{CH}_3\text{SH}/\text{Pt}(111)$ . However, the red-shift of the S-H and C-S stretching modes is less pronounced than on Ni(111). This agrees with a different adsorption configuration close to an on-top position, a weaker elongation of the C-S bond length and a stronger tilt of the C-S axis. For  $\text{CH}_3\text{SH}/\text{Pt}(111)$  HREELS data have been reported by Koestner et al. [106] for saturated layers annealed at different temperatures. The data listed in Table 5.10 refer to an annealing temperature of 10 K (the highest temperature at which a S-H stretching peak can be observed) and refer probably to an unspecified multilayer coverage. This would explain the modest change with respect to the gas-phase molecule.

For  $\text{CH}_3\text{SH}/\text{Pd}(111)$ , we have found a special adsorption configuration with the thiol-hydrogen forming a weak bond to a surface metal-atom. In the vibrational spectrum this is reflected in a very strong red-shift of the S-H stretching mode by more than  $-700\text{ cm}^{-1}$ , while the red-shift of the C-S mode is intermediate between that calculated for Ni and Pt surfaces. No experimental results are available for comparison.

We have also calculated the normal mode intensities (closed in parentheses in Table 5.10) for adsorbed methane-thiol, using the Born effective charges from the linear response approach. The highest intensities are always predicted for the low-energy modes involving displacements of the heavy substrate atoms. Among the eigenmodes of the adsorbate, the highest intensities are predicted for the C-S stretching mode, the torsional mode, the S-H stretch and the C-H rocking modes. However, as no data for comparison are available, these results are not reported in detail.



The eigenvectors corresponding to the the first 24 of 27 vibrational modes are shown in Figs. 5.24 and 5.25 for adsorption on nickel, Figs. 5.26 and 5.27 for palladium, and Figs. 5.28 and 5.29 for platinum. Note that for good visual orientation, the length of the vectors (the green arrows) is normalized to be the same in each mode for each atom. Although this normalization causes a rotation of the actual  $3N$ -dimensional vector (as each triplet of coordinates is scaled by a different factor), it does not rotate the corresponding plot of the  $N$  subvectors in the 3-dimensional projection and only affects the arrow length.

Unfortunately if the subvectors would remain unscaled, mostly only the vibrations including the heavy substrate atoms would be visible, as these modes have larger reduced mass and therefore the force-constants as well.

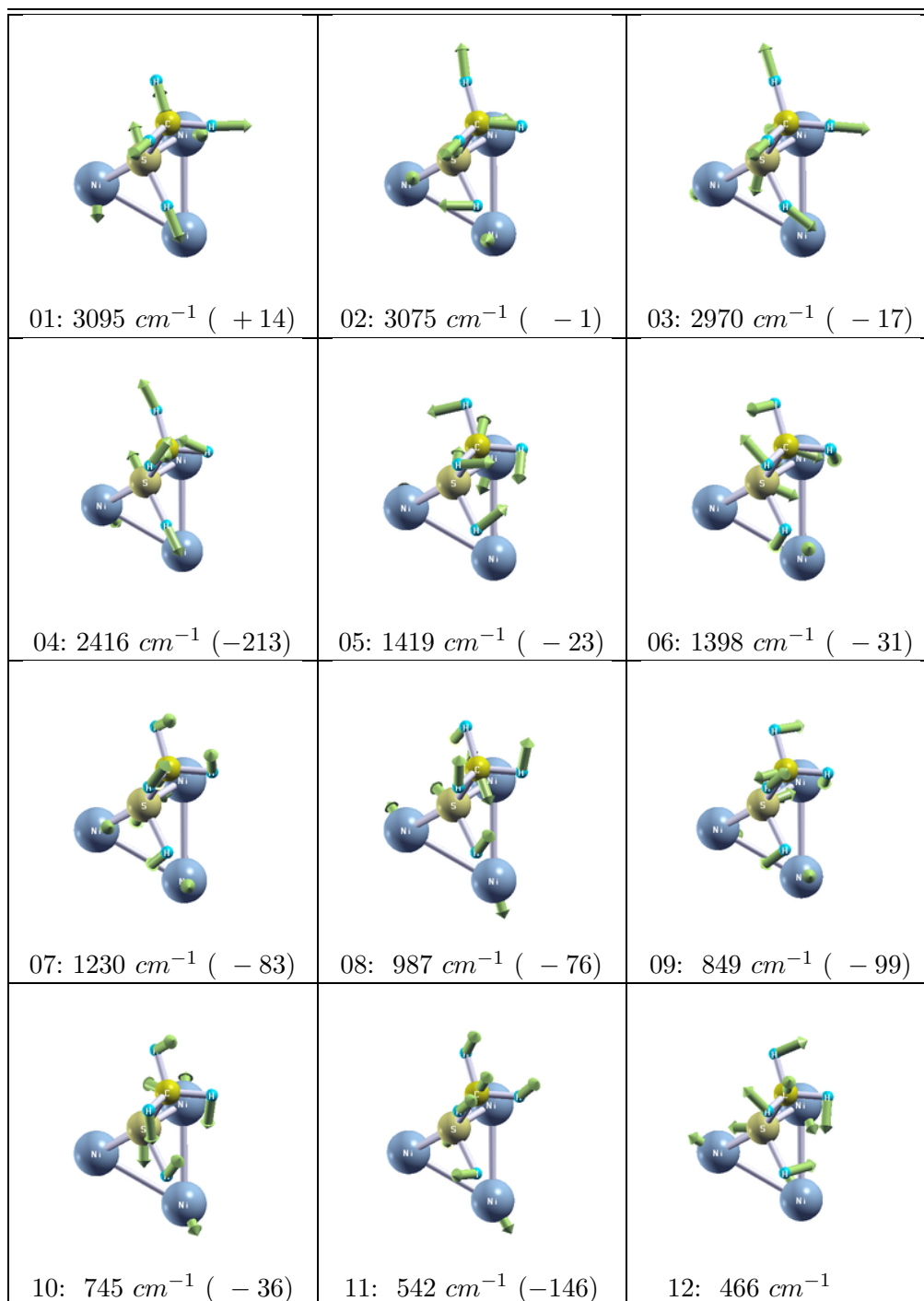
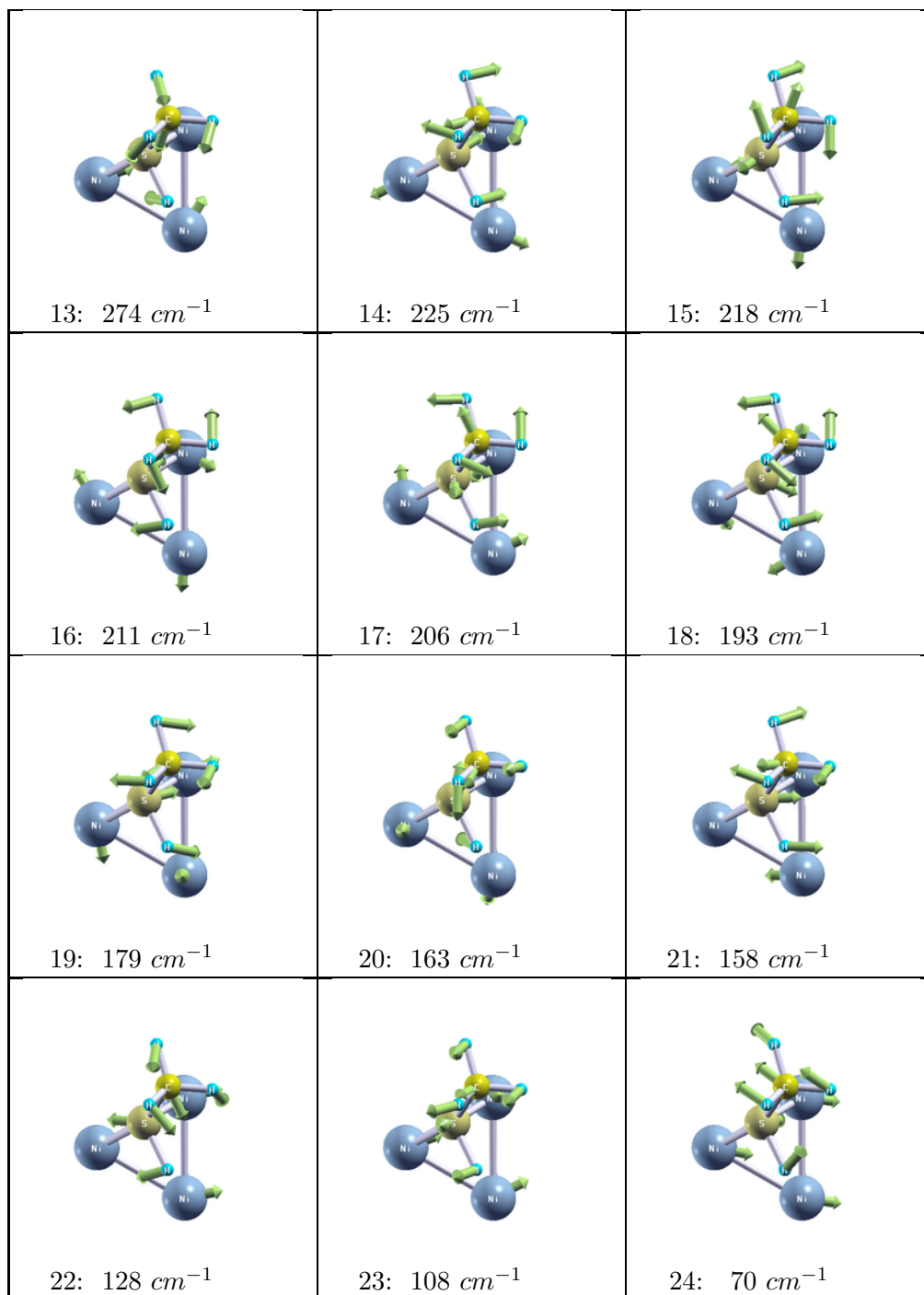


Figure 5.24: *Eigenvectors of CH<sub>3</sub>SH @ Ni(111) IR normal modes.*

Figure 5.25: Eigenvectors of  $\text{CH}_3\text{SH}$  @  $\text{Ni}(111)$  IR normal modes (continued).

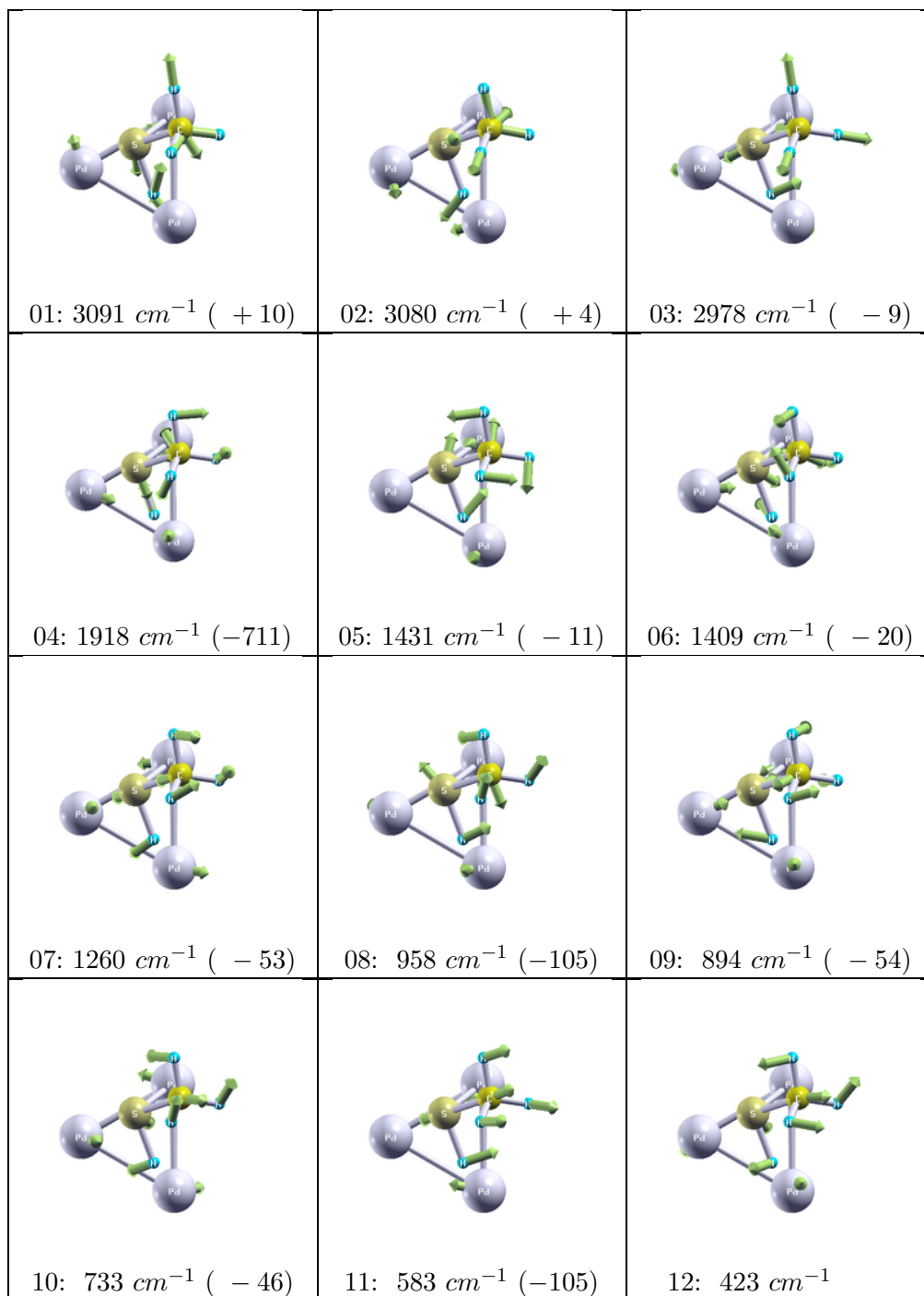
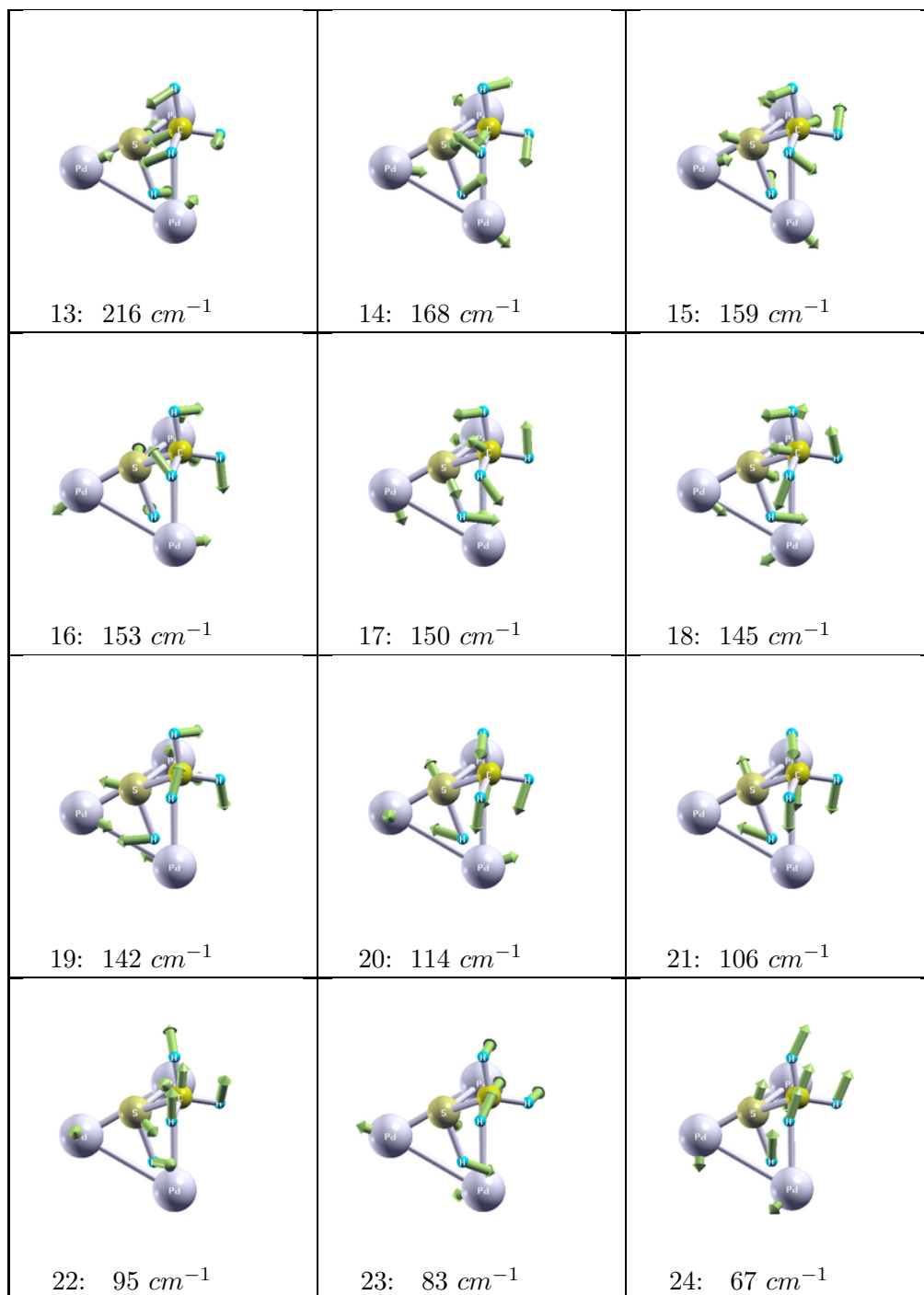


Figure 5.26: *Eigenvectors of  $\text{CH}_3\text{SH}$  @  $\text{Pd}(111)$  IR normal modes.*

Figure 5.27: Eigenvectors of  $\text{CH}_3\text{SH}$  @  $\text{Pd}(111)$  IR normal modes (continued).

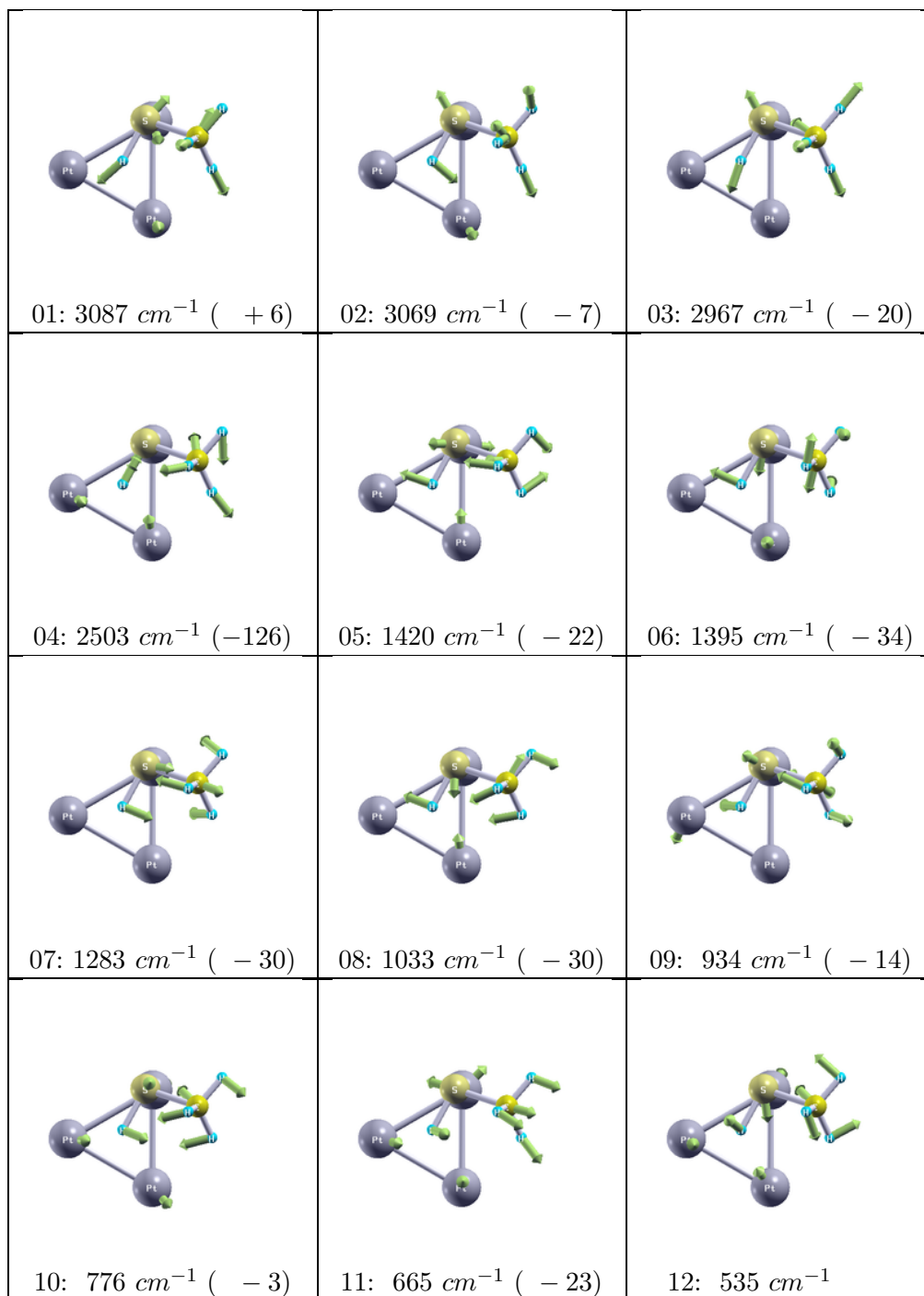
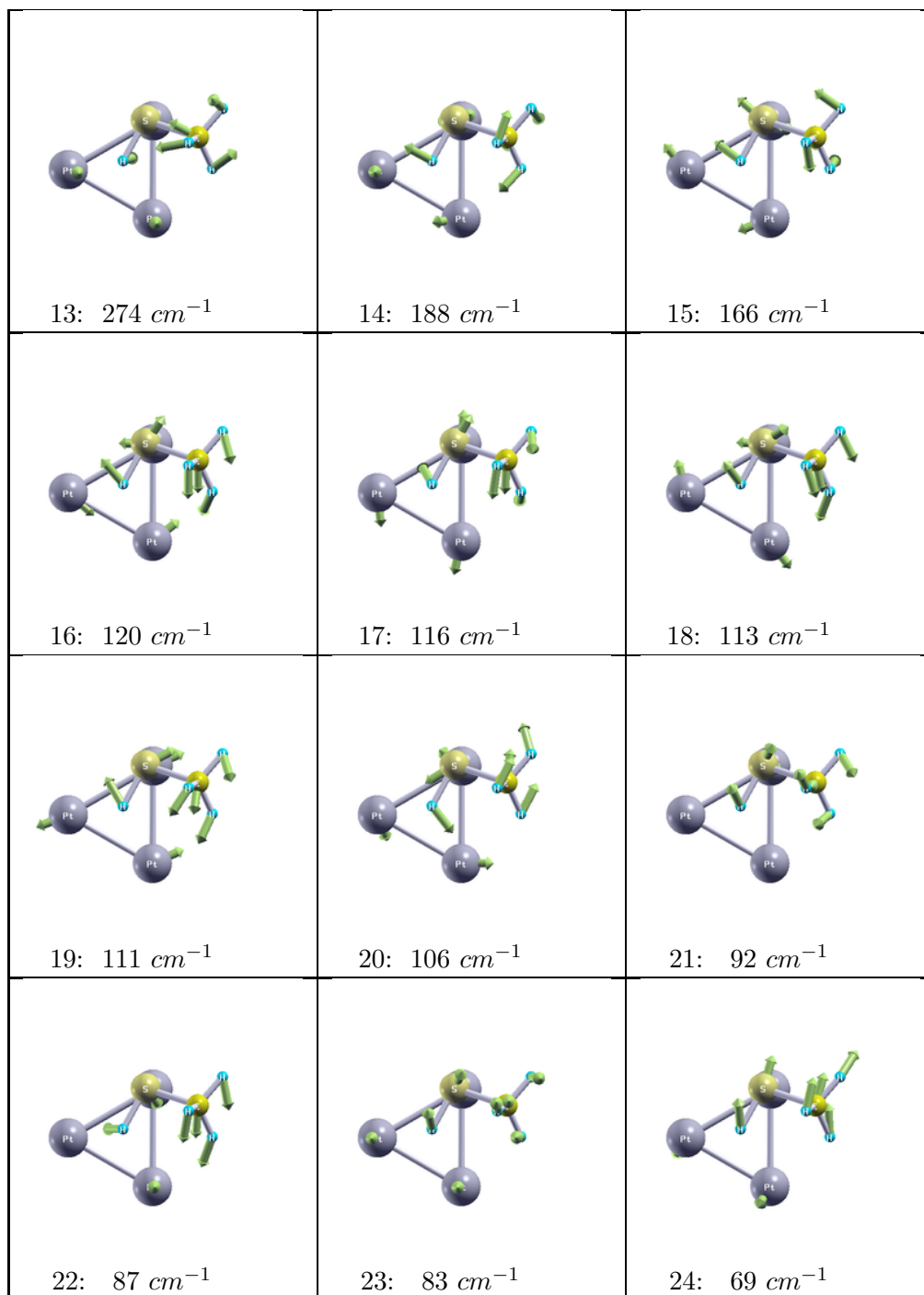
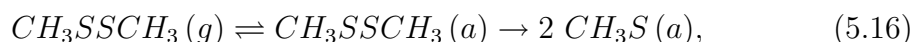


Figure 5.28: *Eigenvectors of CH<sub>3</sub>SH @ Pt(111) IR normal modes.*

Figure 5.29: Eigenvectors of  $\text{CH}_3\text{SH}$  @  $\text{Pt}(111)$  IR normal modes (continued).

## 5.6 Methane Thiolate on (111)-Surfaces of Ni, Pd, Pt

Similarly like the weak interaction of methane thiol with metal surface, the stronger adsorption of methane thiolate radical has been studied. Although surface-bound methane thiolate  $\text{CH}_3\text{S}(a)$  may also be produced by means of dimethyl disulfide  $(\text{CH}_3\text{S})_2$  adsorption and subsequent surface-induced dissociation [102]:



we concentrate on generation of methane thiolate by surface-induced dissociation of adsorbed methane thiol. In fact, the thiolate monolayer can be faster formed via (5.16) rather than  $\text{CH}_3\text{SH}$  dissociation route:



since the surface-bound hydrogen in the latter mechanism occupies perspective adsorption sites, whereas the hydrogen desorption lowers the entropy of the system.

The results for the formation of a close-packed methane-thiolate overlayer with a coverage of  $\Theta = 1/3$  and a  $(\sqrt{3} \times \sqrt{3})R30^\circ$  periodicity are summarized in Table 5.11. In view of the difficulties to find the most stable geometry of the adsorbate/substrate complex (as documented by some conflicting results reported in the literature), we have used eight different starting geometries on each metal, with the sulfur atom in one of the four high-symmetry sites (t, b, fcc-h, hcp-h) and either a perpendicular or a tilted C-S bond. The initial tilt-angle relative to the surface normal was always  $45^\circ$ , the direction of the tilt was towards a neighboring bridge-site for the S-atom on-top of a metal atom and towards a neighboring substrate atom for the molecule in a bridge or hollow position.

### 5.6.1 Adsorption Geometry

For Ni(111) surface,  $\text{CH}_3\text{S}$  adsorbed in a tilted configuration with the S atom close to a fcc hollow site has the highest adsorption energy of about  $-2.77$  eV/molecule

On the Pd(111) surface we find a similar adsorption geometry with a slightly larger tilt of the molecular axis from the surface normal and an adsorption energy of  $-2.73$  eV/molecule. On a Pt(111) surface, the stable adsorption site is halfway between a fcc hollow and a neighboring bridge position, and we found an adsorption energy of  $-2.78$  eV.



A complete overview of adsorption configurations of methane thiolate on particular metal surfaces on all high-symmetry surface sites is also done in form of tables including initial guesses (always the left-hand picture for each relaxation) and relaxed structures (the equilibrium position, right-hand picture). The situation for initial tilting of  $90^\circ$  with respect to metal surface plane (i.e.  $0^\circ$  relative to the surface normal; the “perpendicular” configuration) and approx.  $45^\circ$  (“tilted”) is plotted in Figs. 5.30 and 5.31 for Ni, Figs. 5.32 and 5.33 for Pd, 5.34 and 5.35 for Pt.

Only a few previous DFT results are available for comparison. Jiao et al. [158] report adsorption energies for methane thiolate in fcc hollows of Ni(111) and Pd(111) of  $-3.07$  eV/molecule and  $-3.11$  eV/molecule, respectively, but on Pt(111) an adsorption energy of only  $-2.65$  eV. Only upright adsorption in the hollow was considered. For Pt(111) Ghiringhelli et al. [159] report for the same coverage a lower adsorption energy of  $-2.42$  eV/molecule in a hollow position. For the other two metals, results have been reported only for a lower coverage of  $1/4$  ML. The fcc hollow is the stable adsorption site on all three substrates, with adsorption energies decreasing from  $-2.93$  eV/molecule on Ni to  $-2.67$  eV/molecule on Pt. All their results refer to an upright position of the  $\text{CH}_3\text{S}$  radical. Majumder[160] has studied the adsorption of isolated  $\text{CH}_3\text{S}$  on Pt(111) (using a  $(5 \times 5)$  surface cell) and finds an adsorption energy of  $-3.03$  eV/molecule for a bridge-adsorbed species, rather a bit overestimated compared to our result. For the equilibrium geometries, however, we note appreciable differences between our results and those from earlier investigations.

Our results displayed in Table 5.11 emphasize the importance of choosing a starting geometry which does not bias the final result. Adsorption of  $\text{CH}_3\text{S}$  in a perpendicular geometry on a top or a hollow site of a fcc (111) surface leads to an adsorbate/substrate complex which could, in principle, have full  $C_{3v}$  symmetry if the Jahn-Teller distortion of the free radical is lifted. In these cases, the perpendicular configuration may be at least locally stable, as we found for on-top site on Ni(111) and for both hollows on the surfaces of all three metals. Only for adsorption in a bridge site, the threefold symmetry is broken already in the ideal starting geometry and in all cases we find that the relaxation leads immediately to the stable adsorption geometry consisting of a tilted molecule with the S atom bound to fcc hollow (Ni) or in a position between bridge and hollow (Pd and Pt).

On Ni(111), the stable adsorption site is in the center of an fcc hollow, with the C-S axis tilted by  $32^\circ$  with respect to the surface normal. A perpendicular position of the molecule allows for a slightly shorter distance of the S atom from the surface, but is  $0.07$  eV/molecule higher in energy.

Table 5.11: Adsorption energy and geometry of  $CH_3S$  on Ni, Pd and Pt.

Starting conf.	top	bridge	fcc-hollow	hcp-hollow
<b>Nickel (perpendicular)</b>				
Ads. site <sup>a</sup>	t/-/-	<b>h/b/u</b>	h/p/-	h/p/-
$E_{ads}$ [eV]	-1.35	<b>-2.77</b>	-2.70	-2.68
M-S [ $\text{\AA}$ ]	3.18 2.12 3.17	2.34 2.18 2.18	2.16 2.16 2.16	2.17 2.17 2.17
M-S <sup>a</sup> [ $\text{\AA}$ ]	2.03	1.69	1.58	1.60
C-S [ $\text{\AA}$ ]	1.84	1.85	1.85	1.85
Tilt <sup>b</sup> [ $^\circ$ ]	89.3	58.2	89.8	89.3
<b>Nickel (tilted)</b>				
Ads. site <sup>a</sup>	h/t/d	h/t/u	<b>h/t/u</b>	h/t/d
$E_{ads}$ [eV]	-2.02	-2.75	<b>-2.77</b>	-2.71
M-S [ $\text{\AA}$ ]	2.18 2.18 2.18	2.20 2.21 2.26	2.21 2.21 2.21	2.22 2.22 2.20
M-S <sup>a</sup> [ $\text{\AA}$ ]	1.63	1.68	1.67	1.67
C-S [ $\text{\AA}$ ]	1.86	1.86	1.86	1.86
Tilt <sup>b</sup> [ $^\circ$ ]	56.3	54.9	55.2	57.3
<b>Palladium (perpendicular)</b>				
Ads. site <sup>a</sup>	h/t/d	<b>h/b/d</b>	h/p/-	h/p/-
$E_{ads}$ [eV]	-2.59	<b>-2.72</b>	-2.62	-2.53
M-S [ $\text{\AA}$ ]	2.35 2.33 2.35	2.61 2.30 2.30	2.27 2.27 2.27	2.29 2.29 2.29
M-S <sup>a</sup> [ $\text{\AA}$ ]	1.69	1.74	1.51	1.59
C-S [ $\text{\AA}$ ]	1.87	1.85	1.84	1.85
Tilt <sup>b</sup> [ $^\circ$ ]	52.9	48.7	89.9	89.3
<b>Palladium (tilted)</b>				
Ads. site <sup>a</sup>	h/t/d	<b>h/b/d</b>	h/t/u	h/t/d
$E_{ads}$ [eV]	-2.60	<b>-2.73</b>	-2.67	-2.60
M-S [ $\text{\AA}$ ]	2.35 2.33 2.35	2.70 2.30 2.30	2.34 2.35 2.33	2.35 2.35 2.33
M-S <sup>a</sup> [ $\text{\AA}$ ]	1.69	1.78	1.66	1.69
C-S [ $\text{\AA}$ ]	1.87	1.85	1.86	1.87
Tilt <sup>b</sup> [ $^\circ$ ]	52.9	46.0	53.0	52.4
<b>Platinum (perpendicular)</b>				
Ads. site <sup>a</sup>	b/h/u	<b>b/h/d</b>	h/p/-	h/p/-
$E_{ads}$ [eV]	-2.70	<b>-2.73</b>	-2.50	-2.28
M-S [ $\text{\AA}$ ]	3.07 2.32 2.32	2.96 2.32 2.32	2.27 2.27 2.27	2.31 2.31 2.31
M-S <sup>a</sup> [ $\text{\AA}$ ]	1.90	1.86	1.45	1.60
C-S [ $\text{\AA}$ ]	1.84	1.84	1.84	1.86
Tilt <sup>b</sup> [ $^\circ$ ]	36.2	41.1	89.9	89.2
<b>Platinum (tilted)</b>				
Ads. site <sup>a</sup>	b/h/d	<b>b/h/d</b>	h/t/u	h/t/d
$E_{ads}$ [eV]	-2.73	<b>-2.78</b>	-2.48	-2.37
M-S [ $\text{\AA}$ ]	2.32 2.32 2.97	2.96 2.32 2.32	2.38 2.34 2.38	2.42 2.43 2.34
M-S <sup>a</sup> [ $\text{\AA}$ ]	1.86	1.86	1.67	1.75
C-S [ $\text{\AA}$ ]	1.84	1.84	1.87	1.88
Tilt <sup>b</sup> [ $^\circ$ ]	41.0	40.8	55.2	53.5

<sup>a</sup> Adsorption site look: nearest site position (**hollow-bridge-top**) / -CH<sub>3</sub> fragment tilt (**hollow-bridge-top**) / C-H bond tilt (**up-down**); <sup>b</sup> Tilting of the C-S bond axis w.r.t. metal surface plane.

A location in an hcp hollow is disfavored by 0.06 eV for a tilted and 0.02 eV for a perpendicular geometry. A relaxation starting from a bridge position (upright or tilted) leads to the same final state, except for a slightly off-symmetry location of the S atom. This minor difference could only be eliminated by using a very strict criterion for the residual forces.

On Pd(111), an initial configuration with an upright molecule in a hollow is conserved upon relaxation, but disfavored by 0.11 eV/molecule and 0.20 eV/molecule for the fcc and hcp hollows, respectively. The most stable configuration is reached from an initial state with a perpendicular or tilted molecule in a bridge position. In the final relaxed configuration the S-atom is located about halfway between bridge and fcc hollow, the C-S axis is tilted by  $44^\circ$  from the surface normal across the bridge position towards a Pd atom. Relaxations starting from either on-top or hollow positions relax to a state with the S atom almost in the center of a hollow, but as the direction of the tilt is towards a nearest-neighbor Pd atom, the tilt angle decreases. These configurations are higher in energy by 0.06 to 0.14 eV/molecule.

On a Pt(111) surface the stable geometry of the adsorbate is similar to that on Pd(111), but with a larger tilt angle. Relaxation starting from bridge site leads to a configuration with a S atom even slightly more displaced from the center of the fcc hollow and a larger normal-related tilt angle of  $49^\circ$ . In this case, a configuration very close to the absolute minimum can also be reached starting from an on-top site. Small variations in the displacement from the center, of the height of the S molecule above the surface, and of the tilt angle result in only modest variations of the potential energy (an increased height allows for a larger tilt angle, larger displacement from the hollow leads to increased height etc.).

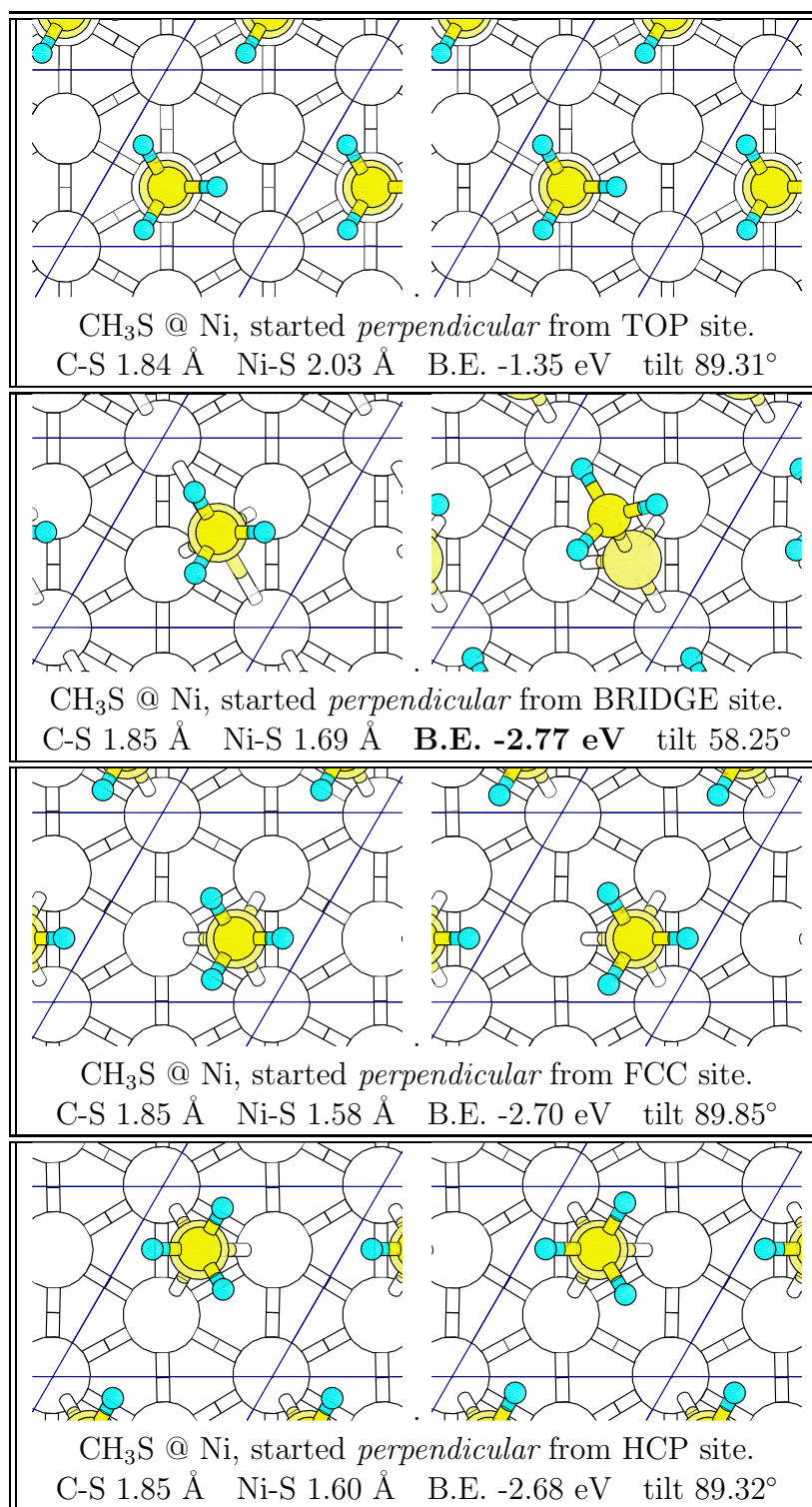
The strong chemisorptive bond between adsorbate and substrate leads also to a modification of the substrate geometry (interlayer spacings are not listed). On Ni(111), this effect is confined to a reduced inward relaxation of the top layers, but on Pd(111) and Pt(111), the  $\text{CH}_3\text{S}$  layer induces an outward relaxation of the top layer. On Pd the outward relaxation even extends to the second interlayer spacing. The intramolecular distances are only slightly affected, only the C-S distance is stretched from 1.79 Å to 1.85 Å on Ni and Pd and to 1.84 Å on Pt.

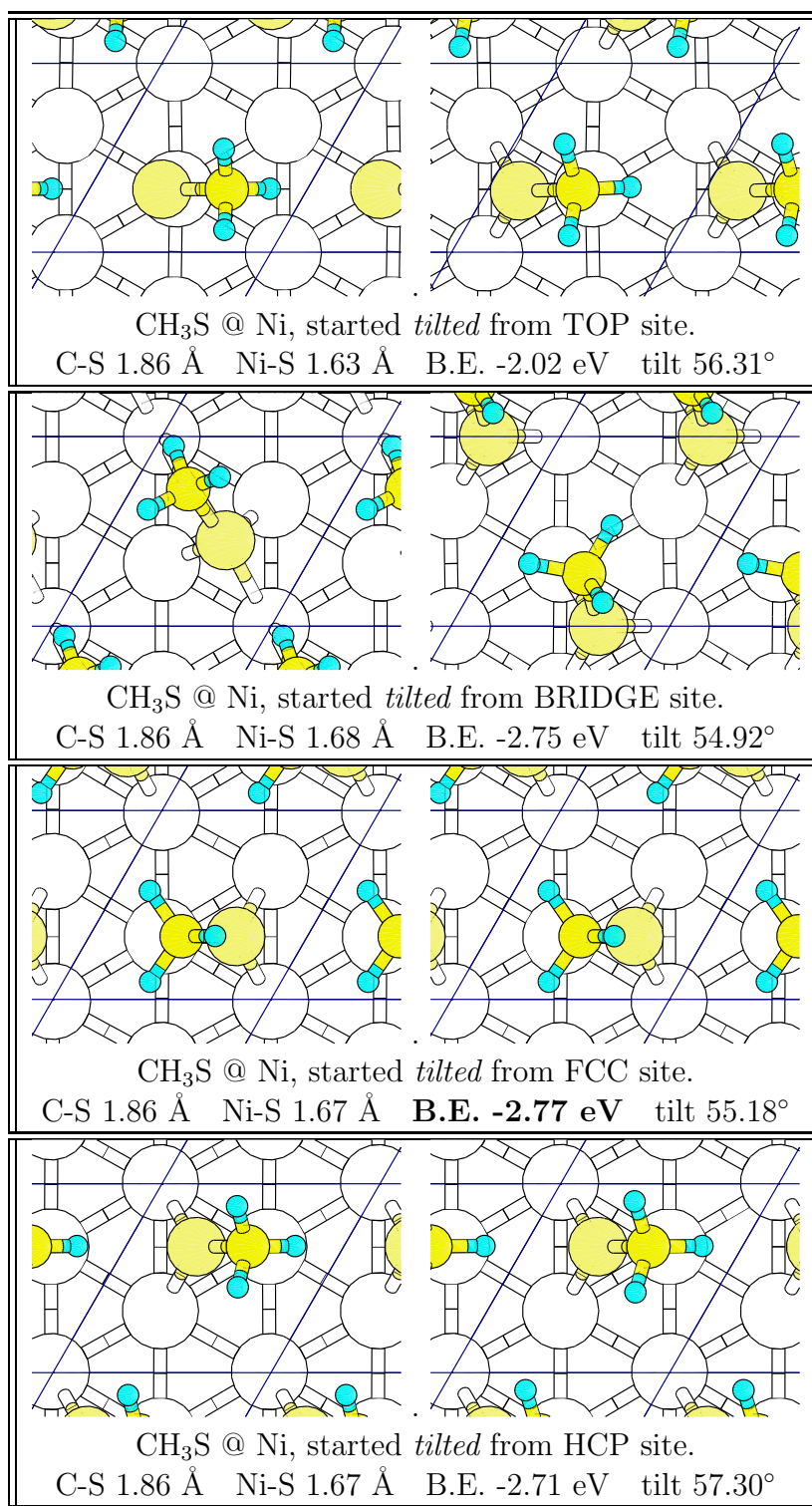
Detailed information on the adsorption geometry is available only in the work of Ghiringhelli et al. [159], Jiao et al. [158] seem to have considered only upright molecules located in an fcc hollow. Ghiringhelli et al. report an upright adsorption at a coverage of  $\Theta = 1/3$  not only on Pt, but also on Ag and Au. At a coverage of  $\Theta = 1/4$ , very modest tilt angles of  $9.3^\circ$  to  $11.7^\circ$  (w.r.t. surface normal) are reported for the equilibrium geometries of  $\text{CH}_3\text{S}$  adsorbed on the surfaces of Ni, Pd, Pt and Ag, only on a Au(111) surface larger tilt angle has been reported.

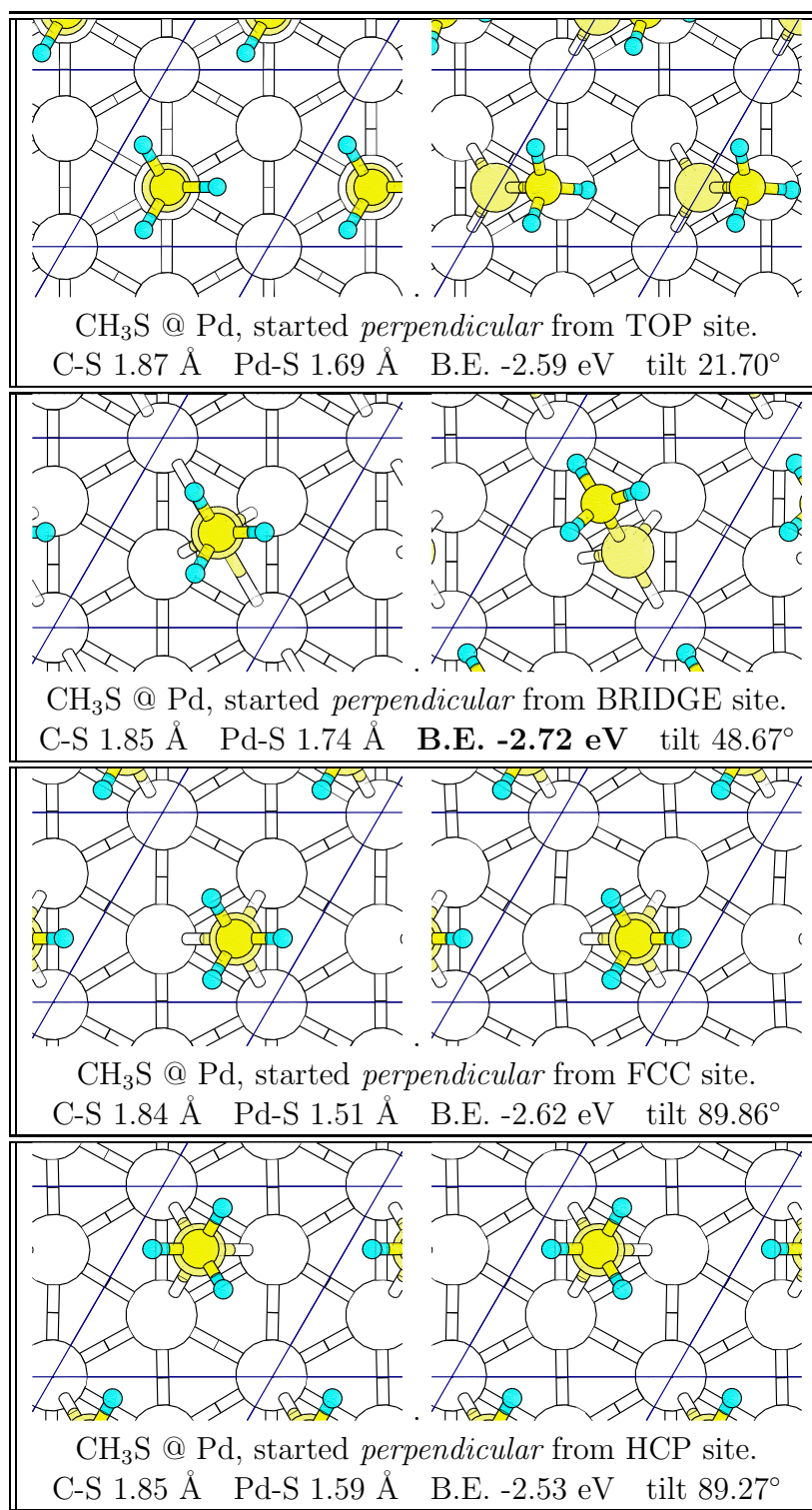
This striking contrast to our results evidently asks for an explanation. We have already mentioned that for Ag(111) and Au(111) surfaces the results of Ghiringhelli et al. are also at variance with a number of other studies (although there are also reports favoring an upright geometry). A very detailed investigation of the variation of the adsorption energy of CH<sub>3</sub>S on Au(111) with the angle of the C-S tilt and with the exact position of the S atom has been presented by Yourdshahyan and Rappe [161]. If the position of the S atom is fixed in an fcc hollow, the variation of the energy with the tilt angle shows 3 minima of increasing depth at about 5°, 15° and 34°, separated by barriers of about 0.05 eV. Their 2D potential-energy surface as a function of the angle and the displacement of the S atom along a straight line from top to fcc-, bridge and hcp hollow also shows multiple minima. In the high-coverage limit the deepest minimum corresponds to a position between bridge and fcc-hollow and a strong tilt of 43.2°. A C-S bond tilted by ~50° relative to the surface normal resulting from ab-initio DFT calculations has also been reported by Maksymovych et al. [162], who also calculated contrast images for scanned tunneling microscopy (STM). Best agreement with the experimental STM images was found for a bridge-adsorbed CH<sub>3</sub>S species (slightly displaced towards the hollow site) and a tilt angle of about 50° from the surface normal.

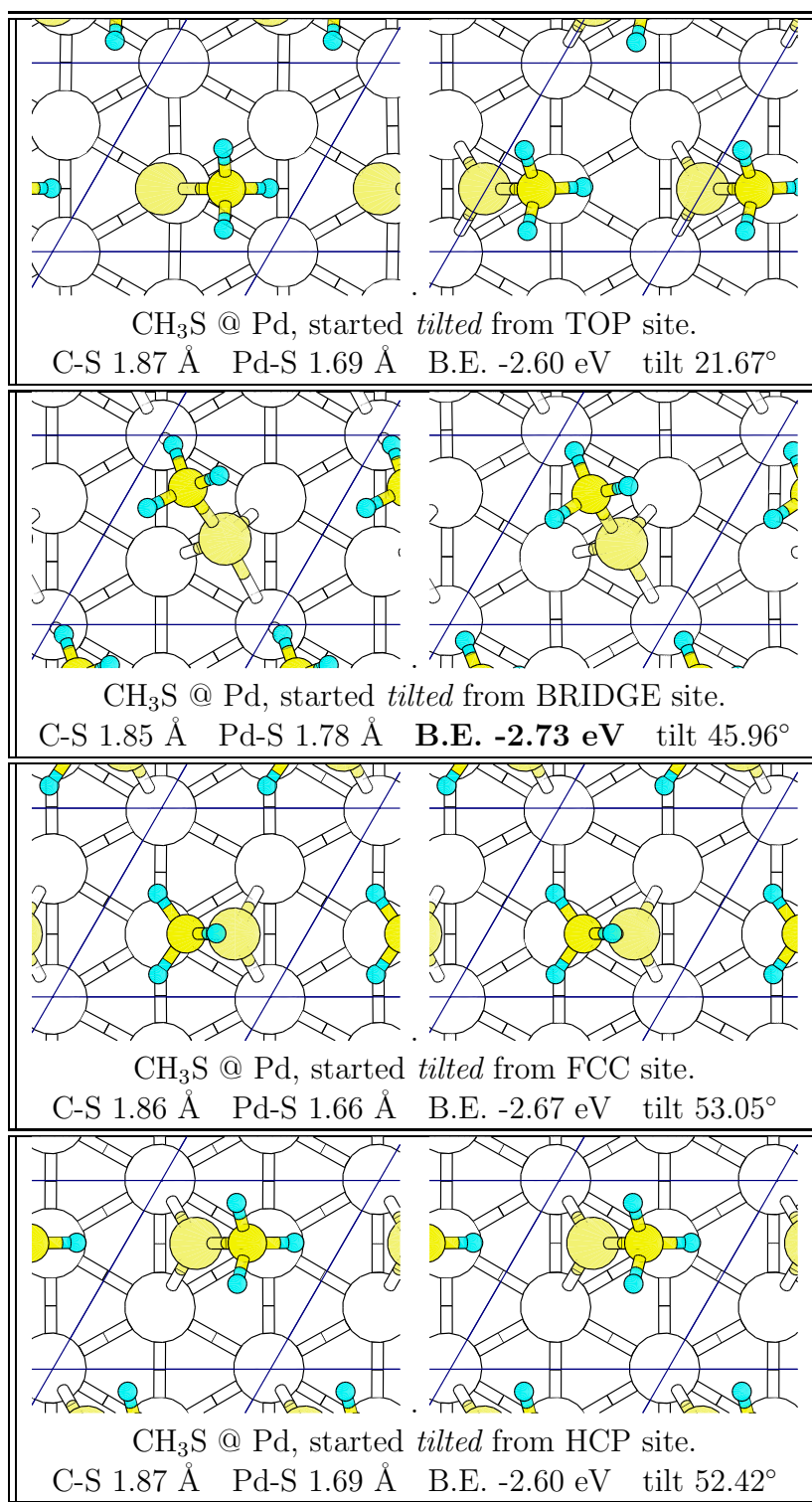
The result of Ghiringhelli et al. for this coverage corresponds to a local minimum completely upright at the fcc hollow. Our results confirm the existence of such a local minimum also for adsorption on a Pt(111) surface. For this metastable configuration, the height of the S atom above the surface (1.52 Å) and the S-metal distances (2.30 Å) reported by Ghiringhelli et al. balance with our results (Table 5.11). Hence there is evidence that the upright adsorption geometries for methane-thiolate on the Ni-group metals reported by these authors and by Jiao et al. [158] represent only local energy minima.

Our predicted adsorption geometries also agree favorably with experiment. For CH<sub>3</sub>S/Ni(111) we even find quantitative agreement with the experimental values of Mullins et al. [101] for the S-Ni distance of 2.20±0.2 Å (2.21 Å), the surface normal-related tilt angle of ~35° (34.8°) and the C-S bond-length of 1.85±0.02 Å (1.86 Å) (theoretical results in parentheses). The value for the S-Ni distance is also in good agreement with the value of 2.25±0.04 Å measured by Fernandez et al. [163] using EXAFS. For CH<sub>3</sub>S/Pt(111) Koestner et al. [106] estimated a tilt angle of about 45° from combined EXAFS and HREELS studies, to be compared with our prediction of 49°. Lee et al. [111] discussed interpretations of their NIXSW data in terms of different adsorbate geometries and concluded that CH<sub>3</sub>S is adsorbed in a tilted "off-top" position with Pt-S distances in the range between 2.3 and 2.4 Å, in good agreement with our calculated Pt-S distances of 2.32 Å.

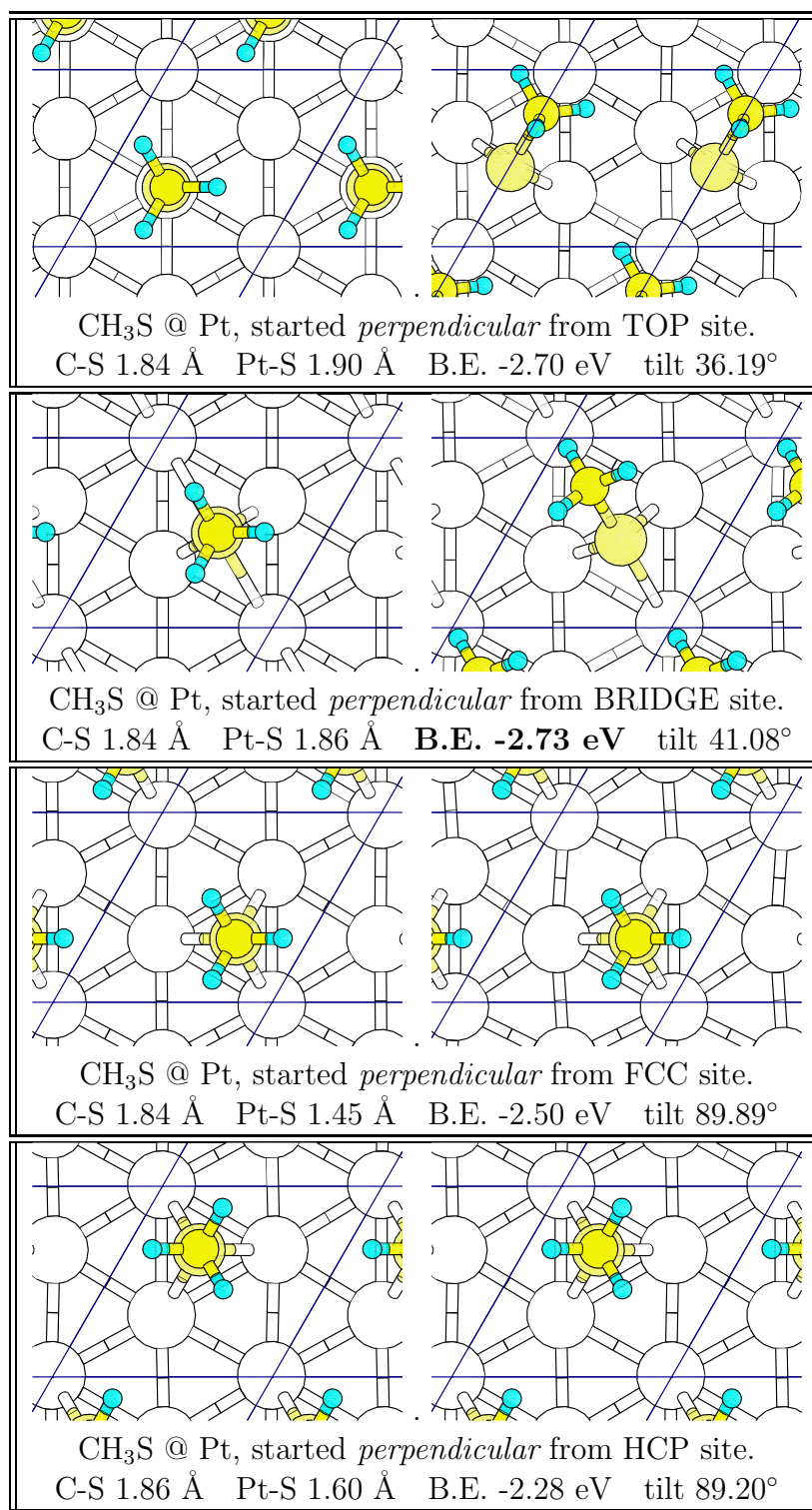
Figure 5.30: Adsorption geometries of CH<sub>3</sub>S on Ni(111), started perpendicular.

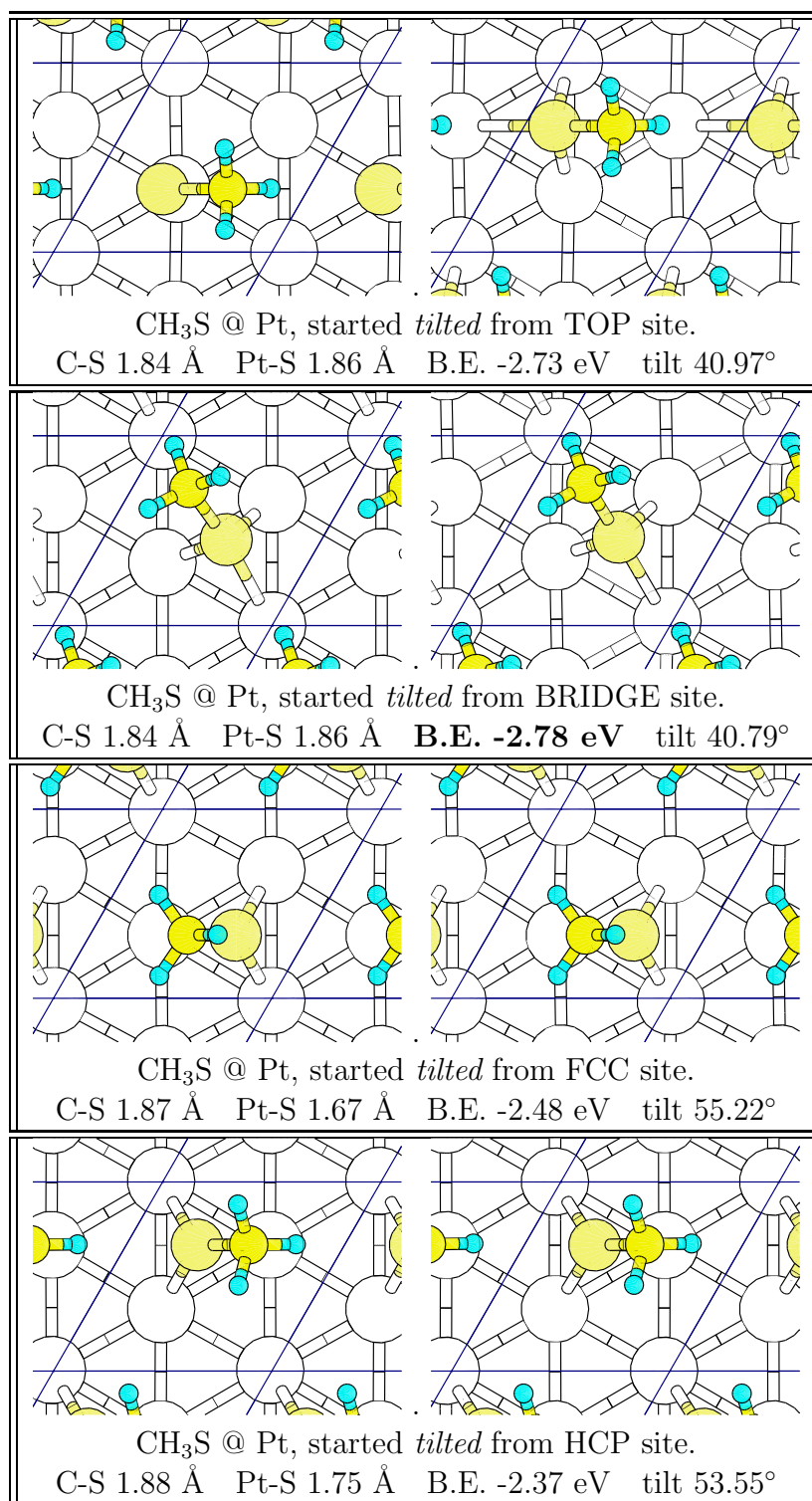
Figure 5.31: Adsorption geometries of CH<sub>3</sub>S on Ni(111), started tilted.

Figure 5.32: Adsorption geometries of CH<sub>3</sub>S on Pd(111), started perpendicular.

Figure 5.33: Adsorption geometries of CH<sub>3</sub>S on Pd(111), started tilted.



Figure 5.34: Adsorption geometries of CH<sub>3</sub>S on Pt(111), started perpendicular.

Figure 5.35: Adsorption geometries of CH<sub>3</sub>S on Pt(111), started tilted.

## 5.6.2 Electronic Properties

The stability of the low-symmetry adsorption complexes of methane-thiolate requires some information. Figs. 5.36, 5.37 and 5.38 shows the local electronic DOS for the topmost metal surface layer and on the S atom, for the stable configuration of CH<sub>3</sub>S on Ni, Pd and Pt (111) surfaces, respectively.

Compared to a thiol-covered surface, we note only small changes around the Fermi level, as also reflected in the work functions which are even slightly enhanced for the thiolate covered surfaces compared to those with thiol monolayers (by 0.02/0.04/0.06 eV on Ni/Pd/Pt surfaces).

Significant changes are found at higher binding energies. The HOMO, HOMO-1 and HOMO-2 states of the radical fall within the energy range covered by the *d*-band of the substrate. All three S-*p* states hybridize strongly with *d*-states of the substrate, producing a strong bonding/anti-bonding splitting leading to a shift of all molecular eigenstates by about 2 eV to larger binding energies.

The HOMO-2 state composed by bonding states located on the methyl group is located at the lower edge of the metal-*d* band, it also undergoes a weak interaction with the metal *d*-states leading to a polarization of the electron distribution in the methyl group. This effect increases in the sequence Ni–Pd–Pt, following the increased width of the *d*-band.

The strong covalent interaction between adsorbate and substrate, however, is entirely dominated by the S-*p*–metal-*d* interaction: Donation of electrons from the occupied *pp*<sub>σ</sub> state (HOMO-1) to the metal *d*-band (leading a weaker C-S bond) and back-donation to the partially occupied S-*p*<sub>π</sub> states (HOMO). The degeneracy of the S-*p*<sub>π</sub> states perpendicular to the C-S axis is broken, and the S-*p* states parallel to the surface and perpendicular to the tilted C-S axis interact with the substrate in a different way.

### Difference Charge Densities

The formation of new bonds between an adsorptive and a clean surface has its origin in displacement of electron density between the interacting systems, so that they become to overlap. Fortunately, there is a tool to visualize this shift of electron density. Namely, calculation of *difference of the charge density* helps to explain charge transfer and bonding characteristics.

The **charge density difference (CDD)** of an adsorbate-metal system may be

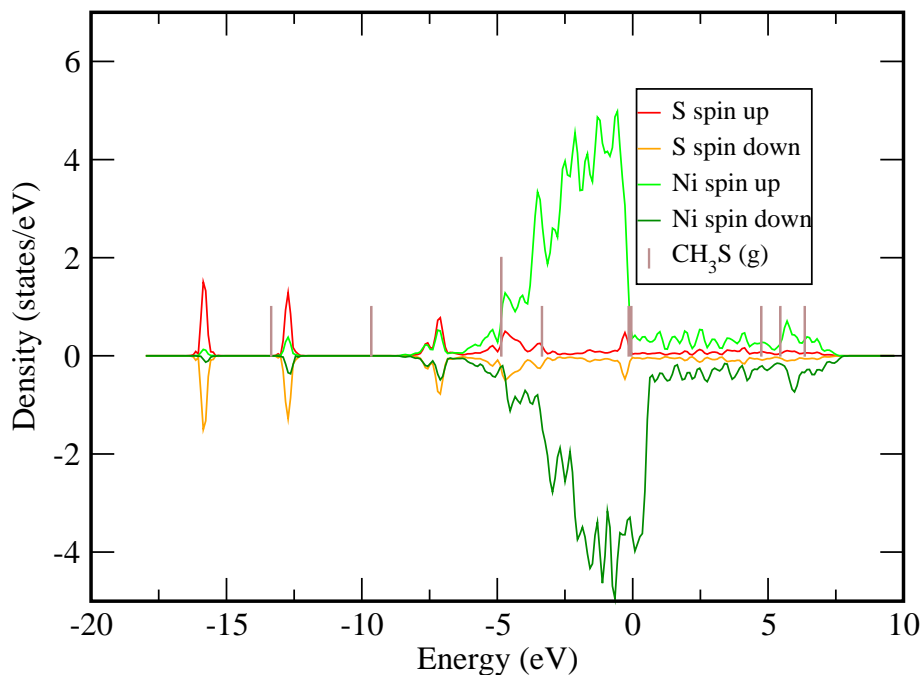


Figure 5.36: *PDOS diagram of  $\text{CH}_3\text{S}$  @  $\text{Ni}(111)$ .*

evaluated by numerical subtraction of the charge densities (**CD**) of a bare adsorbate and bare metal (both calculated at fixed coordinates as they are in the adsorbed system) from the charge density of the entire adsorbate-metal structure:

$$\text{CDD} = \text{CD}_{\text{Adsorbate/Metal}} - (\text{CD}_{\text{Adsorbate}} + \text{CD}_{\text{Metal}}). \quad (5.18)$$

This relation is apparently similar definition as for the adsorption energy,  $E_{\text{ads}}$ , and, in fact, it also provides the complementary information, where the electrons are spatially re-distributed upon adsorption.

The plots of charge density differences in systems of  $\text{CH}_3\text{S}$  adsorbed on Ni, Pd and Pt are shown in Figs. 5.39, 5.40 and 5.41, respectively. There is always a front view and a side view, which is actually related to the viewpoint of the sulphur atom and the direction of the attached tilted  $-\text{CH}_3$  group.

When analysing the charge density, we plotted isosurfaces corresponding to one positive isovalue ( $+0.02$  eV, violet surface) and one negative isovalue ( $-0.02$  eV, light blue surface) in order to determine the regions where the charge density increased (“+”) and where it was reduced (“-”), respectively.

For the methane-thiolate adsorbed in a hollow on  $\text{Ni}(111)$ , we find that electron

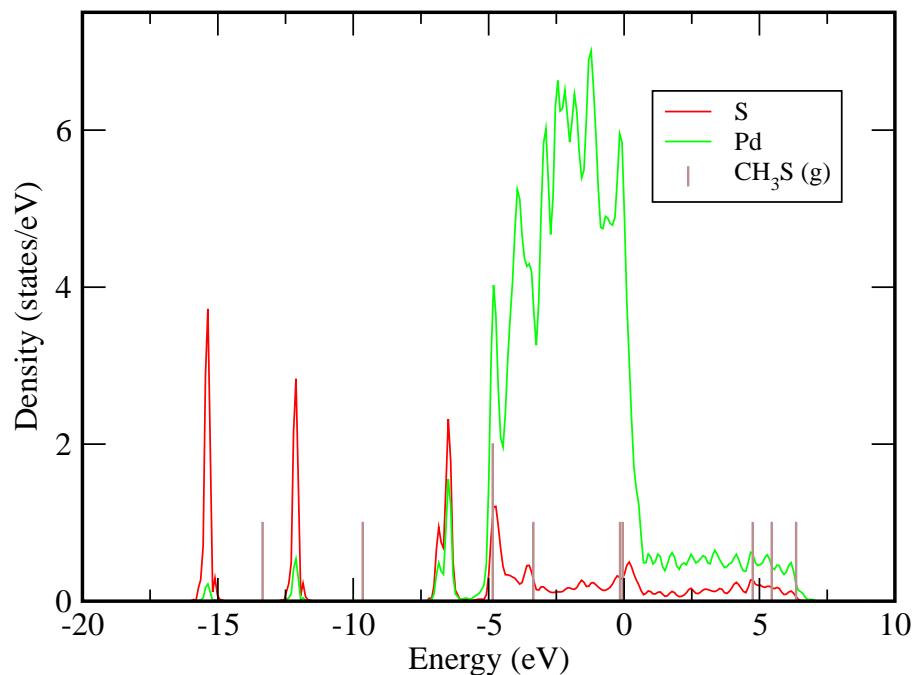


Figure 5.37: *PDOS diagram of  $\text{CH}_3\text{S}$  @  $\text{Pd}(111)$ .*

density is withdrawn from the  $\text{S-}p_\sigma$  states extending along the C-S axis (hence weakening the C-S  $pp_\sigma$  bond) and from the  $\text{S-}p_\pi$  states extending parallel to the surface. The electron density is increased in the bonding regions between the S-atoms and all three Ni atoms surrounding the hollow. Regions of electron accumulation and electron depletion are found also around the Ni atoms, suggesting that adsorbate-substrate bonding is based on a re-hybridization of both Ni and S orbitals and involves no substantial electron transfer. The electron density on the methyl group is not affected by the adsorption.

For adsorption close to a bridge position on Pt(111) the picture looks rather different: now only the two Pt atoms forming the bridge are involved in the covalent bonds with the S atoms. On these Pt atoms, the re-hybridization affects mostly the  $d_{z^2}$  states extending perpendicular to the surface which are strongly polarized towards the atoms. On the S atom, bonding involves mostly the p-states perpendicular to the C-S axis. In contrast to Ni, we find that adsorption on Pt also leads to a weak electronic polarization of the methyl group.

Given the rather small energy differences, it is difficult to assess the reasons why on the heavier metals the less symmetric sites with a lower metal coordination are the preferred adsorption sites. Evidently tilt angle and adsorption site are cor-

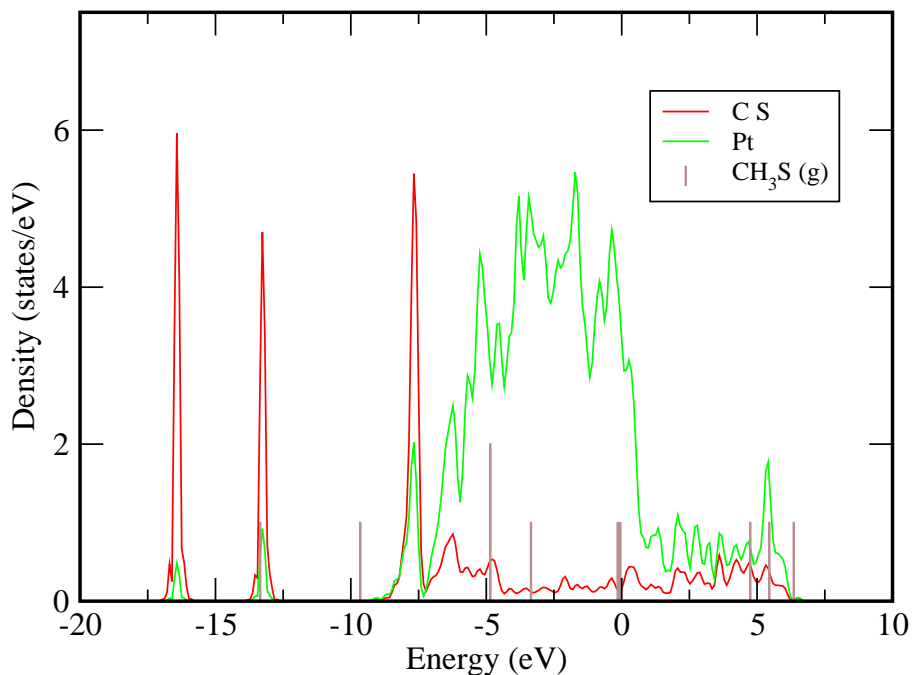


Figure 5.38: *PDOS diagram of  $\text{CH}_3\text{S}$  @  $\text{Pt}(111)$ .*

related. For the formation of a tilted configuration at high coverage, also steric reasons (minimization of the Pauli repulsion between the methyl groups) have been invoked. [164, 161]. Here we find that the adsorption-induced polarization of the methyl group could also play a role. The small positive charge on the methyl group in Fig. 5.41 is oriented towards the negative charge created by the depletion of the  $\text{pp}\sigma$  states around the S atom. This interaction stabilizes configurations displaced towards the bridge site and more strongly tilted away from the surface normal.

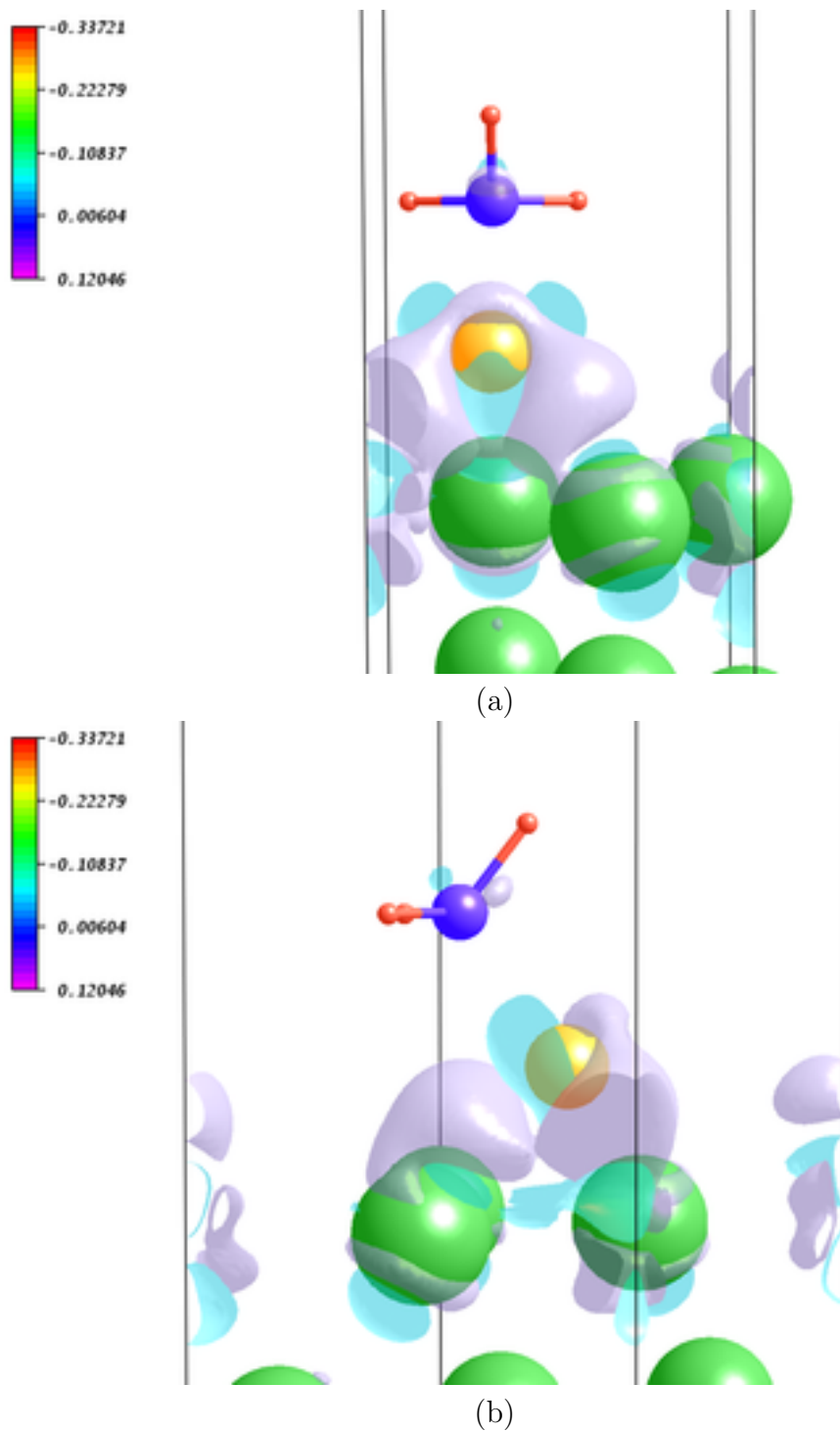


Figure 5.39: Charge density difference (CDD) isosurface plot of  $\text{CH}_3\text{S}$  @ Ni(111): a front view (a) and a side view (b).

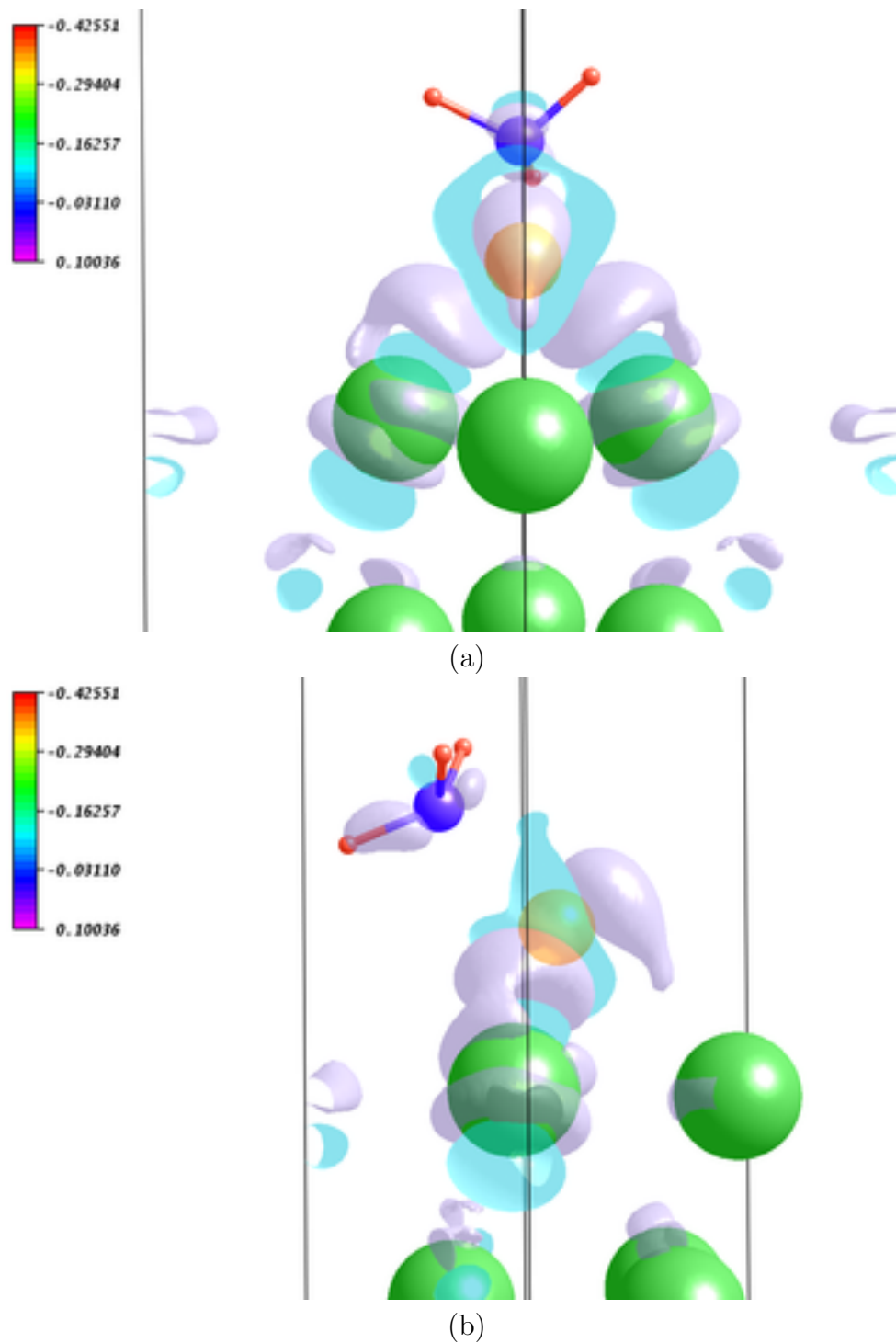


Figure 5.40: Charge density difference (CDD) isosurface plot of  $\text{CH}_3\text{S}$  @  $\text{Pd}(111)$ : a front view (a) and a side view (b).



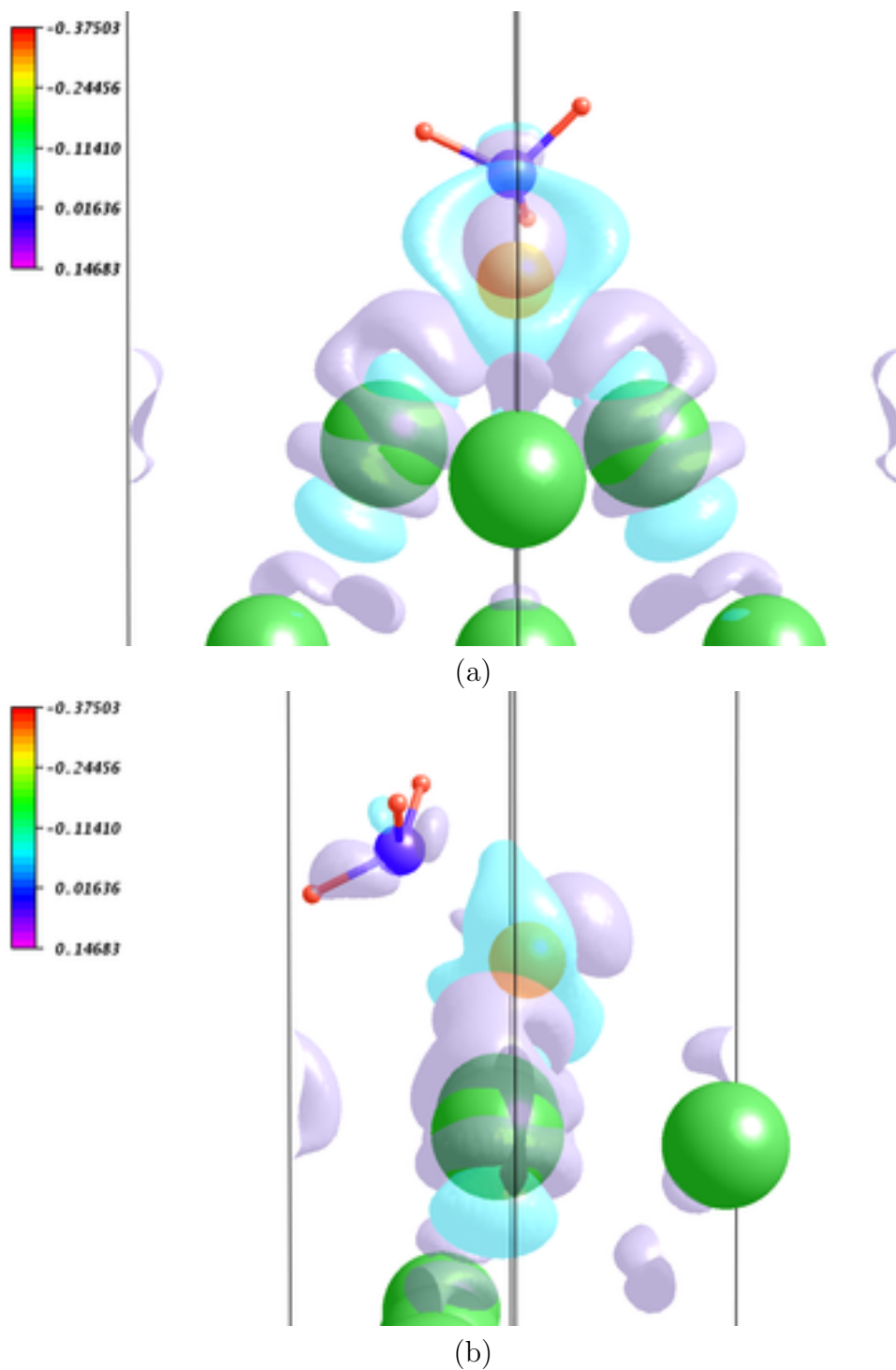


Figure 5.41: Charge density difference (CDD) isosurface plot of  $\text{CH}_3\text{S}$  @ Pt(111): a front view (a) and a side view (b).

### 5.6.3 Vibrational Analysis

The bonding of the  $\text{CH}_3\text{S}$  radical to the metal surfaces was further investigated by calculation of the vibrational (IR) spectra of the most stable configuration for each metal surface.

The calculated vibrational normal modes, calculated by means of FC and LR approaches, are summarized in Table 5.12. Only the the first 18 of altogether 24 modes are listed.

The corresponding eigenvectors are shown in Figs. 5.42 and 5.43 for adsorption on nickel, Figs. 5.44 and 5.45 for palladium, and Figs. 5.46 and 5.47 for platinum.

The three highest frequencies in each system belong to asymmetric and symmetric C-H stretching modes, followed by the three C-H deformation modes and two C-H rocking modes, and by the C-S stretching mode at around  $600\text{ cm}^{-1}$ . The eigenmodes in the range between about  $150$  and  $300\text{ cm}^{-1}$  consist of frustrated translation modes and deformation modes of the substrate layer compatible with the  $\sqrt{3} \times \sqrt{3}$  periodicity of the surface cell. The mode at  $175\text{ cm}^{-1}$  describes a pure torsion mode of the methyl group around the C-S axis of the thiolate. Quite generally it is evident that the modes describing a deformation of the substrate and frustrated translations of the substrate couple only weakly.

For a thiolate monolayer on Ni(111), all eigenmodes except the symmetric C-H deformation and the C-S stretching modes are blue-shifted compared to a gas-phase methane-thiolate radical, the symmetric C-H deformation mode is red-shifted by  $-44\text{ cm}^{-1}$ , the C-S stretching mode by  $-135\text{ cm}^{-1}$ . Compared to adsorbed methane-thiol shifts in the eigenfrequencies of the C-H modes are modest, only one of the C-H rocking modes is red-shifted by  $-109(-107)\text{ cm}^{-1}$ , while C-S stretching and the metal-S stretching modes are blue-shifted mode by  $+45(+79)\text{ cm}^{-1}$  and  $+31(+22)\text{ cm}^{-1}$  in calculations using the FC(LR) method.

The differences between the two C-H stretching, the symmetric C-H deformation and the C-H rocking modes are smaller than for adsorbed thiol, expressing the fact that the symmetry of the adsorbed thiolate is closer to  $C_s$  than that of the adsorbed thiol. The difference between the symmetric and asymmetric deformation modes remains important, as expected for the tilted adsorption configurations. The blue-shift of the C-S and metal-S mode reflects the fact that both the C-S and the S-substrate bonds are stronger than in the adsorbed methane-thiol layer. Agreement with the HREELS experiment [100, 102] is reasonably good, although there are differences of up to  $25\text{ cm}^{-1}$  in the frequencies listed in the two papers.

Table 5.12: Normal vibration modes for the most stable configurations of  $CH_3S$  on Ni, Pd and Pt (111)-surfaces. <sup>a</sup> Ref. [102], <sup>b</sup> Ref. [107].

# Mode description	Nickel $\tilde{\nu}_{Ni}^{ads}$ [ $cm^{-1}$ ]			Palladium $\tilde{\nu}_{Pd}^{ads}$ [ $cm^{-1}$ ]			Platinum $\tilde{\nu}_{Pt}^{ads}$ [ $cm^{-1}$ ]			$\tilde{\nu}^{free}$ [ $cm^{-1}$ ]	
	FC	LR (int)	exp <sup>a</sup>	FC	LR (int)	exp	FC	LR (int)	exp <sup>b</sup>	LR (int)	
01 C-H stretch (as.)	3090	3089 (0.002)	2974	3079	3074 (0.005)	–	3077	3060 (0.008)	3010	3012 (0.235)	
02 C-H stretch (as.)	3077	3073 (0.001)	–	3066	3063 (0.001)	–	3064	2991 (0.007)	2985	3010 (0.289)	
03 C-H stretch (s.)	2969	2976 (0.004)	2915	2966	2962 (0.001)	–	2960	2906 (0.006)	2910	2938 (0.577)	
04 C-H def. (as.)	1402	1401 (0.019)	1410	1415	1416 (0.004)	–	1412	1411 (0.012)	1410	1374 (1.000)	
05 C-H def. (as.)	1400	1396 (0.000)	–	1400	1401 (0.000)	–	1395	1398 (0.003)	–	1369 (0.944)	
06 C-H def. (s.)	1241	1243 (0.000)	1269	1257	1260 (0.002)	–	1263	1268 (0.002)	1290	1280 (0.000)	
07 C-H rocking	878	889 (0.070)	922	881	888 (0.049)	–	897	913 (0.010)	975	848 (0.219)	
08 C-H rocking	863	868 (0.007)	–	877	881 (0.008)	–	891	894 (0.091)	–	847 (0.203)	
09 C-S stretch	597	598 (0.030)	642	608	599 (0.025)	–	637	631 (0.061)	670	727 (0.708)	
10 Ni-S/ Pd-S/ Pt-S	305	298 (0.053)	325	296	284 (1.000)	–	308	312 (1.000)	320	– –	
11	276	275 (0.131)	–	253	242 (0.058)	–	259	252 (0.552)	–	– –	
12	239	237 (0.831)	–	184	196 (0.075)	–	212	202 (0.014)	–	– –	
13	219	222 (0.216)	–	174	177 (0.173)	–	150	171 (0.018)	–	– –	
14	217	220 (0.208)	–	167	166 (0.045)	–	131	158 (0.003)	–	– –	
15	208	201 (0.220)	–	154	155 (0.327)	–	128	138 (0.412)	–	– –	
16	177	180 (1.000)	–	151	147 (0.010)	–	117	133 (0.418)	–	– –	
17	139	175 (0.005)	–	117	134 (0.159)	–	115	121 (0.419)	–	– –	
18	136	146 (0.266)	–	104	121 (0.061)	–	102	120 (0.086)	–	– –	

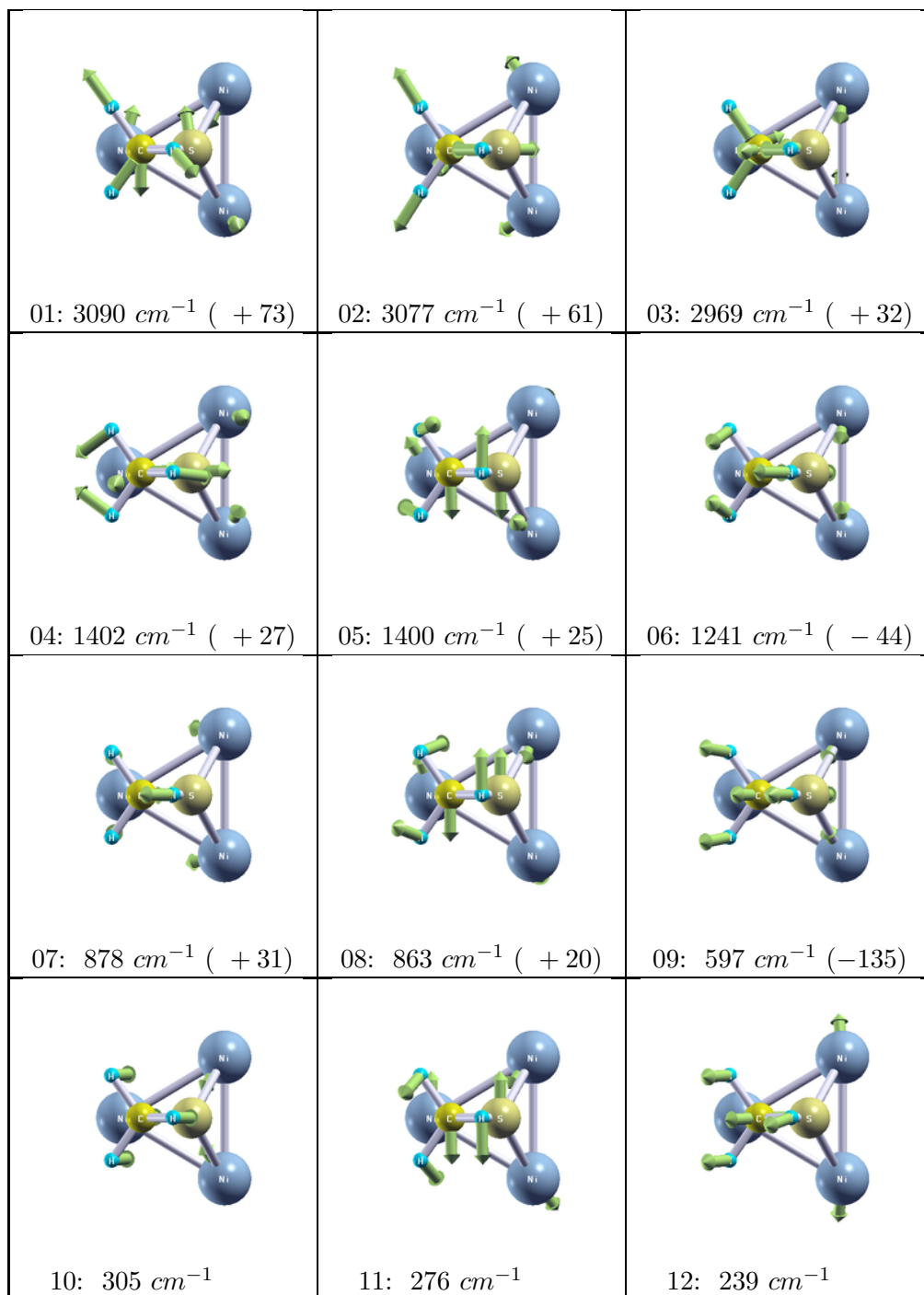
The C-H stretching frequencies are lower than predicted by our calculations, while harder metal-S and C-S stretching frequencies suggest a stronger bonding between the S atom and both the methyl group and the substrate.

For CH<sub>3</sub>S/Pt(111), the changes in the eigenfrequencies with respect to the gas-phase radical and to adsorbed methane-thiol are similar, although slightly smaller in both directions. Agreement with the HREELS experiments [106, 107] is good, the largest discrepancy of about 85 cm<sup>-1</sup> exists for the asymmetric C-H stretching modes, which are most subject to anharmonic corrections.

We also find good agreement between theory and experiment for the C-S and metal-S stretching modes. For methane-thiolate adsorbed on Pd(111) not experimental spectra are available, but most eigenmodes follow a smooth trend on the three different substrates.

We have also calculated the normal-mode intensities. Among the eigenmodes of the adsorbate, the highest intensities are predicted for the C-S stretch, the C-H rocking and the asymmetric C-H deformation modes.

Under the assumption that dipole scattering is the dominant mechanism, the predicted intensities should be at least roughly comparable with the experimental intensities observed in the HREELS experiments on methane-thiolate on Pt(111) [107]. As expected, a very high intensity is observed for the asymmetric C-H deformation mode at 1410 cm<sup>-1</sup> and the lower C-H rocking mode at 945 cm<sup>-1</sup>. On the other hand, the HREELS intensities for the C-H stretching modes are higher, those of the C-S mode lower than the calculated IR intensities.

Figure 5.42: Eigenvectors of  $\text{CH}_3\text{S}$  @  $\text{Ni}(111)$  IR normal modes.

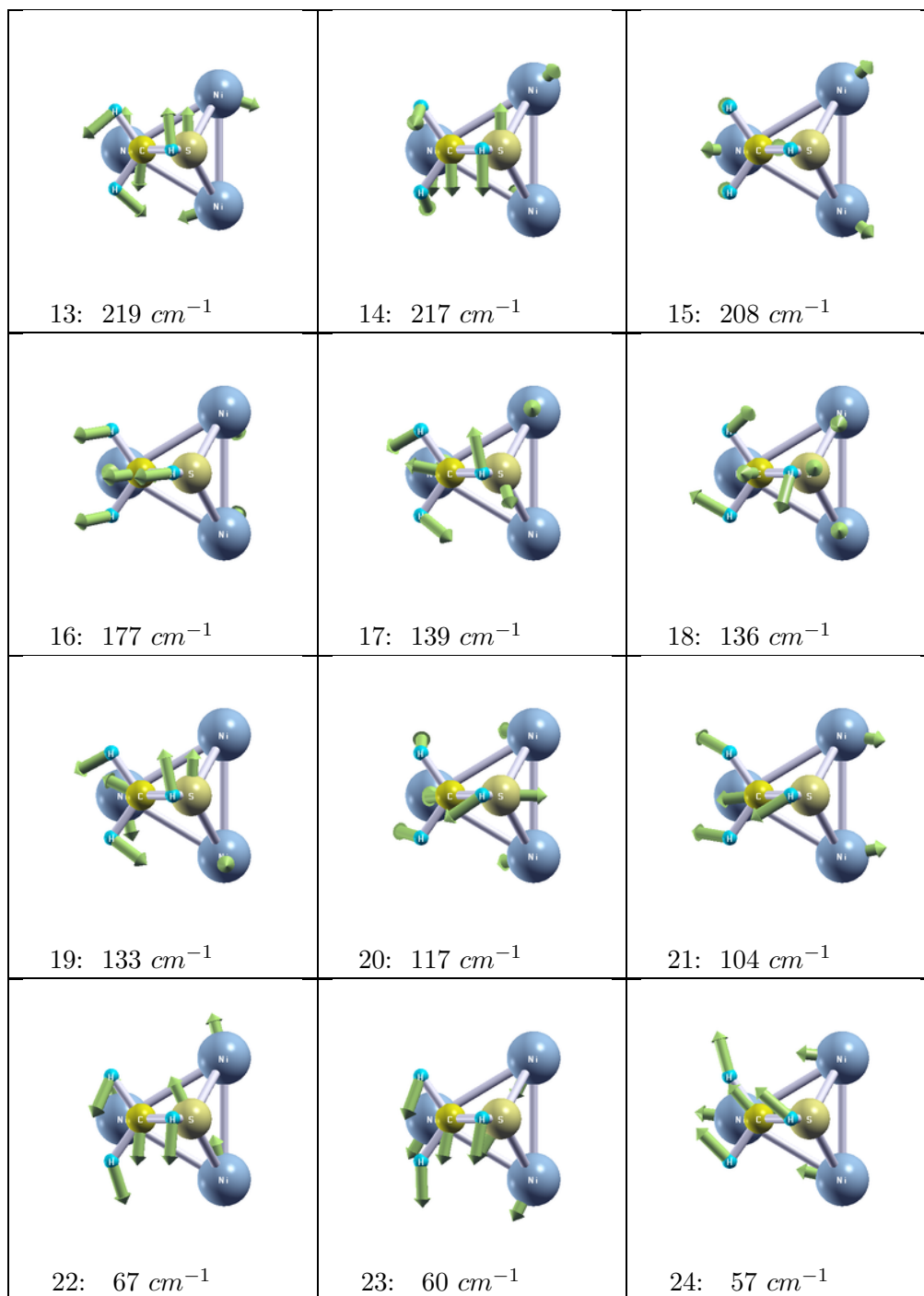
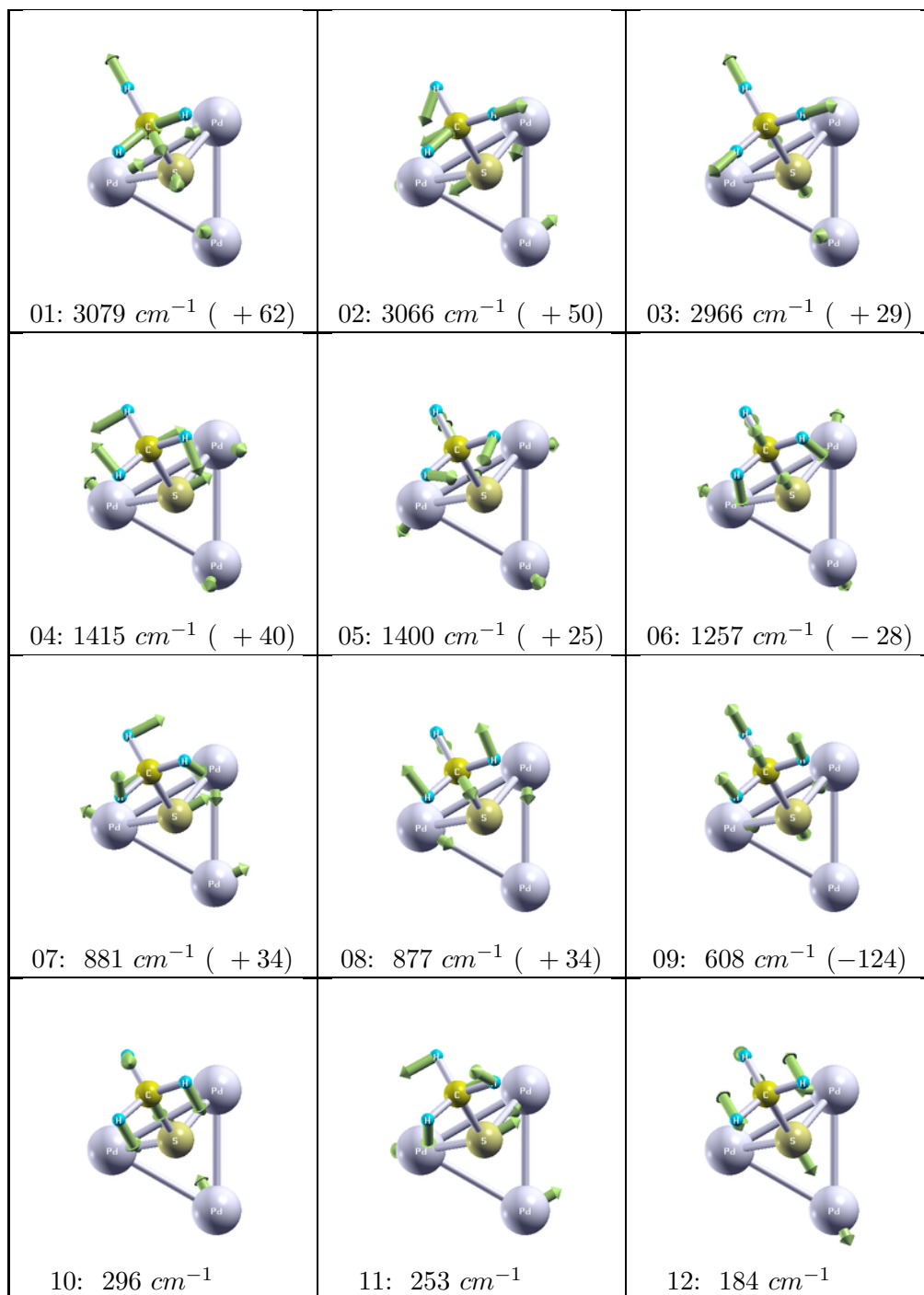


Figure 5.43: *Eigenvectors of  $\text{CH}_3\text{S}$  @  $\text{Ni}(111)$  IR normal modes (continued).*

Figure 5.44: Eigenvectors of  $\text{CH}_3\text{S}$  @  $\text{Pd}(111)$  IR normal modes.

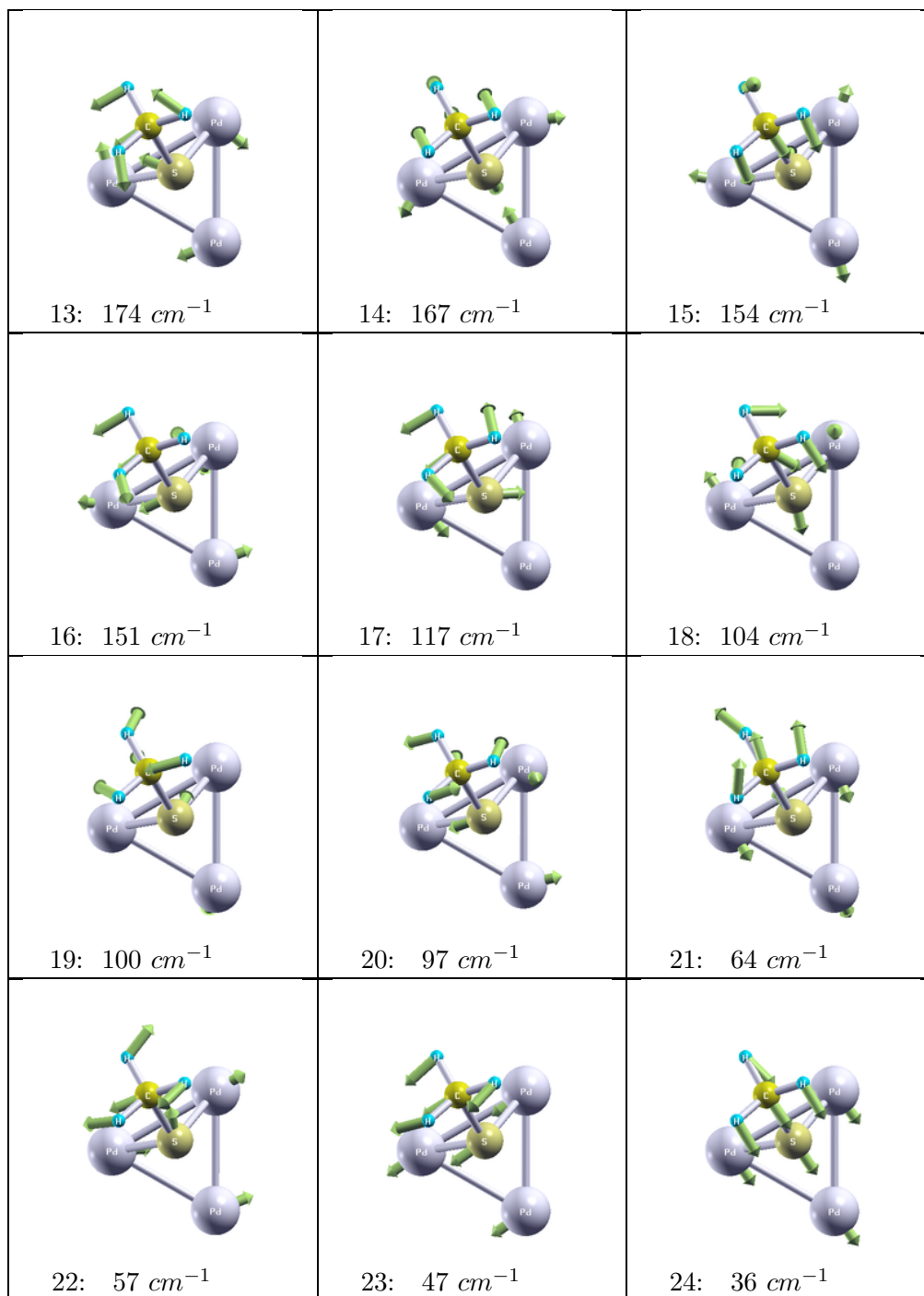
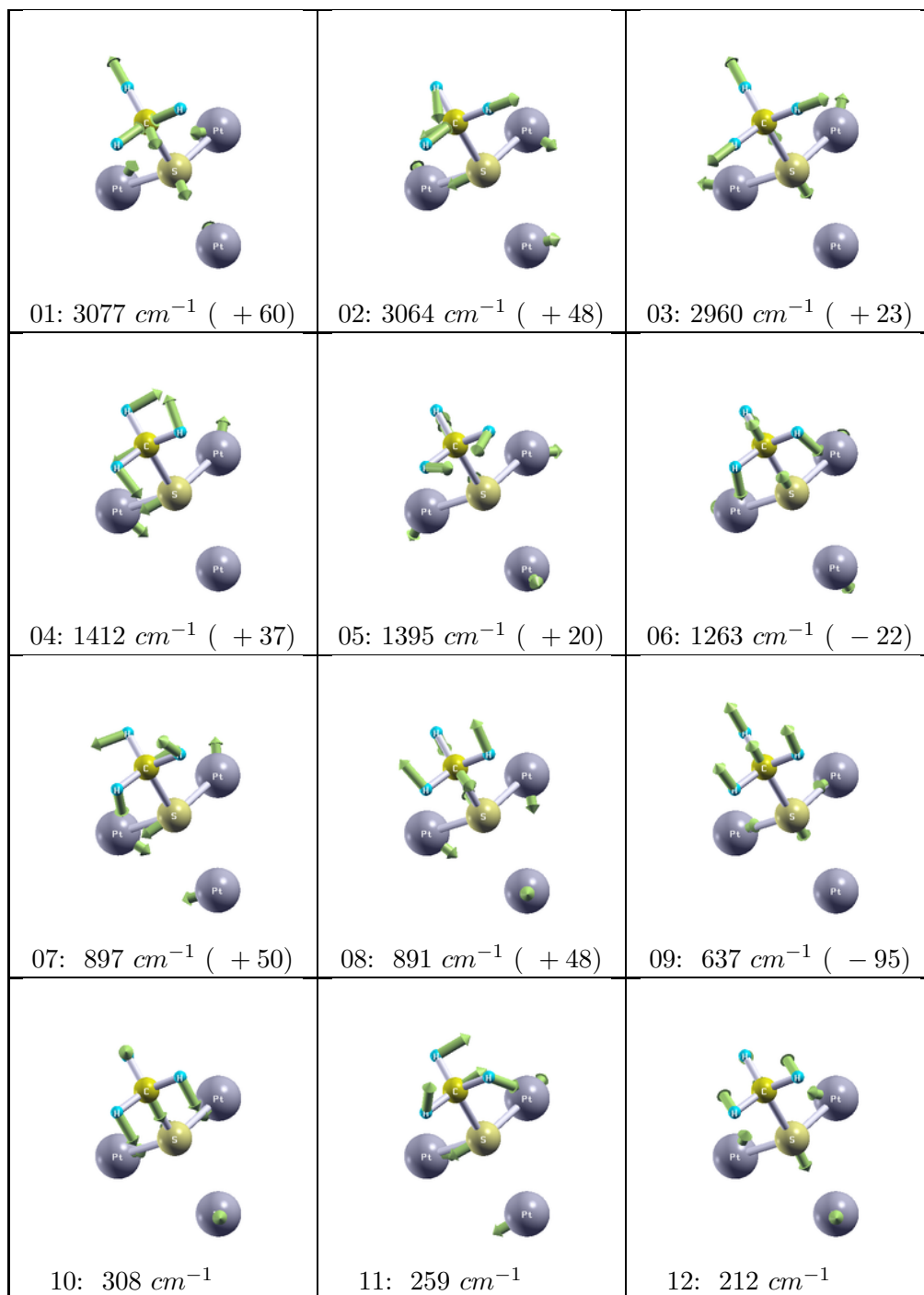


Figure 5.45: *Eigenvectors of  $\text{CH}_3\text{S}$  @  $\text{Pd}(111)$  IR normal modes (continued).*



Figure 5.46: Eigenvectors of  $\text{CH}_3\text{S}$  @  $\text{Pt}(111)$  IR normal modes.

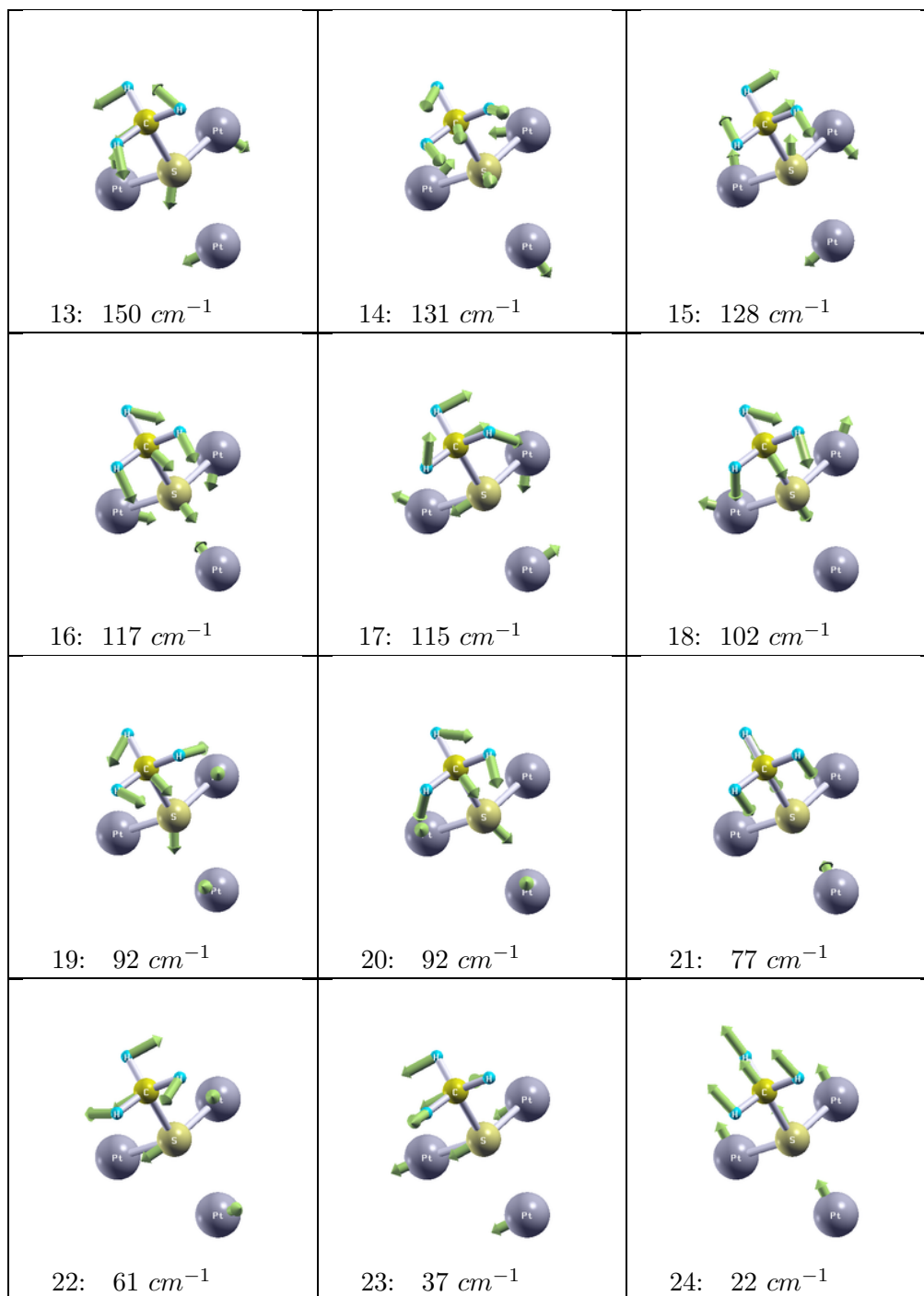


Figure 5.47: Eigenvectors of  $\text{CH}_3\text{S} @ \text{Pt}(111)$  IR normal modes (continued).

## 5.7 Comparison of Thiol and Thiolate Adsorption

In addition, a very brief summary of calculated differences between bond lengths and angles in the most stable configurations of methane thiol and methane thiolate on the studied metal surfaces is presented in Table 5.13.

Table 5.13: *Geometry parameters of CH<sub>3</sub>S and CH<sub>3</sub>SH adsorbed on Ni, Pd and Pt. M-S(⊥) stands for perpendicular distance of the S atom from the topmost surface layer, Δd<sub>12</sub>/Δd<sub>23</sub> are the relaxations of interlayer distances in % of the bulk interlayer distance.*

M	Property	Clean M	CH <sub>3</sub> SH/M	CH <sub>3</sub> S/M	CH <sub>3</sub> SH(g)	CH <sub>3</sub> S(g)
Ni	C-S [Å]	—	1.88	1.87	1.82	1.79
	S-H [Å]	—	1.37	—	1.35	—
	M-S(⊥) [Å]	—	1.95	1.67	—	—
	C-S-H [°]	—	92.4	—	97.0	—
	C-S tilt [°]	—	55.2	54.9	—	—
	Δd <sub>12</sub> /Δd <sub>23</sub>	-0.9/+0.2	-0.4/-0.4	-0.2/-0.3	—	—
Pd	C-S [Å]	—	1.86	1.85	“	“
	S-H [Å]	—	1.42	—	—	—
	M-S(⊥) [Å]	—	2.08	1.78	—	—
	C-S-H [°]	—	96.1	—	—	—
	C-S tilt [°]	—	47.3	46.0	—	—
	Δd <sub>12</sub> /Δd <sub>23</sub>	+0.1/-0.3	+1.2/0.0	+1.2/+0.5	—	—
Pt	C-S [Å]	—	1.82	1.84	“	“
	S-H [Å]	—	1.36	—	—	—
	M-S(⊥) [Å]	—	2.39	1.86	—	—
	C-S-H [°]	—	95.3	—	—	—
	C-S tilt [°]	—	29.8	40.8	—	—
	Δd <sub>12</sub> /Δd <sub>23</sub>	+0.2/-0.7	+1.4/-0.6	+1.8/-0.1	—	—

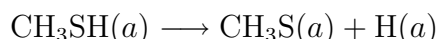
Apparently, the largest changes are to be found in the interatomic distances of the molecule/radical according to the present hybridization and overlap with *d*-band electrons of the substrate metal. The largest change of the tilting angle is observed for platinum, based on the peculiar on-top adsorption mode of thiol on thiol surface.

For further conclusions, see Chapter 6.

## 5.8 Dissociation of Methane Thiol on Metals

The dissociation of methane thiol ( $\text{CH}_3\text{SH}$ ) molecule on (111)-surfaces of Ni, Pd and Pt has been studied by the means of the improved dimer method [46]. This powerful method is useful for finding a transition state of surface reactions like we observe them on metals.

In Chapter 5.6, the optimal structure of  $\text{CH}_3\text{S}$  radical on the metallic surfaces were declared. Nevertheless, if we think of a surface dissociation reaction



we have to reveal how the surface looks like if both fragments are present, i.e. not only the methane thiolate radical ( $\text{CH}_3\text{S}$ ), but the atomic hydrogen as well. Hence the it was necessary to recalculate the results from Chapter 5.6 in the presence of co-adsorbed one surface hydrogen atom per unit cell. As it is known from various studies (e.g., Ref. [154]), atomic hydrogen prefers hollow-site adsorption.

Knowing this, we have added the quasi-dissociated hydrogen atom to the methane thiolate radical onto the metal surface to such hollow position, so that the sulfur-hydrogen distance is longer than 2 Å, as to ensure than the S-H bond (with gas-phase equilibrium distance of approx. 1.1 Å is completely broken. Such structures were relaxed with the same accuracy settings as used in Chapters 5.5 and 5.6.

In fact, the addition of hydrogen atom had in each case just a minor impact on the adsorption pattern of the adsorbed methane thiolate. Note that the remarkable structure differences are only visible for the perpendicular distance of sulfur and the surface of the metals, whereas the change of the tilt angle upon this co-adsorption was negligible for palladium and platinum, in the case of nickel, the change of approx. 4° towards the perpendicular arrangement has been detected. The structural parameters of adsorbed  $\text{CH}_3\text{S}$  radical upon addition of the hydrogen atom are summarized in Fig. 5.48.

The co-adsorption energies ( $\text{CH}_3\text{S}$  and H on surface) are  $-2.88/-2.87/-2.80$  eV on Ni/Pd/Pt surfaces. The adsorption energy of an isolated hydrogen atom (relative to molecular hydrogen in the gas phase) calculated using the same surface cell is  $-0.56/-0.59/-0.48$  eV on the same surface. Combined with the adsorption energies for thiolate, we find that the co-adsorption energies are higher by  $0.45/0.45/0.43$  eV than the sum of the adsorption energies for isolated thiolate radicals and H atoms on these three surfaces.

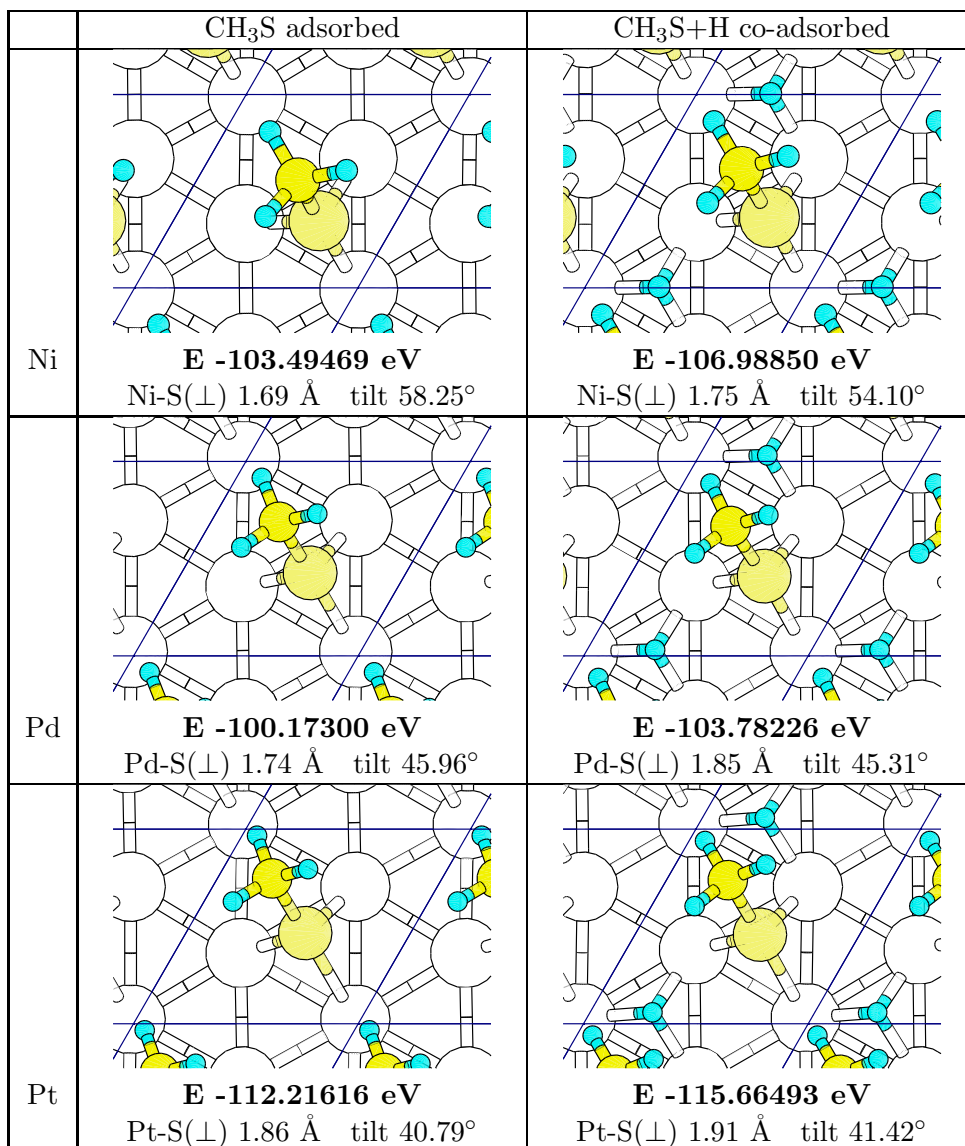


Figure 5.48: Structure of adsorbed CH<sub>3</sub>S before (left-hand side) and after (right) the co-adsorption of hydrogen atom into the unit cell.

In order to suggest an initial guess of the **transition state** using the improved dimer method, VASP requests for an input structure. As one could obtain relaxed structures of CH<sub>3</sub>SH and CH<sub>3</sub>S adsorbed on each metal surface from the previous calculations (static optimizations, Chapters 5.5 and 5.6), the initial guess of the transition state geometries were designed manually from the “input” structures (adsorbed CH<sub>3</sub>SH) by elongating the bond to be broken (i.e., the S-H bond) and slight shifting the resulting surface fragments (CH<sub>3</sub>S and H) towards the surface.

The basic geometry parameters and the look of the adsorption sites for the initial, transition and final states are shown in Fig. 5.49.

For some reasons, not even a metastable transition state for the S–H dissociation on Ni could be found. In the small supercell, the strong lateral interactions forced the H and CH<sub>3</sub>S moieties tear apart in each relaxation run when the S–H bond has been manually weakened. Thus the transition state for Ni, shown in Fig. 5.49 (top-mid image), rather corresponds to a late transition state of the particular reaction step and cannot give us a full information of structure and energetics. One can observe that for this structure, the S–H bondlength is already so long that the fulfilled dissociation may be confirmed, which is also apparent on the total energy of this structure, lying much deeper than that of the initial state.

In general, the initial and final structures found by a subsequent search from the TS are in very good agreement with the most stable configurations found in Chapter 5.5.1 (for CH<sub>3</sub>SH) and in Fig. 5.48 (for CH<sub>3</sub>S+H).

The sketch of the energy profile of the dissociation process for CH<sub>3</sub>SH on Pd(111) is sketched in Fig. 5.50(a). If the energy of the initial structure (physisorbed methane thiol) is set to be the reference (0 eV), then the adsorbed molecule overcomes a barrier of 0.18 eV in order to be rearranged to the transition state structure, which – upon the cleavage of the weakened S-H bond – yields an energy of  $\Delta E = -0.77$  eV forming a surface covered by co-adsorbed CH<sub>3</sub>S and. (Note that the curve is only *fitted* to the initial, intermediate and final energy values.)

A detailed investigation of the geometry parameters is summarized in Table 5.14. It is remarkable that the transition states for the dissociation on Pd and Pt surfaces have a quite different character. On the Pd surface, the S-H bond is strongly stretched, in this “late” transition state the sulfur-hydrogen bond is already broken. On Pt in contrast we find an “early” transition state where the S-H bond undergoes only a modest elongation. The calculated activation energy for the dehydrogenation of CH<sub>3</sub>SH on Pt(111) is in very good agreement with the experiments of Rufael et al. [108], who reported an apparent activation energy of 18 kcal/mole (or 0.78 eV/molecule).

Table 5.14: *Geometry parameters of CH<sub>3</sub>SH dissociation stages on Ni, Pd and Pt.*

M	Property/State	Initial	Transition	Final	CH <sub>3</sub> SH(g)	CH <sub>3</sub> S(g)
Ni	C-S [Å]	1.88	1.84	1.86	1.82	1.79
	S-H [Å]	1.37	2.26	2.62	1.35	—
	M-S (⊥) [Å]	1.95	1.86	1.73	—	—
	C-S-H [°]	92.4	131.7	—	97.0	—
	C-S tilt [°]	55.2	23.5	23.9	—	—
	$\Delta d_{12}/\Delta d_{23}$	-0.4/-0.4	+0.7/-0.3	+0.9/-0.3	—	—
Pd	C-S [Å]	1.84	1.84	1.84	“	“
	S-H [Å]	1.42	1.73	2.84		
	M-S (⊥) [Å]	2.22	2.05	1.88		
	C-S-H [°]	98.8	98.6	—		
	C-S tilt [°]	41.9	43.7	44.7		
	$\Delta d_{12}/\Delta d_{23}$	+0.8/-0.2	+1.5/-0.1	+2.4/+0.1		
Pt	C-S [Å]	1.83	1.89	1.83	“	“
	S-H [Å]	1.36	1.46	2.75		
	M-S (⊥) [Å]	2.37	1.83	1.95		
	C-S-H [°]	95.5	113.2	—		
	C-S tilt [°]	32.7	63.0	37.6		
	$\Delta d_{12}/\Delta d_{23}$	+1.2/-0.7	+1.7/-0.6	+2.9/0.0		

For Pt(111), we used the improved dimer method in order to find the transition state (TS). Upon the TS was found, the reaction path sampling using the intrinsic reaction coordinate (IRC) algorithm [168, 169], as implemented to VASP by Bučko [167], was applied to find the initial structure (“reactant”) and the corresponding final structure (“products”) of the dissociation. In Figure 5.50(b), we show the potential energy profile along IRC, defined as the steepest descent path in mass weighted coordinates that connects the transition state to reactant and product. The intrinsic reaction coordinate has been determined using the damped velocity Verlet algorithm [170].

However, we must also emphasize that as the investigation of the stable adsorption geometries of the absorbed thiol and thiolate have demonstrated that the potential-energy surface is characterized by multiple local minima, the same has to be expected for the saddle point structure. Our simulations have identified one possible, but probably not the only transition state for the dehydrogenation of methane-thiol.

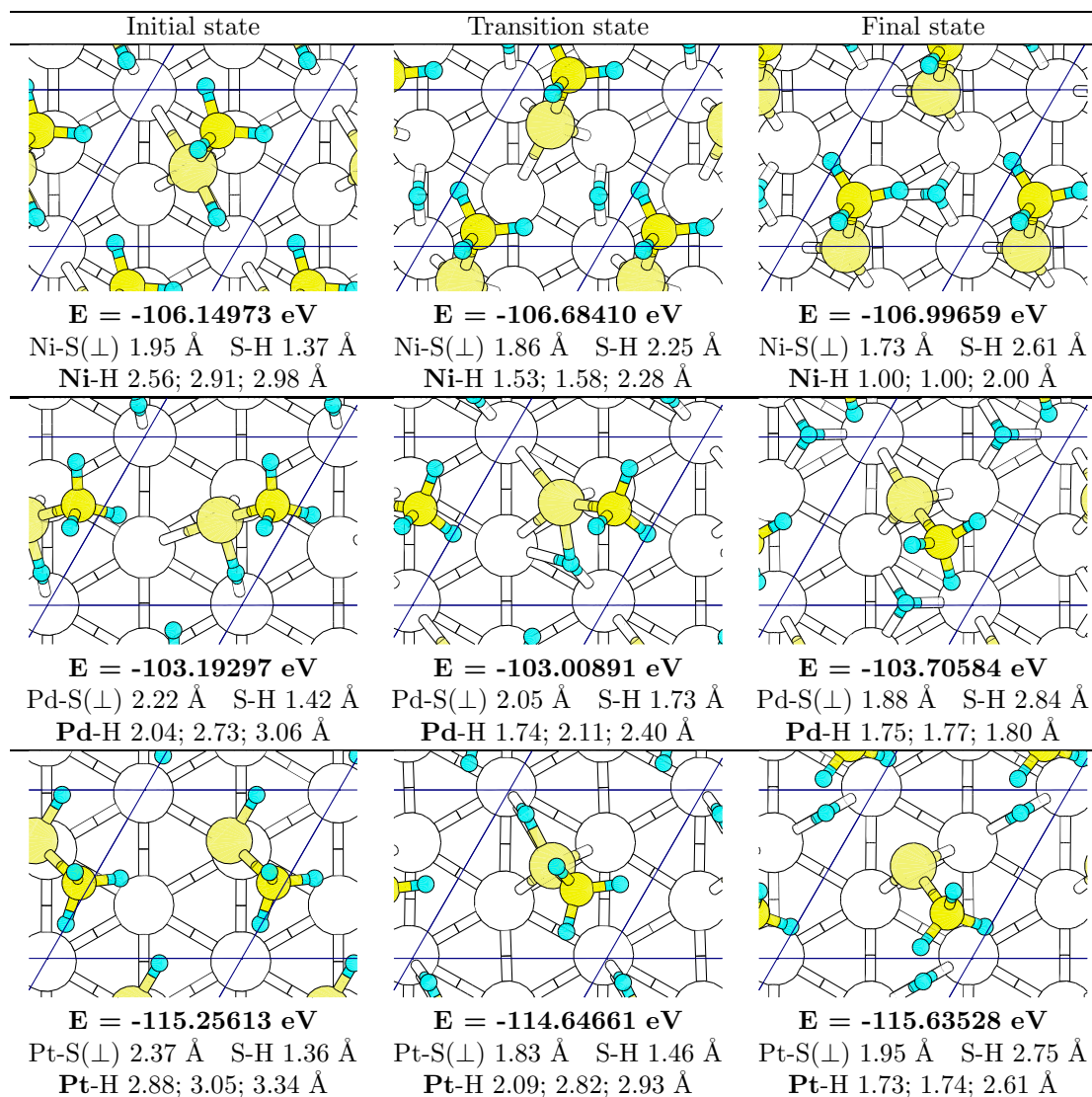
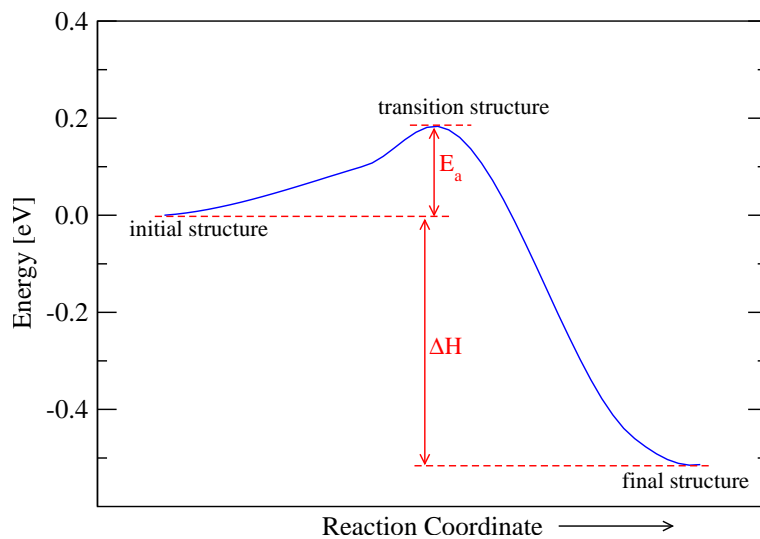
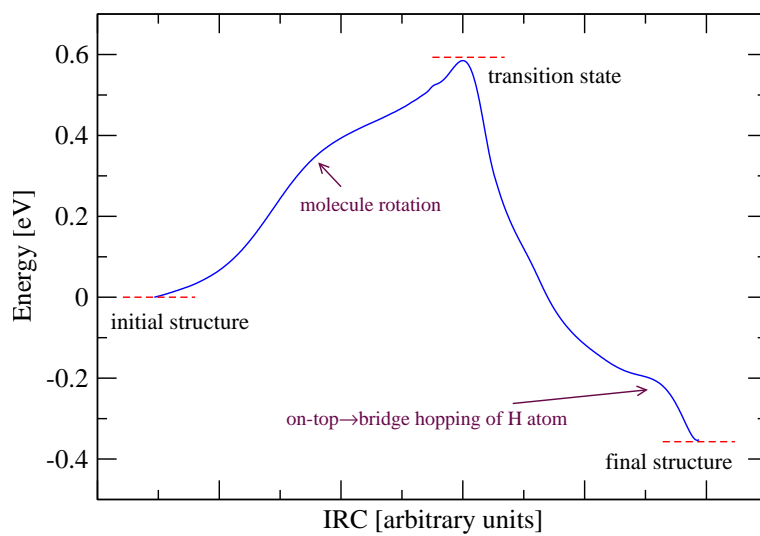


Figure 5.49: Dissociation routes of  $\text{CH}_3\text{S}$  adsorbed on Ni, Pd and Pt.





(a)



(b)

Figure 5.50: Potential energy profile of the dissociation route of  $CH_3SH$  adsorbed on  $Pd(111)$  (a) and on  $Pt(111)$  (b). The path in (b) was calculated along the intrinsic reaction coordinate (IRC).



# Chapter 6

## Conclusions

The thesis focused on a detailed description of adsorption behavior of simple thiols (mercaptoalcohols) on metal surfaces. The thorough investigation by means of DFT theory shows interesting results.

### **Isolated Molecules, Bulk Metals, Clean Metal Surfaces**

The project started using density-functional theory (DFT) by dealing with correct description of bulk metals (Ni, Pd, and Pt) and their clean (111) surfaces. A very detailed calculation on free gas-phase methane thiol molecule and methane thiolate radical showed an excellent agreement in most parameters, that are directly comparable to experiment.

To create a reference to experimental results, calculations of vibrational eigenmodes have been performed using two different approaches: the force-constant (FC) method constructing the dynamical matrix from the forces generated by small displacements of the atoms, and a linear response (LR) approach. The linear response approach also allows to calculate the normal-modes intensities for infrared spectroscopy via the eigenvectors of the normal modes and the Born effective charges. Generally we find very good agreement between the results of these two very different computational methods.

For the gas-phase methane thiol molecule, good agreement with the experimental infrared spectrum is achieved. Existing differences concern mostly the high-frequency C-H stretching modes and are attributable to the neglect of anharmonic corrections. We also find good agreement for the infrared intensities, except for the overestimation of the intensity of the C-S stretching mode.

For the methane thiolate radical, only incomplete experimental information is available from laser-induced fluorescence data and the vibrational fine-structure of photoemission data, leading to reasonable agreement, given the quite substantial differences between the experimental data for high-frequency modes. For the thiolate radical the calculated eigenvectors also allow a unique assignment of the eigenfrequencies.

### Methane Thiol Adsorption

Further, the molecular and dissociative adsorption of methane thiol on the (111) surfaces of the Ni-group metals has been studied in the high-coverage limit. Molecular adsorption is found to be promoted by weak polarization induced forces, leading to adsorption energies increasing from  $-0.37$  eV/molecule on Ni(111) to  $-0.75$  eV/molecule on Pt(111).

In the fully relaxed equilibrium configurations, the S atom is located close to a bridge-site on Ni and Pd, but close to an on-top site on Pt. In all cases, the C-S axis is strongly tilted relative to the surface normal, the tilt angle and the height of the S atom above the surface increasing in the sequence Ni→Pd→Pt. Adsorption leads to a modest elongation of the C-S and S-H bond lengths, promoted by a modest back-donation of electrons from the metal *d*-band to the LUMO orbital of the thiol molecule.

The theoretical investigations of the adsorbed thiol monolayers are interesting, because experimental results are available only for multilayers of unknown coverage. The preparation of monolayers is difficult because even modest heating of the adsorbed films leads to de-hydrogenation and the formation of a thiolate layer. For the thiolate monolayers we calculate strong red-shifts of the S-H and C-S stretching modes (reflecting the activation of the adsorbed molecules for de-hydrogenation), and smaller red-shifts of the C-H rocking and C-H deformation modes. Compared to the available experiments for multilayer CH<sub>3</sub>SH/Ni(111) and CH<sub>3</sub>SH/Pt(111) these changes appear to be overestimated, evidently because the experiments average over the molecules adsorbed on the metals substrates and those physisorbed in subsequent layers.

An important observation is that the differences in the frequencies of the asymmetric C-H stretching and C-H deformation modes are larger than in the gas-phase. This reflects the broken symmetry of the tilted adsorption configuration. However, these differences could not be resolved in the experiment. For CH<sub>3</sub>SH/Pd(111), an outstanding feature is the strong red-shift of the S-H stretching mode because for this system we had found a special adsorption configuration where the H-atom of the thiol group forms a H-bond to a metal atom without dissociating.

## Methane Thiolate Adsorption

On the contrary, concerning the geometry in methane thiolate adsorption, the bonding is promoted by a strong covalent bond between the S- $p$  states and the metal- $d$  band, leading to adsorption energies reaching about  $-2.8$  eV/atom on all three surfaces. The determination of the stable adsorbate geometry is hampered by the existence of multiple local minima on the potential-energy surface as a function of lateral position and height of the S-atom and tilt of the C-S axis.

It has been demonstrated that, as for alkane-thiolates on noble-metal surfaces, a strongly tilted configuration with the S atom in an off-symmetry position between bridge and fcc hollow is preferred. On Ni(111), the stable position is almost exactly in the center of the hollow, while on Pd(111) and Pt(111), it is gradually shifted towards the bridge site. The increasing lateral displacement is correlated to an increasing height above the surface and a tilt angle increasing from  $32^\circ$  to  $49^\circ$ . These results emphasize the similarity with thiolate adsorbed on noble-metals surfaces and contradict earlier studies reporting, due to their insufficient relaxation, an adsorption in the center of an fcc hollow and no tilt in the high-coverage limit.

The preference for a tilted adsorption geometry has been shown to be associated with the electronic structure of the thiolate radical. Bonding is promoted by electron donation from the occupied bonding  $pp_\sigma$  states on the S atom to the substrate and back-donation to the partially occupied non-bonding  $pp_\pi$  states, degeneracy of which is broken in the adsorbed configuration. Experimental information on adsorption geometries is rather scarce. For the best-studied system  $\text{CH}_3\text{S}/\text{Ni}(111)$  we find quantitative agreement between theory and experiment. More experimental information is available from vibrational spectroscopy.

For the thiolate monolayers, the calculations show modest, but significant changes in vibrational properties relative to the adsorbed thiol layers. The differences in the asymmetric C-H deformation and the C-H rocking modes are lower than in the thiol layer and also than in gas-phase thiol molecules. This shows that the adsorbed  $\text{CH}_3\text{S}$  radicals are quite close to  $C_s$  symmetry. The agreement with experiments is reasonable, but it also demonstrates the need of anharmonic correction to the high-frequency C-H stretching modes.

## Reaction Barriers

The investigation also included the dissociation of the adsorbed thiol leading to the formation of co-adsorbed methane thiolate and atomic hydrogen. This process is predicted to be exothermic and non-activated on Ni(111), but activated on Pd(111) and Pt(111).

The reduced exothermic heat of reaction correlates with an increased activation energy for dissociation. The calculated activation energy for Pt(111) is in very good agreement with experiment.

### General Conclusions

In summary, we have demonstrated that DFT calculations provide a very accurate description of the geometry, energetics and the vibrational properties of methane thiol and methane thiolate monolayers on close-packed metal surfaces. A careful structural optimization has demonstrated that both thiol molecules and thiolate radical adsorb in low-symmetry configurations with a tilted C-S axis, even at saturation coverage. The tilted adsorption geometry is also reflected in the vibrational spectra. The theoretical spectra permit a unequivocal interpretation of the experiments. For the gas-phase molecular species we have also compared our DFT results with those based on calculations using hybrid functionals. Application of hybrid functional leads to a blue-shift of all eigenmodes, varying between 30 and 60  $\text{cm}^{-1}$ , and thus worsening agreement with experimental values.

### Future Outlook

Self-assembled monolayers are definitely a promising group of systems, which already came to the breakthrough from general research to application in industry, mainly for the tuning of electrode workfunction. With the fast development of computer simulation methods, even larger molecules sticking on the metal surfaces may be described by the first principles. As it can be seen from each field of study by computer simulations, they rapidly decrease the costs of experimental research by predicting to proceed only those experiments, which have some sense, thus avoiding trial-and-error techniques, saving time and money.

As we understand the bonding between molecule and surface for small adsorbates, we can also easier predict the behavior of long-chain thiols on the surfaces. Comparative studies for more molecules on one surface, or one molecule on different metal surfaces (as in our case) may lead to the statements of structure-properties relationships, that are generalizations of knowledge achieved by simulation or experiment. As enough trends are known, one can interpolate or even extrapolate the adsorption behavior of any thiol-metal system.

# Bibliography

- [1] P. Hohenberg, W. Kohn, Phys. Rev. 136 (1964) 864B.
- [2] W. Kohn, L.J. Sham, Phys. Rev. 140 (1965) A1133.
- [3] J.P. Perdew, A. Zunger, Phys. Rev. B 23 (1981) 5048.
- [4] D.M. Ceperley, B.J. Alder, Phys. Rev. Lett. 45 (1980) 566.
- [5] A.G. Koures, F.E. Harris, Int. J. Quant. Chem. 59 (1996) 3.
- [6] J.P. Perdew. Phys. Rev. Lett. 55 (1985) 1665.
- [7] W. Koch, M.C. Holthausen, *A Chemist's Guide to Density Functional Theory*, Wiley-VCH, Weinheim, 2001.
- [8] G.L. Oliver, J.P. Perdew, Phys. Rev. A 20 (1979) 397.
- [9] U. von Barth, L. Hedin, J. Phys. C: Solid State Phys. 5 (1972) 1629.
- [10] S.H. Vosko, L. Wilk, M. Nusair, Can. J. Phys. 58 (1980) 1200.
- [11] L.A. Cole, J.P. Perdew, Phys. Rev. A 25 (1982) 1265.
- [12] J.P. Perdew, Y. Wang, Phys. Rev. B 45 (1992), 13244.
- [13] D.C. Langreth, J.P. Perdew, Phys. Rev. B 21 (1980) 5469.
- [14] J.P. Perdew, Y. Wang, Phys. Rev. B 33 (1986) 8800.
- [15] J.P. Perdew, J.A. Chevary, S.H. Vosko, K.A. Jackson, M.R. Pederson, D.J. Singh, C. Fiolhais, Phys. Rev. B 46 (1992) 6671.
- [16] J.P. Perdew, K. Burke, M. Ernzerhof, Phys. Rev. Lett. 77 (1996) 3865.
- [17] B. Hammer, L.B. Hansen, J.K. Nørskov, Phys. Rev. B 59 (1999) 7413.

- 
- [18] J. Tao, J.P. Perdew, V.N. Staroverov, E. Scuseria, Phys. Rev. Lett. 91 (2003) 146401.
- [19] J.P. Perdew, M. Ernzerhof, K. Burke, J. Chem. Phys. 105 (1996) 9982.
- [20] J. Heyd, G.E. Scuseria, M. Ernzerhof, J. Chem. Phys. 118 (2003) 8207.
- [21] A.D. Becke, Phys. Rev. A 38 (1988) 3098
- [22] F. Bloch, Z. Physik 52 (1928) 555.
- [23] N.W. Ashcroft, N.D. Mermin, *Solid State Physics*, Harcourt College Publishers, 1976.
- [24] J.C. Phillips, L. Kleinman, Phys. Rev. 116 (1959) 287.
- [25] W. Quester, *Pseudopotential – Wikipedia, the free encyclopedia*. Accessed on-line: 2009-Feb-10. <http://en.wikipedia.org/wiki/Pseudopotential>
- [26] P.E. Blöchl, Phys. Rev. B 50 (1994) 17953.
- [27] R.M. Martin, *Electronic Structure: Basic Theory and Practical Methods*, Cambridge University Press, Cambridge, 2004.
- [28] O. Jepsen, O.K. Andersen, Solid State Commun. 9 (1971) 1763.
- [29] P.E. Blöchl, O. Jepsen, O.K. Andersen, Phys. Rev. B 49 (1994) 16223.
- [30] M. Methfessel, T. Paxton, Phys. Rev. B 40 (1989) 3616.
- [31] H. Hellmann, *Einführung in die Quantenchemie*, Franz Deuticke, Leipzig, 1937.
- [32] R.P. Feynman, Phys. Rev. 56 (1939) 340.
- [33] E. Wimmer, A.J. Freeman, *Fundamentals of the electronic structure of surfaces*, Handbook of Surface Science Vol.2: Electronic structure, Elsevier, Amsterdam, 2000.
- [34] M. Born, K. Huang, *Dynamical Theory of Crystal Lattices*, Oxford University Press, Oxford, 1954.
- [35] M. Gajdoš, K. Hummer, G. Kresse, J. Furthmüller, F. Bechstedt, Phys. Rev. B 73 (2006) 045112.
- [36] S. Baroni, S. de Gironcoli, A. Dal Corso, P. Giannozzi, Rev. Mod. Phys. 73 (2001) 515.



- [37] R. Pick, M.H. Cohen, R.M. Martin, Phys. Rev. B 1 (1970) 910.
- [38] G. Kresse, J. Furthmüller, J. Hafner, Europhys. Lett. 32 (1995) 729.
- [39] P. Brüesch, *Phonons: Theory and Experiments II*, Springer Ser. Solid-State Sci. Vol. 65, Springer, Berlin, 1986.
- [40] S. Baroni, P. Giannozzi, A. Testa, Phys. Rev. Lett. 58 (1987) 1861.
- [41] P. Giannozzi, S. de Gironcoli, P. Pavone, S. Baroni, Phys. Rev. B 43 (1990) 7231.
- [42] P. Giannozzi, S. Baroni, J. Chem. Phys. 100 (1994) 8537.
- [43] A. Shukla, Phys. Rev. B 61 (2000) 13277.
- [44] G. Mills, H. Jónsson, Phys. Rev. Lett. 72 (1994) 1124.
- [45] G. Henkelman, H. Jónsson, J. Chem. Phys. 113 (2000) 9978.
- [46] A. Heyden, A.T. Bell, F.K. Keil, J. Chem. Phys. 123 (2005) 224101.
- [47] G. Henkelman, H. Jónsson, J. Chem. Phys. 111 (1999) 7010.
- [48] S. Senkan, Angew. Chem. Int. Ed. 40 (2001) 312.
- [49] M.-C. Desjonquères, D. Spanjaard, *Concepts in surface physics*, Springer, Berlin, 1996.
- [50] A. Nilsson, L.G.M. Pettersson, J.K.Nørskov, *Chemical Bonding at Surfaces and Interfaces*, Elsevier, Amsterdam, 2008.
- [51] R. Dovesi, B. Civalleri, R. Orlando, C. Roetti, V.R. Saunders, Rev. Comp. Chem. 21 (2005) 1.
- [52] F. Schreiber, Prog. Surf. Sci. 65 (2000) 151.
- [53] A. Ulman, Chem. Rev. 96 (1996) 1533.
- [54] K. Motesharei, D.C. Myles, J. Am. Chem. Soc. 119 (1997) 6674.
- [55] I. Willner, V. Heleg-Shabati, R. Blonder, E. Katz, G. Tao, A.F. Buckman, A. Heller, J. Am. Chem. Soc. 118 (1996) 10321.
- [56] I. Willner, R. Blonder, E.J. Katz, Am. Chem. Soc. 118 (1996) 5310.
- [57] J. Zak, H. Yuan, M. Ho, L.K. Woo, M.D. Porter, Langmuir 9 (1993) 2772.

- [58] F.W. Scheller, F. Schubert, J. Ferrowitz, *Frontiers in Biosensorics*, Vols. I and II, Birkhauser, Berlin, 1996.
- [59] J. Janata, *Principles of Chemical Sensors*, Plenum Press, New York, 1989.
- [60] K. Motesharei, D.C. Myles, *J. Am. Chem. Soc.* 120 (1998) 7328.
- [61] O. Chailapakul, L. Sun, C. Xu, R.M. Crooks, *J. Am. Chem. Soc.* 115 (1993) 12459.
- [62] Y. Yamamoto, H. Nishihara, K. Aramaki, *J. Electrochem. Soc.* 140 (1993) 436.
- [63] L. Häussling, B. Michel, H. Ringsdorf, H. Rohrer, *Angew. Chem. Int. Ed. Eng.* 30 (1991) 569.
- [64] J.C. Love, L.A. Estroff, J.K. Kriebel, R.G. Nuzzo, G.M. Whitesides, *Chem. Rev.* 105 (2005) 1103.
- [65] W.C. Bigelow, D.L. Pickett, W.A. Zisman, *J. Colloid Interface Sci.* 1 (1946) 513.
- [66] J. Sagiv, *J. Am. Chem. Soc.* 102 (1980) 92.
- [67] D.L. Allara, R.G. Nuzzo, *Langmuir* 1 (1985) 45.
- [68] R.G. Nuzzo, D.L. Allara, *J. Am. Chem. Soc.* 105 (1983) 4481.
- [69] P.E. Laibinis, G.M. Whitesides, D.L. Allara, Y.T. Tao, A.N. Parikh, R.G. Nuzzo, *J. Am. Chem. Soc.* 113 (1991) 7152.
- [70] M.M. Walczak, C. Chung, S.M. Stole, C.A. Widrig, M.D. Porter, *J. Am. Chem. Soc.* 113, (1991) 2370.
- [71] P. Fenter, P. Eisenberger, J. Li, N. Camillone, S. Bernasek, G. Scoles, T.A. Ramanarayanan, K.S. Liang, *Langmuir* 7 (1991) 2013.
- [72] S. Hwang, Y.H. Jang, H. Kim, *Bull. Korean Chem. Soc.* 12 (1991) 635.
- [73] M. Yu, S.M. Driver, D.P. Woodruff, *Langmuir* 21 (2005) 7285.
- [74] G.S. Parkinson, A. Hentz, P.D. Quinn, A.J. Window, D.P. Woodruff, P. Bailey, T.C.Q. Noakes, *Surf. Sci.* 601 (2007) 50.
- [75] H. Rieley, G.K. Kendall, A. Chan, R.G. Jones, J. Lüdecke, D.P. Woodruff, B.C.C. Cowie, *Surf. Sci.* 392 (1997) 143.

- [76] M. Stratmann. *Adv. Mater.* 2 (1990) 191.
- [77] M. Stratmann. *Stahl u. Eisen* 113 (1993) 101.
- [78] J. Lara, T. Blunt, P. Kotvis, A. Riga, W.T. Tysoe, *J Phys. Chem. B* 102 (1998) 1703.
- [79] W. Shen, G.L. Nyberg, *Surf. Sci.* 296 (1993) 49.
- [80] C.W. Sheen, J.-X. Shi, J. Mårtensson, A.N. Parikh, D.L. Allara. *J. Am. Chem. Soc.* 114 (1992) 1514.
- [81] Y. Gu, Z. Lin, R.A. Butera, V.S. Smentkowski, D.H. Waldeck, *Langmuir* 11 (1995) 1849.
- [82] O.M. Magnussen, B.M. Ocko, M. Deutsch, M.J. Regan, P.S. Pershan, L.E. Berman, D. Abernathy, J.F. Legrand, G. Grübel. *Nature* 384 (1996) 250.
- [83] N. Muskal, I. Turyan, D. Mandler, *J. Electroanal. Chem.* 409 (1996) 131.
- [84] M.G. Samant, C.A. Brown, J.G. Gordon II, *Langmuir* 8 (1992) 1615.
- [85] M.H. Dishner, J.C. Hemminger, F.J. Feher. *Langmuir* 13 (1997) 4788.
- [86] F.K. Huang, R.C. Horton, D.C. Myles, R.L. Garrell. *Langmuir* 14 (1998) 4802.
- [87] J.G. Van Alsten, *Langmuir* 15 (1999) 7605.
- [88] C.D. Bain, G.M. Whitesides, *J. Am. Chem. Soc.* 111 (1989) 7164.
- [89] R.C. Thomas, L. Sun, R.M. Crooks, A.J. Ricco, *Langmuir* 7 (1991) 620.
- [90] M. Buck, M. Grunze, F. Eisert, J. Fischer, F. Trager, *J. Vac. Sci. Technol. A* 10 (1992) 926.
- [91] G. Hahner, C. Woll, M. Buck, M. Grunze, *Langmuir* 9 (1993) 1955.
- [92] D.S. Karpovich, G.J. Blanchard, *Langmuir* 10 (1994) 3315.
- [93] C. Vericat, M.E. Vela, R.C. Salvarezza, *Phys. Chem. Chem. Phys.* 7 (2005) 3258.
- [94] H. Kondoh, M. Iwasaki, T. Shimada, K. Amemiya, T. Yokohama, T. Ohta, M. Shimomura, S. Kono, *Phys. Rev. Lett.* 90 (2003) 66102.

- [95] M.G. Roper, M.P. Skegg, C.J. Fisher, J.J. Lee, V.R. Dhanak, D.P. Woodruff, R.G. Jones, *Chem. Phys. Lett.* 389 (2004) 87.
- [96] G.E. Poirier, E.D. Pylant, *Science* 272 (1996) 1145.
- [97] M.E. Castro, J.M. White, *Surf. Sci.* 257 (1991) 22.
- [98] H. Yang, T.C. Caves, J.L. Whitten, D.R. Huntley, *J. Am. Chem. Soc.* 116 (1994) 8200.
- [99] C.J. Fisher, D.P. Woodruff, R.G. Jones, B.C.C. Cowie, V. Formoso, *Surf. Sci.* 496 (2002) 73.
- [100] T.S. Rufael, D.R. Huntley, D.R. Mullins, J.L. Gland, *J. Phys. Chem.* 99 (1995) 11472.
- [101] D.R. Mullins, D.R. Huntley, T. Tang, D.K. Saldin, W.T. Tysoe, *Surf. Sci.* 380 (1997) 468.
- [102] T.S. Rufael, D.R. Huntley, D.R. Mullins, J.L. Gland, *J. Phys. Chem. B* 102 (1998) 3431.
- [103] J.C. Love, D.B. Wolfe, R. Haasch, M.L. Chabinyk, K.E. Paul, G.M. Whitesides, R.G. Nuzzo, *J. Am. Chem. Soc.* 125 (2003) 2597.
- [104] A. Carvalho, M. Geissler, H. Schmid, B. Michel, E. Delamarche, *Langmuir*, 2002, 18 (6), p. 2406.
- [105] J.C. Love, D.B. Wolfe, M.L. Chabinyk, K.E. Paul, G.M. Whitesides, *J. Am. Chem. Soc.* 124 (2002) 1576.
- [106] R.J. Koestner, J. Stöhr, J.L. Gland, E.B. Kollin, F. Sette, *Chem. Phys. Lett.* 120 (1985) 285.
- [107] T.S. Rufael, R.J. Koestner, E.B. Kollin, M. Salmeron, J.L. Gland, *Surf. Sci.* 297 (1993) 272.
- [108] T.S. Rufael, J. Prasad, 1, D.A. Fischer, J.L. Gland, *Surf. Sci.* 278 (1992) 41.
- [109] H. Sellers, *Surf. Sci.* 264 (1992) 177.
- [110] S.S. Kim, Y. Kim, H.I. Kim, S.H. Lee, T.R. Lee, S.S. Perry, J.W. Rabalais, *J. Chem. Phys.* 109 (1998) 9574.
- [111] J.J. Lee, C.J. Fisher, C. Bittencourt, D.P. Woodruff, A.S.Y. Chan, R.G. Jones, *Surf. Sci.* 516 (2002) 1.

- [112] T.H. Lin, T.P. Huang, Y.L. Liu, C.C. Yeh, Y.H. Lai, W.H. Hung, *Surface Science* 578 (2005) 27.
- [113] Z. Li, S.C. Chang, R.S. Williams, *Langmuir* 19 (2003) 6744.
- [114] G. Kresse, J. Furthmüller, *Phys. Rev. B* 54 (1996) 11169.
- [115] G. Kresse, J. Furthmüller, *Comput. Mater. Sci.* 6 (1996) 15.
- [116] G. Kresse, J. Hafner, *Phys. Rev. B* 47 (1993) 558.
- [117] G. Kresse, J. Hafner, *J. Phys.* 6 (1994) 8245.
- [118] G.M. Shipman, T.S. Woodall, R.L. Graham, A.B. Maccabe, P.G. Bridges, *Proc. of Parallel and Distributed Processing Symposium, 2006. IPDPS 2006* (2006) 10.
- [119] G. Kresse, D. Joubert, *Phys. Rev. B* 59 (1999) 1758.
- [120] H.J. Monkhorst, J.D. Pack, *Phys. Rev. B* 13 (1976) 5188.
- [121] M. Methfessel, A.T. Paxton, *Phys. Rev. B* 40 (1989) 3616.
- [122] F.D. Murnaghan, *Am. J. Math.* 59 (1937) 235.
- [123] G.W.C. Kaye, T.H. Laby, *Tables of physical and chemical constants*, 15<sup>th</sup> edition, Longman, London, 1993.
- [124] C. Kittel, *Introduction to Solid State Physics*, 7<sup>th</sup> edition, Wiley, New York, 1996.
- [125] W.R. Tyson, W.A. Miller, *Surf. Sci.* 62 (1977) 267.
- [126] N.E. Singh-Miller, N. Marzari, *Phys. Rev. B* 80 (2009) 235407.
- [127] J.E. Demuth, P.M. Marcus, D.W. Jepsen, *Phys. Rev. B* 11 (1975) 1460.
- [128] Y. Kuk, L.C. Feldman, P.J. Silverman, *Phys. Rev. Lett.* 50 (1983) 511.
- [129] H. Ohtani, M.A. Van Hove, G.A. Somorjai, *Surf. Sci.* 187 (1987) 372.
- [130] R. Feder, H. Pleyer, P. Bauer, N. Müller, *Surf. Sci.* 109 (1981) 419.
- [131] D.L. Adams, H.B. Nielsen, M.A. Van Hove, *Phys. Rev. B* 20 (1979) 4789.
- [132] F. Mittendorfer, A. Eichler, J. Hafner, *Surf. Sci.* 423 (1999) 1.

- [133] K. Barbalace, *Periodic Table of Elements*. Accessed on-line: 2007-Dec-11. <http://EnvironmentalChemistry.com/yogi/periodic/Ni.html>
- [134] G.D. Kubiak, *J. Vac. Sci. Technol. A* 5 (1987) 731.
- [135] G.N. Derry, Z. Ji-Zhong, *Phys. Rev. B* 39 (1989) 1940.
- [136] NIST Chemistry Webbook, <http://webbook.nist.gov/chemistry/>.
- [137] Gaussian 03, Revision C.02, M.J. Frisch, G.W. Trucks, H.B. Schlegel, G.E. Scuseria, M.A. Robb, J.R. Cheeseman, J.A. Montgomery Jr., T. Vreven, K.N. Kudin, J.C. Burant, J.M. Millam, S.S. Iyengar, J. Tomasi, V. Barone, B. Mennucci, M. Cossi, G. Scalmani, N. Rega, G.A. Petersson, H. Nakatsuji, M. Hada, M. Ehara, K. Toyota, R. Fukuda, J. Hasegawa, M. Ishida, T. Nakajima, Y. Honda, O. Kitao, H. Nakai, M. Klene, X. Li, J.E. Knox, H.P. Hratchian, J.B. Cross, V. Bakken, C. Adamo, J. Jaramillo, R. Gomperts, R.E. Stratmann, O. Yazyev, A.J. Austin, R. Cammi, C. Pomelli, J.W. Ochterski, P.Y. Ayala, K. Morokuma, G.A. Voth, P. Salvador, J.J. Dannenberg, V.G. Zakrzewski, S. Dapprich, A.D. Daniels, M.C. Strain, O. Farkas, D.K. Malick, A.D. Rabuck, K. Raghavachari, J.B. Foresman, J. V. Ortiz, Q. Cui, A. G. Baboul, S. Clifford, J. Cioslowski, B. B. Stefanov, G. Liu, A. Liashenko, P. Piskorz, I. Komaromi, R.L. Martin, D.J. Fox, T. Keith, M.A. Al-Laham, C.Y. Peng, A. Nanayakkara, M. Challacombe, P.M.W. Gill, B. Johnson, W. Chen, M.W. Wong, C. Gonzalez, J.A. Pople, Gaussian, Inc., Wallingford CT, 2004.
- [138] L.A. Curtiss, R.H. Nobes, J.A. Pople, L. Radom., *J. Chem. Phys.* 97 (1992) 6766.
- [139] R.D. El Bouzaidi, A. El Hammadi, A. Boutalibb, M. El Mouhtadi, *J. Molec. Struct. (THEOCHEM)* 497 (2000) 197.
- [140] D.R. Lide, *CRC Handbook of Chemistry and Physics*, 81<sup>st</sup> edition, CRC Press, Boca Raton, 2001.
- [141] P.J. Stephens, F.J. Devlin, C.F. Chabalowski, M.J. Frisch, *J. Phys. Chem.* 98 (1994) 11623.
- [142] A.D. Becke, *J. Chem. Phys.* 98 (1993) 5648.
- [143] A. Rauk, S. Collins, *J. Molec. Spectr.* 105 (1984) 438.
- [144] I.W. May, E.L. Pace, *Spectrochim. Acta A* 24 (1968) 1605.
- [145] S. Chiang, Y. Lee, *J. Chem. Phys.* 95 (1991) 66.

- [146] A. Kokalj, *J. Mol. Graphics Modelling* 17 (1999) 176. Code available from <http://www.xcrysden.org/>.
- [147] M. Suzuki, G. Inoue, H. Akimoto, *J. Chem. Phys.* 81 (1984) 5405.
- [148] P. Misra, X. Zhu, H.L. Bryant, *Pure and Appl. Opt.* 4 (1995) 587.
- [149] C.-P. Liu, Y. Matsuda, Y.-P. Lee, *J. Chem. Phys.* 119 (2003) 12335.
- [150] C.-P. Liu, S.A. Reid, Y.-P. Lee, *J. Chem. Phys.* 122 (2005) 124313.
- [151] R.L. Schwartz, G.E. Davico, W.C. Lineberger, *J. Electr. Spectr. and Relat. Phenom.* 108 (2000) 163.
- [152] B.K. Janousek, J.I. Brauman, *J. Chem. Phys.* 72 (1980) 694.
- [153] A.V. Marenich, J.E. Boggs, *J. Chem. Theory Comput.* 1 (2005) 1162.
- [154] D.R. Alfonso, *Surf. Sci.* 602, (2008) 2758.
- [155] J. M. Nicovich, K. D. Kreutter, C. A. Van Dijk, P. H. Wine, *J. Phys. Chem.* 96 (1992) 2518.
- [156] S.H. Wilson, M.N.R. Ashfold, R.N. Dixon, *J. Chem. Phys.* 101 (1994) 7538.
- [157] A. Balakrishnan, V. Smith, B.P. Stoicheff, *Phys. Rev. Lett.* 68 (1992) 2149.
- [158] J. Jiao, S.-Y. Bu, G.-C. Wang, X.-H. Bu, *J. Molec. Struct.: THEOCHEM* 862 (2008) 80.
- [159] L.M. Ghiringhelli, R. Caputo, L. delle Site, *J. Phys.: Condens. Matter* 19 (2007) 176004.
- [160] C. Majumder, *Langmuir* 24 (2008) 10838.
- [161] Y. Yourdshahyan, A.M. Rappe, *J. Chem. Phys.* 117 (2002) 825.
- [162] P. Maksymovych, D.C. Sorescu, J.T. Yates, *J. Phys. Chem. B* 110 (2006) 21161.
- [163] A. Fernandez, J.P. Espinosa, A.R. Gonzalez-Elipse, M. Kerkar, P.B.J. Thompson, J. Ludeck, G. Scragg, A.V. de Cavalho, D.P. Woodruff, M. Fernandez-Garcia, J.C. Conesa, *J. Phys.: Condens. Matter* 7 (1995) 7781.
- [164] J. Gottschalck and B. Hammer, *J. Chem. Phys.* **116**, 784 (2002).

- 
- [165] J. Liu, E.J. Salumbides, U. Hollenstein, J.C.J. Koelemeij, K.S.E. Eikema, W. Ubachs, F. Merkt, *J. Chem. Phys.* 130 (2009) 174306.
- [166] K. Piszczatowski, G. Łach, M. Przybytek, J. Komasa, K. Pachucki, B. Jeziorski, *J. Chem. Theory Comput.* 5 (2009) 3039.
- [167] T. Bučko, *J. Phys.: Condens. Matter* 20 (2008) 064211.
- [168] K. Fukui, *Phys. Chem.* 74 (1970) 4161.
- [169] K. Fukui, *Acc. Chem. Res.* 14 (1981) 363.
- [170] H.P. Hratchian, H.B. Schlegel, *J. Phys. Chem. A* 106 (2002) 165.



# List of Publications

- 1 D. Karhánek, P. Kačer, M. Kuzma, J. Šplíchalová, L. Červený,  
*The platinum-olefin binding energy in series of  $(PH_3)_2Pt(olefin)$  complexes – a theoretical study,*  
J. Mol. Model. 13 (2007) 1009.
- 2 P. Kačer, M. Kuzma, D. Karhánek, J. Švrček, L. Červený,  
*Application of molecular modelling in heterogeneous catalysis research,*  
Chem. Centr. J. 2 (Suppl. I) (2008) P37.
- 3 J. Švrček, D. Karhánek, P. Kačer, E. Leitmannová, J. Šplíchalová, L. Červený,  
*Particle size effect and its influence on the adsorbed complex stability,*  
Appl. Catal. A: General 354 (2009) 169.
- 4 J. Švrček, P. Kačer, M. Kuzma, D. Karhánek, J. Šplíchalová, E. Leitmannová, L. Červený,  
*Simulation of platinum surface complexes using NMR spectroscopy,*  
Catal. Commun., submitted (2009).
- 7 D. Karhánek, T. Bučko, J. Hafner,  
*A density-functional study of the adsorption of methane-thiol on the (111) surfaces of the Ni-group metals: I. Molecular and dissociative adsorption,*  
J. Phys.: Condens. Matter, submitted (2010).
- 7 D. Karhánek, T. Bučko, J. Hafner,  
*A density-functional study of the adsorption of methane-thiol on the (111) surfaces of the Ni-group metals: II. Vibrational analysis,*  
J. Phys.: Condens. Matter, submitted (2010).



# Conference Presentations and Seminars, Poster Sessions

## Oral Presentations:

- 1 D. Karhánek, P. Kačer, M. Kuzma, L. Červený, *Surface Complexes in Catalysis*, XXXVII Symposium on Catalysis, November 07<sup>th</sup>-08<sup>th</sup>, 2005, Prague, Czech Republic.
- 2 D. Karhánek, J. Hafner, *Self-Assembled Monolayers on Transition Metal Surfaces*, New Developments in Surface Science - Seminar, Technical University of Vienna, April 18<sup>th</sup>, 2007, Vienna, Austria.
- 3 D. Karhánek, J. Hafner, *Thiol SAMs studied by DFT*, Seminar lecture, Institute of Chemical Research of Catalonia (ICIQ), May 8<sup>th</sup>, 2009, Tarragona, Spain.

## Posters:

- 1 D. Karhánek, P. Kačer, M. Kuzma, L. Červený, *The Platinum-Olefin Binding Energy in  $(PH_3)_2Pt(Olefin)$  Complexes: A Theoretical Study*, XXXVI Symposium on Catalysis, October 08<sup>th</sup>-09<sup>th</sup>, 2004, Prague, Czech Republic.
- 2 D. Karhánek, J. Hafner, *Self-Assembled Monolayers Studied by DFT*, The CMS Science College Evaluation Hearing, Austrian Science Fund (FWF), November 28<sup>th</sup>, 2007, Vienna, Austria.



# Abstract

The present thesis is devoted to the quantum-mechanical description of adsorption process and thermodynamics in self-assembled monolayers of simple thiols on transition metal surfaces. As an *ab-initio* computational tool, the VASP software package was used, and the calculations were performed on the computer clusters belonging to Computational Materials Science (CMS) framework at the University of Vienna.

The adsorption of thiols (such as methane thiol, CH<sub>3</sub>SH) on metal surfaces, mostly gold, has been studied since early 1980's. On most metals, formation of thiolates (like methane thiolate, CH<sub>3</sub>S) occurs already at moderate temperatures. In this thesis, the adsorption of methane thiol on the (111) crystallographic planes of nickel, palladium and platinum was studied in detail.

As a model of the surface, a 3D-supercell with  $(\sqrt{3}\times\sqrt{3})R30^\circ$  periodicity of the adsorbate has been chosen, as experimentally this is the most dense and stable packing of the molecules on the surface, giving a surface coverage  $\Theta = 1/3$ .

The aim of this project was to investigate periodic trends in the strength of CH<sub>3</sub>SH adsorption and dissociation on the surfaces of the Ni-group metals. It was found out that methane thiol adsorbs weakly on the surfaces and the adsorption energy increases in the order Ni<Pd<Pt (−0.37/ − 0.60/ − 0.75 eV). Its dissociation product, methane thiolate CH<sub>3</sub>S, forms strongly bound monolayers and the released adsorption energy is almost the same for all 3 metals ( $\approx -2.7$  eV).

In addition, vibrational properties (eigenvalues, eigenvectors and intensities of the infrared normal modes) of the adsorbed species have been thoroughly studied and subsequently compared with experimental data. The electronic states (projected density of states spectra) and difference charge-densities have been studied as well, leading to elucidation of the nature of adsorbate-substrate bonding.

A simulation of the hydrogen dissociation from adsorbed CH<sub>3</sub>SH (using the very recently implemented *improved dimer method*) showed that the corresponding reaction barrier increases in the order Ni<Pd<Pt (0.00/ +0.18/ +0.60 eV), whereas the enthalpy of this reaction step follows a reverse order (−0.85/ − 0.52/ − 0.42 eV).



# Zusammenfassung

Die vorliegende Dissertation widmet sich der quantenmechanischen Beschreibung der Adsorption selbstorganisierter monomolekularer Schichten (*engl.* self-assembled monolayers, SAMs) von einfachen Thiolen auf Übergangsmetalloberflächen. Für *ab-initio* Rechnungen auf den Computer-Clustern des Computational Materials Science (CMS) der Universität Wien wurde das Software-Paket VASP verwendet.

Spontane Adsorption von Thiolen (wie z.B. Methanthiol, CH<sub>3</sub>SH) auf Metalloberflächen, vorwiegend Gold, wurde seit Anfang 1980 untersucht. Auf den meisten Metallen kommt es dann zu einer Bildung von Thiolaten (wie z.B. Methanthiolat, CH<sub>3</sub>S) schon bei niedrigen Temperaturen. In der vorliegenden Arbeit wurde die Adsorption von Methanthiol auf (111) kristallographischen Ebenen von Nickel, Palladium und Platin betrachtet.

Als Modell der Oberflächenstruktur wurde eine 3D-Superzelle mit einer  $(\sqrt{3} \times \sqrt{3})R30^\circ$  Periodizität des Adsorbats gewählt, da diese als die dichteste und stabilste Packung der Moleküle auf der Oberfläche bildet. Dies entspricht einer Oberflächenbedeckung von  $\Theta = 1/3$ .

Ziel des Projektes war es, Trends in der Adsorptionsstärke von CH<sub>3</sub>SH und CH<sub>3</sub>S auf Oberflächen der Metalle der Ni-Gruppe zu untersuchen. Es wurde festgestellt, dass Methanthiol auf den Oberflächen schwach adsorbiert, wobei die Adsorptionsenergie in der Reihenfolge Ni < Pd < Pt zunimmt ( $-0.37 / -0.60 / -0.75$  eV). Das Dissoziations-Produkt, Methanthiolat CH<sub>3</sub>S, bildet stark gebundene monomolekulare Schichten und die dabei freigegebene Adsorptionsenergie ist für alle 3 Metalle etwa gleich hoch ( $\approx -2.7$  eV).

Zusätzlich wurde eine detaillierte Schwingungsanalyse (Eigenwerte, Eigenvektoren und Intensitäten der infrarotaktiven Normalschwingungen) der adsorbierten Species durchgeführt und nachfolgend mit experimentellen Daten verglichen. Die elektronischen Zustände (projizierte Zustandsdichte-Spektren) und Ladungsdichte-Differenzen wurden ebenfalls dargestellt, um eine Charakterisierung der Adsorbat-Substrat Bindungen zu ermöglichen.

Simulation der Wasserstoffatom-Dissoziation von adsorbiertem CH<sub>3</sub>SH (mit Hilfe der verbesserten Dimer-Methode) zeigte, dass die entsprechende Reaktionsbarriere in der Reihenfolge Ni < Pd < Pt ( $0 / +0.18 / +0.60$  eV) zunimmt, während die Enthalpie dieses Reaktionsschrittes die umgekehrte Reihenfolge besitzt ( $-0.85 / -0.52 / -0.42$  eV).





# Curriculum Vitae

## Personal information:

Name: David Karhánek  
Born: August 3<sup>rd</sup> 1982 in Prostějov (former Czechoslovakia)  
Citizenship: Czech Republic  
Parents: Anna Karháňková, Zdeněk Karhánek  
Contact: david.karhanek@gmail.com

## Education:

1988 - 1994 Elementary school in Prostějov, Czech Republic  
1994 - 2000 Secondary school (natural sciences), Prostějov, Czech Rep.  
May 2000 Graduation with honour  
2000 - 2005 Master studies of chemistry:  
Dept. of Organic Technology, Institute of Chemical Technology, Prague, Czech Republic;  
Master thesis (supervisor Prof. Ing. Libor Červený, DrSc.):  
*The Study of Surface Complexes in Heterogeneous Catalysis*  
June 2005 Graduation with honour, awarding the academic degree *Ing.*  
(equivalent to *Dipl.-Ing. / MSc.*)  
2005 - 2010 Doctoral studies of natural sciences:  
Computational Materials Physics, Univ. of Vienna, Austria;  
Thesis (supervisor o.Univ.Prof. Dipl.-Ing. Dr. Jürgen Hafner):  
*Self-Assembled Molecular Monolayers Studied by Density-Functional Theory*  
May 2010 Attempting the academic degree *Dr. rer. nat.*